



**EXPERIMENTAL DEMONSTRATION OF AN ALGORITHM TO
DETECT THE PRESENCE OF A PARASITIC SATELLITE**

THESIS

Vincent J. Dabrowski, Captain, USAF

AFIT/GAE/ENY/03-2

DEPARTMENT OF THE AIR FORCE
AIR UNIVERSITY

AIR FORCE INSTITUTE OF TECHNOLOGY

Wright-Patterson Air Force Base, Ohio

APPROVED FOR PUBLIC RELEASE; DISTRIBUTION UNLIMITED

The views expressed in this thesis are those of the author and do not reflect the official policy or position of the United States Air Force, Department of Defense, or the United States Government.

AFIT/GAE/ENY/03-2

EXPERIMENTAL DEMONSTRATION OF AN ALGORITHM TO
DETECT THE PRESENCE OF A PARASITIC SATELLITE

THESIS

Presented to the Faculty
Department of Aeronautics and Astronautics
Graduate School of Engineering and Management
Air Force Institute of Technology
Air University
Air Education and Training Command
in Partial Fulfillment of the Requirements for the
Degree of Master of Science in Aeronautical Engineering

Vincent J. Dabrowski, B.S.

Captain, USAF

March, 2003

APPROVED FOR PUBLIC RELEASE; DISTRIBUTION UNLIMITED

AFIT/GAE/ENY/03-2

EXPERIMENTAL DEMONSTRATION OF AN ALGORITHM TO
DETECT THE PRESENCE OF A PARASITIC SATELLITE

Vincent J. Dabrowski, B.S.

Captain, USAF

Approved:

Maj Richard G. Cobb, Ph.D.
Thesis Advisor

Date

Bradley S. Liebst, Ph.D.
Committee Member

Date

Steven G. Tragesser, Ph.D.
Committee Member

Date

Acknowledgements

First and foremost I thank Maj. Rich Cobb who treated me less like a student and more like a research associate. Maj. Cobb gave me the freedom to find my own way and enough expert advice to keep me on track.

I acknowledge the members of my committee Dr. Brad Liebst and Dr. Steve Tragesser for their helpful insight. Their input produced a more understandable and readable product.

I also thank Mr. Wilbur Lacy, Mr. Jay Anderson, and Mr. Barry Page for their help in the lab. They were always ready and willing to assist with their knowledge and support.

Most of all, I thank my beautiful wife. Even though we were separated by thousands of miles, her love, support, and encouragement pushed me to the finish.

Vincent J. Dabrowski

Table of Contents

	Page
Acknowledgements	iv
List of Figures	viii
List of Tables	xi
List of Symbols	xii
List of Abbreviations	xiv
Abstract	xvi
I. Introduction	1-1
1.1 Current Microsat/Nanosat Rendezvous and Docking Capability	1-2
1.2 A Threat Exemplified	1-4
1.3 Impact of a Satellite Attack	1-5
1.4 Current Noncooperative Docking Detection Technology	1-6
1.4.1 Ground-Based Detection	1-7
1.4.2 Satellite Monitoring	1-7
1.5 Need for Improved Detection/“Smart” Systems	1-8
1.6 Research Objectives	1-9
1.7 Thesis Outline	1-10
II. Background	2-1
2.1 Literature Review	2-1
2.1.1 System Identification	2-1
2.1.2 System Identification Methods	2-2
2.2 The Satellite Model	2-3
2.2.1 Rotational Dynamics	2-4
2.2.2 Rotational Kinematics	2-9
2.2.3 Satellite Controller	2-12
2.2.4 Reaction Wheel System	2-13
2.3 Docking Event Detection	2-14
2.4 Dynamic Detection	2-19
2.5 Summary	2-21

	Page
III. Characterization of Experimental Equipment	3-1
3.1 Air Bearing Assembly	3-2
3.2 Satellite Assembly	3-3
3.2.1 Structure	3-3
3.2.2 Attitude Determination	3-4
3.2.3 Attitude Control	3-5
3.2.4 Command and Data Handling	3-6
3.2.5 Power	3-7
3.2.6 Other Systems	3-7
3.3 Ground-Station Computer	3-8
3.3.1 Hardware	3-8
3.3.2 Software	3-8
3.4 Model Matching	3-9
3.4.1 Moment of Inertia	3-9
3.4.2 Reaction Wheels	3-10
3.4.3 System Delay	3-11
3.4.4 Detection Maneuver	3-12
3.5 Summary	3-12
IV. Results and Analysis	4-1
4.1 Test Procedure	4-1
4.2 Test Scope	4-3
4.3 Test Results	4-4
4.3.1 Baseline Results	4-5
4.3.2 Estimated MOI Results	4-7
4.3.3 Estimated MOI Results, Method Two	4-9
4.3.4 Estimated MOI Results, Method Three	4-11
4.3.5 Repeatability	4-12
4.4 Application of Results	4-13
4.4.1 Method	4-13
4.4.2 Applied Results	4-14
4.5 System-Level Characteristics	4-15
4.6 Summary	4-16
V. Conclusions and Recommendations	5-1
5.1 Conclusions	5-1
5.2 Recommendations	5-2
5.2.1 Future Work	5-2
5.2.2 Current Results	5-3

	Page
Appendix A. LN-200 Fiber Optic Gyroscope Upgrade	A-1
Appendix B. Reaction Wheel Motor Tuning	B-1
Appendix C. Minimization Program Code	C-1
Appendix D. Simulation Model Library	D-1
Appendix E. Experimental Model Library	E-1
Appendix F. Experiment Software User Interface	F-1
Bibliography	BIB-1
Vita	VITA-1

List of Figures

Figure	Page
1.1. Size Comparison SNAP-1 [31], GPS-IIR [19], and HST [19]	1-2
2.1. Satellite Functional Diagram	2-4
2.2. Satellite Body Axes	2-5
2.3. Kinematic Single-Axis Rotations	2-9
2.4. Satellite Proportional Plus Derivative Controller	2-13
2.5. Proportional Plus Integral Plus Derivative with Velocity Feed-Forward and Acceleration Feed-Forward Motor Controller	2-14
2.6. Satellite Targeted Based on Center of Mass Location	2-16
2.7. Comparison of a Low-Fidelity Docking Versus a Debris Collision of Equal Magnitude	2-17
2.8. Comparison of a Moderate-Fidelity Docking Versus a Debris Collision of Equal Magnitude	2-18
2.9. Comparison of a High-Fidelity Docking Versus a Debris Collision of Equal Magnitude	2-18
3.1. Satellite Assembly and Air Bearing	3-2
3.2. Space Electronics, Inc. Model SE9791 Tri-axis Spherical Air Bearing	3-3
3.3. Humphrey CF-75-0201-1 Axis Rate Gyroscope and Mounting	3-4
3.4. Reaction Wheel Cluster	3-5
3.5. Experimental Simulink Satellite Model	3-8
3.6. Simulation Simulink Satellite Model	3-9
3.7. SIMSAT Body Axes	3-9
3.8. Typical SIMSAT MOI Truth Test	3-10
3.9. Reaction Wheel Look-Up Table Profile	3-11
3.10. One Degree Detection Maneuver	3-12
4.1. Example Data Set	4-2
4.2. Example Data Fit	4-5
4.3. Baseline Data Histogram	4-6

Figure		Page
4.4.	Estimated MOI Histogram, 0.5° Maneuver	4-7
4.5.	Estimated MOI Histogram, 1° Maneuver	4-7
4.6.	Estimated MOI Histogram, 2° Maneuver	4-8
4.7.	Detection Result Statistics	4-8
4.8.	Data Overlap and Accuracy	4-9
4.9.	Detection Result Statistics, Method Two	4-10
4.10.	Data Overlap and Accuracy, Method Two	4-10
4.11.	Detection Result Statistics, Method Three	4-11
4.12.	Data Overlap and Accuracy, Method Three	4-12
4.13.	Repeatability Comparison, 2° Maneuver	4-13
4.14.	Hubble Space Telescope	4-15
4.15.	Second Order Characteristics as a Function of MOI	4-16
A.1.	LN-200 Fiber Optic Gyroscope	A-2
B.1.	Default Tuning Response	B-2
B.2.	Intermediate Tuning Response	B-3
B.3.	Final Tuning Response	B-4
D.1.	Top Level Simulation Model	D-1
D.2.	Proportional Plus Derivative Controller, Level 2 Submodel . .	D-2
D.3.	Dynamics Model, Level 2 Submodel	D-2
D.4.	Wheel Dynamics, Level 3 Submodel	D-2
D.5.	Rigid Body Dynamics, Level 3 Submodel	D-3
D.6.	Euler 3-2-1 Kinematics, Level 2 Submodel	D-4
E.1.	Top Level Experimental Model	E-1
E.2.	Proportional Plus Derivative Controller, Level 2 Submodel . .	E-2
E.3.	Motor Communications, Level 2 Submodel	E-3
E.4.	Velocity Decoder Cluster, Level 3 Submodel	E-4
E.5.	Single Velocity and Position Decoder, Level 4 Submodel . . .	E-5
E.6.	Position Decoder, Level 5 Submodel	E-6
E.7.	Motor Initialization, Level 3 Submodel	E-7

Figure	Page
E.8. Velocity Encoder Cluster, Level 3 Submodel	E-8
E.9. Single Velocity Encoder, Level 4 Submodel	E-9
E.10. Analog Telemetry Decoder, Level 2 Submodel	E-10
E.11. Gyroscope Decoder and Calibration, Level 3 Submodel	E-11
E.12. Euler 3-2-1 Kinematics, Level 2 Submodel	E-12
F.1. Gyroscope Calibration Interface	F-1
F.2. General Operation Interface	F-2

List of Tables

Table	Page
1.1. Image Resolution Requirements for Satellite Mission & Payload Assessment [32]	1-7
3.1. Humphrey Model CF-75-0201-1 Axis Rate Gyroscope Characteristics	3-4
3.2. Animatics SmartMotor™ Model SM3450 Motor System Characteristics	3-5
3.3. Animatics SmartMotor™ Model SM3450 Motor System Integrated Controller Settings	3-6
3.4. Normalized Error Results for Various System Level Delays	3-11
4.1. MOI Values Tested	4-4
4.2. Number of Test Points at Different Detection Maneuver Magnitudes	4-4
4.3. Statistical Analysis of Different Baseline Detection Maneuver Magnitudes	4-6
4.4. Estimation Method Comparison, Method Two	4-10
4.5. Estimation Method Comparison, Method Three	4-11
4.6. Results of Repeatability Investigation	4-13
A.1. Northrop Grumman® LN-200 Characteristics	A-2

List of Symbols

Symbol	Page
$\mathbf{b}_i \cdots$ Body Coordinates	2-4
$\mathbf{M} \cdots$ Moment Exerted on the Satellite	2-5
$\mathbf{H} \cdots$ Satellite Angular Momentum	2-5
$\{\cdot\}_I \cdots$ Inertial Frame of Reference	2-5
$\mathbf{A} \cdots$ Generic Vector	2-5
$\{\cdot\}_B \cdots$ Body Frame of Reference	2-5
$\boldsymbol{\Omega}^{B/I} \cdots$ Angular Velocity Vector Between the Body and Inertial Reference Frames	2-5
$\boldsymbol{\Omega} \cdots$ Satellite Angular Velocity Vector with Respect to the Inertial Frame of Reference	2-5
$\rho \cdots$ Vector Distance from an Element of Satellite Mass to the Satellite Center of Mass	2-5
$dm \cdots$ Infinitesimal Element of Mass	2-5
$\mathbf{I} \cdots$ Satellite Inertia Matrix	2-7
$I_{rw} \cdots$ Reaction Wheel Moment of Inertia	2-8
$\omega_i \cdots$ Reaction Wheel Angular Velocity	2-8
$\psi \cdots$ Satellite Yaw Angle	2-9
$\theta \cdots$ Satellite Pitch Angle	2-9
$\phi \cdots$ Satellite Roll Angle	2-9
$K_P \cdots$ Proportional Gain Constant	2-13
$K_D \cdots$ Derivative Gain Constant	2-13
$s \cdots$ Laplace Variable	2-13
$T_D \cdots$ Derivative Time Constant	2-13
$e \cdots$ Control Error	2-13
$\mathbf{H}_{s/c} \cdots$ Spacecraft Angular Momentum	2-15
$\mathbf{H}_{debris} \cdots$ Debris Angular Momentum	2-15
$\mathbf{r} \cdots$ Position Vector From the Spacecraft Center of Mass to the Point of Debris Impact	2-15
$\mathbf{p} \cdots$ Debris Linear Momentum	2-15

Symbol	Page
$m_{particle}$... Debris Mass	2-15
t_{step} ... Simulation Timestep	2-16
$m_{parasite}$... Parasite Mass	2-16
I_{new} ... Combined Satellite and Microsatellite Moment of Inertia . . .	2-16
J ... Cost Function	2-20
\mathbf{y}_{actual} ... Time History of the Actual Satellite Response	2-20
\mathbf{y}_{model} ... Time History of the Model Response	2-20
\mathbf{y}_{test} ... Time History of the Satellite Response to be Tested	2-20
E_i ... Normalized Angular Mismatch	4-11
$\Delta \mathbf{I}$... Change in Satellite Moment of Inertia Due to Presence of Parasite	4-13
Δm ... Change in Satellite Mass Due to Presence of Parasite	4-14

List of Abbreviations

Abbreviation	Page
US ... United States	1-1
SOI ... Space Object Identification	1-1
LEO ... Low Earth Orbit	1-1
GEO ... Geosynchronous Orbit	1-1
DoD ... Department of Defense	1-1
SSA ... Space Situational Awareness	1-1
GPS ... Global Positioning System	1-2
HST ... Hubble Space Telescope	1-2
COTS ... Commercial Off-The-Shelf	1-2
SSTL ... Surrey Space Technologies, Ltd.	1-2
AFRL ... Air Force Research Lab	1-3
LLNL ... Lawrence Livermore National Lab	1-3
XSS-10 ... AFRL/LLNL Microsat Servicer Test Article	1-3
DARPA ... Defense Advanced Research Projects Agency	1-3
μ N ... Micronewtons	1-4
W ... Watts	1-4
ASAT ... Anti-Satellite	1-4
ID ... Identification	1-7
RAIDRS ... Rapid Attack Identification, Detection and Reporting System	1-8
MOI ... Moment of Inertia	1-9
AFIT ... Air Force Institute of Technology	1-9
SIMSAT ... AFIT Satellite Simulator	1-9
ACTEX ... Advanced Controls Technology Experiment	2-2
ETS-VI ... Engineering Test Satellite-VI	2-2
PEM ... Prediction Error Method	2-2
4SID ... State Space Subspace System Identification	2-2
ERA ... Eigensystem Realization Algorithm	2-2
FFT ... Fast Fourier Transform	2-3

Abbreviation	Page
PSD ... Power Spectral Density	2-3
PD ... Proportional Plus Derivative	2-12
PID ... Proportional Plus Integral Plus Derivative	2-13
+MOI ... Additional Moment of Inertia	4-3
SD ... Standard Deviation	4-6
FOG ... Fiber Optic Gyroscope	A-1
DC ... Direct Current	A-2
SDLC ... Synchronous Data Link Control	A-2

Abstract

Published reports of microsatellite weapons testing have led to a concern that some of these “parasitic” satellites could be deployed against US satellites to rendezvous, dock and then disrupt, degrade, disable, or destroy the system. Since the United States is the most space-dependent country on earth, it has the most to lose from this type of attack. Current detection techniques including the use of ground-based detection by optical trackers, radar sensors and satellite telemetry monitoring were found to be inadequate. Therefore, an effective detection method is required.

Both impact sensing and dynamic sensing solutions were investigated. Dynamic detection, the most effective solution, was further explored to include the creation of a detection algorithm. The algorithm consists of a dynamic detection maneuver and satellite model which is tuned in order to match the model response to the physical system response. The detection maneuver is performed regularly and matched to the model by minimizing a least-squares type cost function over the model’s moment of inertia.

The algorithm was constructed and validated on AFIT’s ground-based satellite simulator, SIMSAT. Results indicate that microsatellites rigidly connected to a satellite can be detected with a series of small identical maneuvers utilizing data available from a typical attitude determination and control system. Variations on the technique were investigated using the same SIMSAT data. All algorithm variations readily detected parasite-induced moment of inertia changes of 3–23%. The most accurate detection scheme estimated the moment of inertia to 0.67%. These results were applied to operational systems to gain insight into the performance that may be achievable on-orbit. The results look promising for potential microsatellite threats to US systems. The detection scheme presented could easily be integrated into a complete space situational awareness system.

EXPERIMENTAL DEMONSTRATION OF AN ALGORITHM TO DETECT THE PRESENCE OF A PARASITIC SATELLITE

I. Introduction

Advances in the miniaturization of space systems technology have, and will continue to, lead to reductions in space vehicle size and cost. These reductions are leading to a world-wide explosion in microsatellite usage. One particularly promising area of research is the use of microsatellites (microsats) as inspection and servicing vehicles for larger satellites. However, this same technology can be used to rendezvous and dock with a satellite and disrupt, degrade, disable, or destroy it. Since the United States (US) is the most space-dependent country on earth, it has the most to lose from these types of attacks [43].

Ground-based detection of such threats are insufficient. A 1999, government-sponsored report by the Schafer Corporation [32] concluded that the US Space Object Identification (SOI) capability in Low Earth Orbit (LEO) is inadequate. Worden [44] explains: “These sensors are mostly 1960s and 1970s era radar and optical tracking sensors” and the US “cannot detect and track microsatellite-sized objects in Geosynchronous Orbit (GEO).” The US Fiscal Year 2000-01 Department of Defense (DoD) Space Technology Guide [26] cites the need for on-orbit diagnostics aboard all satellites. It states that “assets must be capable of surveying their own space environment, both for self-protection against natural and man-made threats and to determine if they are under attack.” This concept is referred to as Space Situational Awareness (SSA).

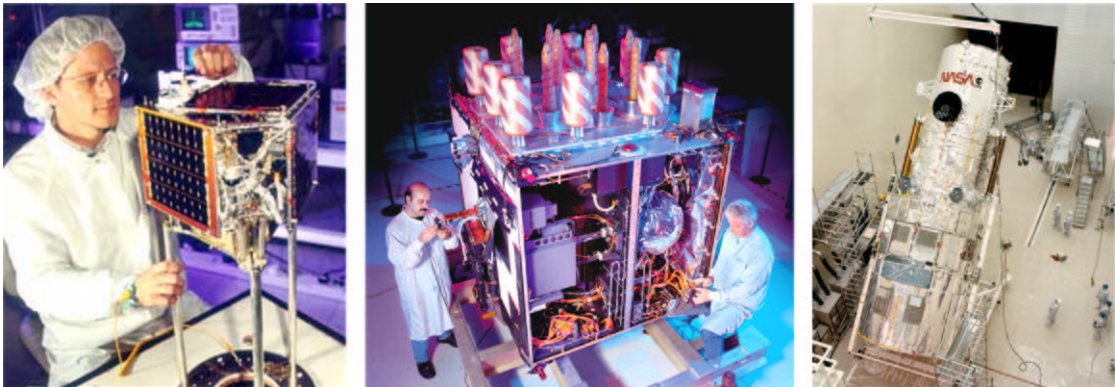


Figure 1.1 Size Comparison SNAP-1 [31], GPS-IIR [19], and HST [19]

1.1 Current Microsat/Nanosat Rendezvous and Docking Capability

Microsats and Nanosats are defined as satellites with masses less than 100 kg and 10 kg respectively. Miniaturization enables increasingly complex mission to be performed by these increasingly smaller/lighter vehicles. Figure 1.1 compares the size of the 6.5 kg SNAP-1 nanosat to the size of an 1100 kg Global Positioning System (GPS) satellite and 11,000 kg Hubble Space Telescope (HST) satellite.

Microsat projects are characterized by rapid development scales of six to thirty-six months. Cutting-edge or Commercial Off-The-Shelf (COTS) technology is routinely employed in order to provide innovative solutions and cheaper alternatives to the established methods and systems [31]. Cheaper space operations through the use of microsats have attracted many countries. Wilson [43] elaborates on the worldwide proliferation of microsats:

Surrey Space Technologies, Ltd. (SSTL), in England, is considered to be the market leader in microsatellite technology. SSTL is a commercial, majority owned subsidiary of the University of Surrey. SSTL has conducted technology transfer and training programs with a goal of enabling emerging space nations to master microsatellite technology as a step in facilitating the development and deployment of an increasingly capable national space infrastructure. To date SSTL has conducted technology transfer and training programs with: China (Tsinghua-1), South Korea (KITSat-1/2), Portugal (PoSat-1), Pakistan (BADR-1), Chile (FASat-Alfa/Bravo), South Africa (UoSAT-3/4/5), Thailand (TMSAT-1), Sin-

gapore (Merlion payload), and Malaysia (TiungSAT-1). Recently, SSTL conducted a satellite inspection mission with the Russians and Chinese using the 6.5 kg SNAP-1 nanosat. In addition to SSTL, other countries involved in maturing microsat technology include: Russia, Israel, Canada, Sweden, and Australia.

Microsat rendezvous and docking is an active research topic. The payoff for large satellites is enormous. Satellite servicing (refueling, repairing, or upgrading) promises to extend the life of large, high-priced existing and future satellites. This potential is driving research at an accelerated rate. In 1996, Rafazzotti [27] presented a “simulator to support the analysis and development of safe techniques to approach, circumflight, and inspect non-cooperative spacecraft.” Today, many detailed designs for such microsats exist. An Air Force Research Lab (AFRL)/Lawrence Livermore National Lab (LLNL) design [17] and ground testing results [16] are readily available. This 28 kg AFRL/LLNL microsat servicer test article (XSS-10) was flown in January 2003.

The Defense Advanced Research Projects Agency (DARPA) is in the design stage of its Autonomous Space Transporter and Robotic Orbiter (ASTRO) demonstration program. DARPA created ASTRO as part of a larger Orbital Express suite which is planned to create a comprehensive on-orbit servicing architecture. ASTRO is an autonomous microsat servicer for in-situ refueling and modular upgrades to other spacecraft [42]. It requires only minimal input from ground controllers to do its job.

Moser *et al.* [21] describes the commissioning of four studies (sponsored by AFRL) to explore the feasibility and affordability of producing 100 microsats for under \$100M. Each satellite was to have a wet mass of under 40 kg, be capable of on-orbit inspection and servicing of a generic customer satellite, and be capable of 600 m/s delta-V. Lifetime requirements were 1-month of operational use, 1-year of dormant mode, and 1- to 5-years of shelf life. The vehicles were either to be launched into a 400 by 1000 km storage orbit at 55 degrees inclination awaiting transfer orders,

launched on demand using a small launch vehicle, or air-deployed. The microsat was to gather images of the target on its way to rendezvous before docking autonomously. All four studies produced a convincing design with a technology freeze date of 2003. The studies cited propulsion as an area where improvement could yield substantial gains in capability.

Innovative solutions are being developed in the area of micropropulsion research. One example is the work being done by Gulczinski *et al.* [13] in developing the Micro-Pulsed Plasma Thruster. It is designed to “provide all stationkeeping and attitude control” for 25-kg class or smaller satellites. The unoptimized test unit weighs only 600 grams and provides thrust from 20–80 μN using 2–10 W of power.

With the vast amount of research in this area, it was only a matter of time before new uses for this technology were explored. Governments are often the first to exploit new technologies for revolutionary military applications.

1.2 A Threat Exemplified

The Report of the Commission to Assess US National Security Space Management and Organization [9]—commonly known as the 2001 Rumsfeld Space Commission Report states:

Microsatellites can perform satellite inspection, imaging and other functions and could be adapted as weapons. Placed on an interception course and programmed to home on a satellite, a microsatellite could fly alongside a target until commanded to disrupt, disable or destroy the target. Detection of and defense against such an attack could prove difficult.

Microsat weapons development programs exist. On 5 January 2001, Tung Yi of the Hong Kong Sing Tao Jih Pao newspaper [46] quoted Chinese sources who indicated that the Small Satellite Institute under the Research Institute of Space Technology of the Chinese Academy of Sciences has secretly completed ground tests of an anti-satellite (ASAT) weapon named “parasitic satellite.” Less than a month

later, the Hong Kong Ming Pao newspaper [6] reported a similar story. The articles describe the system as consisting of a carrier satellite, a parasite satellite, a launcher, and ground station. The weapon is secretly deployed as a covert secondary payload of the carrier satellite. At some later time, it is released, and homes in on the target satellite, eventually docking with it. During times of war, the ground station sends a command to either jam or destroy the host satellite.

The papers claim the “parasitic satellites” are small and light to avoid interfering with the normal operation of the host satellite “and thus [avoid] being detected by the enemy [46].” Tung Yi also reports the cost of such a weapon is between one one-hundredth and one one-thousandth that of an ordinary satellite, making it very cost-effective.

The newspapers explain the weapon will soon be deployed on an experimental basis and will enter space testing in the near future. This weapon will provide China with “asymmetrical combat capability so that it will become capable of completely paralyzing [an] enemy’s fighting system when necessary by ‘attacking selected vital point[s]’ in [an] enemy’s key areas [46].”

1.3 Impact of a Satellite Attack

The US relies on satellite systems to provide imagery, communications, timing, weather, and navigational data. This reliance caused the Rumsfeld Space Commission Report to conclude “the US is an attractive candidate for a ‘Space Pearl Harbor’ [9].”

Loss of US space systems in a time of crisis could have a crippling effect on the Nation’s ability to respond. “It could lead to forbearance when action is needed or to hasty action when more or better information would have given rise to a broader and more effective set of response options [9].” Wilson [43] outlines the potential impact as follows:

Some examples of the potential impact of deception, disruption, denial, degradation, or destruction of specific space systems by foreign offensive counterspace operations include:

- Impairment or elimination of reconnaissance satellites that would reduce situational awareness and could lead to military surprise, underestimation of enemy strength and capabilities, less effective planning, and less accurate targeting and battle damage assessments.
- Impairment or elimination of missile launch detection satellites that would degrade the US's ability to perform missile launch warning, missile defense, and would increase the psychological impact of the adversary's ballistic missiles.
- Impairment or elimination of satellite communications systems that would disrupt troop command and control problems at all force levels.
- Impairment or elimination of navigation satellites that would make troop movements more difficult, aircraft and ship piloting problematic, and could render many precision-guided weapon systems ineffective or useless.
- Impairment or elimination of Earth resource and weather satellites that would make it more difficult to plan effective military operations.

Threatening or attacking the space capabilities of the US would have domestic, economic and political consequences and could provoke international disputes about the origin and intent of an attack.

There are a number of possible crises or conflicts in which the potential vulnerability of national security space systems would be especially worrisome. During these situations, the President, his senior advisors and military commanders would be dependent on information from US satellite systems to help manage the crisis, conduct military operations or bring about a resolution to the conflict. If the performance of US systems were reduced, the diplomatic and military leverage of the US could decrease, the position of an adversary could be improved, and the cost and risks associated with achieving US objectives would increase.

1.4 Current Noncooperative Docking Detection Technology

There are two current methods of detection: ground-based detection and satellite monitoring. Ground-based sensing relies on the use of radar sites and telescopes to find and track harmful objects. Satellite monitoring is the process of watching

satellite telemetry (orientation, acceleration data, subsystem status, etc.) for signs of an attack. Both techniques fall short of a robust capability.

1.4.1 Ground-Based Detection. The US currently tracks over 10,000 known orbiting space objects using radar and optical trackers—most of these sensors are 1960s and 1970s vintage. The US has only limited capabilities to search for unknown objects using these sensors. Microsat-sized objects in higher orbits such as GEO are totally undetectable/untrackable [44].

There is a limited capability to do SOI in LEO. For small satellites (<1 m in diameter), identification (ID) is limited due to inadequate size and shape information. Inadequate resolution restricts the ability to do a detailed characterization or resolve anomalies of these satellites (Table 1.1). Satellite status determination is limited by radar coverage with no capability for theater coverage [32]. If these systems are to be used for SSA or SOI, they must be upgraded [44].

Table 1.1 Image Resolution Requirements for Satellite Mission & Payload Assessment [32]

Satellite Size	Diameter (m)	Resolution Requirement (cm)	US Capability
Large	>15	>50	current
Medium	15–5	16	current
Small	5–2.5	8	limit
Mini	2.5–0.6	2	beyond

1.4.2 Satellite Monitoring. A docking event can range from a violent collision to feather-light soft dock. Desrocher *et al.* [10] comment on the complexity of docking detection by an operational team:

Satellite platform and payload performance monitoring and course of action decision-making are complex, multi-variate problems for operators. Many times, when anomalies arise, even the most skilled of operators typically have neither the tools, the scientific and engineering

backgrounds, nor the means for efficient, real-time collection of all relevant information to make the proper assessment and take appropriate action.

1.5 Need for Improved Detection/“Smart” Systems

In 1998, former Commander-in-Chief, US Space Command, General Howell M. Estes III [30] admitted: “If we have an attack [on a satellite], I have no [way of knowing], for sure, that it’s been attacked. We have ways of telling something happened to the satellite, but why did it quit?”

Anomaly detection and accurate diagnosis is the first step toward SSA. Unfortunately, an attack can easily be confused with natural phenomena [9]. For example, space debris can reasonably explain the result of a docking-type impact. “In order for the US to react appropriately to an attack on its space systems, it must first know that it has been attacked and the nature of the attack [43].” This is the reason why the DoD [26] has concluded: “Assets must be capable of surveying their own space environment, both for self-protection against... man-made threats and to determine if they are under attack.” It suggests the use of on-orbit diagnostics. A “smart” system would be able to constantly access its own environment and report significant findings to operators on the ground.

The DoD’s Rapid Attack ID, Detection and Reporting System (RAIDRS) [36] is a step in that direction. Desrocher *et al.* [10] are developing the expert systems for the RAIDRS program. They are “applying artificial intelligence and automated data collection to support near real-time anomaly detection, characterization, and reporting.”

Having identified the problem, this thesis now turns to possible solutions to the parasite satellite problem. These solutions can take many forms including upgrades to existing ground-based sensors, additional sensors (cameras, pressure sensors, etc.)

installed on new satellites, new inspection satellites to check older satellites, and dynamic detection techniques, one of which is described herein.

1.6 Research Objectives

In this thesis, a simple satellite model is employed to detect the presence of a “parasitic satellite” docked to the satellite of interest. Detection of both the docking event itself and post-dock presence are examined. It is anticipated that by matching the model response to the on-orbit satellite response, changes in a satellite’s Moment of Inertia (MOI) due to the additional mass of the parasite, can be identified. The merits and limitations of this method of detection are investigated and presented.

The investigation began by creating a mathematical model (using Simulink[®] included with MATLAB[®]) of the satellite and matching it to the response of an actual satellite. This requires characterization of the attitude control system and modal analysis. Modal analysis (looking at all the frequency dynamics of the satellite structure) can be used to identify mass and stiffness changes to flexible elements of the satellite. For the research considered herein, a rigid body analysis will be used. Changes in the rigid body response can be directly correlated to MOI changes, and thus ID the parasite. A rigid satellite is chosen to match available experimental equipment. A detection maneuver was designed and a database of satellite responses to this maneuver was cataloged. A nominal model is defined to best fit the data. Docking events are then simulated and compared to space debris collisions of similar intensity. The detection maneuver is performed post-dock and the response is fit to the nominal model allowing the change in MOIs to be estimated.

To demonstrate and validate the detection technique, a variety of cases are tested on the Air Force Institute of Technology’s (AFIT) ground-based satellite simulator (SIMSAT). The simulator system consists of an air bearing assembly allowing nearly frictionless motion in three restricted rotational degrees-of-freedom, an untethered small satellite assembly consisting of a 3-axis gyroscope, three reaction

wheels, an onboard command and control computer, batteries, and wireless, real-time communications from a ground-station computer. The detectability of the “parasitic satellite” attached to the satellite simulator will be examined and presented. Once demonstrated and validated, this detection method could be integrated into a larger “smart” system for anomaly detection/resolution.

1.7 Thesis Outline

This chapter motivated the problem of on-orbit parasitic microsatellite detection and introduced the research effort. Chapter II reviews literature relevant to this research as well as develops the tools necessary for application in subsequent chapters. Specifically, previous work in on-orbit system ID and MOI estimation are presented, followed by the derivation of the dynamic equations of motion for a satellite controlled by reaction wheels, struck by space debris, and subject to docking. Simulations were performed to gain insight into the phenomena and a dynamic detection algorithm was constructed. Chapter III characterizes the hardware used to validate the algorithm. The test procedure and scope are outlined in Chapter IV. The test results are then presented followed by the data analysis. Several estimation schemes were tested and are presented. The best estimation scheme was applied to models of operational systems to assess the level of performance this type of algorithm may provide. Chapter V provides a summary of the work performed, the results achieved, recommendations for future study, and conclusions.

II. Background

2.1 Literature Review

The dynamic detection of satellite property changes is simply an estimation process. There are numerous estimation methods, many of which are thoroughly documented. One type of estimation methodology is known as system ID.

2.1.1 System Identification. System ID is the process of creating mathematical models of dynamic systems based on observed input/output data. It is a well documented area of research extending far beyond its applications to space systems. Research can range from Vidal *et al.* [37] characterizing an optical pick-up in a common compact disk player to Huang *et al.* [15] estimating the orientation and position of a suspended cylinder at National Aeronautics and Space Administration Langley Research Center's magnetic suspension testbed.

For space vehicles, system ID is generally performed as a precursor to controller design. Often new methods are tested theoretically, like in [18], before their widespread use experimentally and in practice.

On-orbit system ID is an important step towards a high-performance satellite controller. Haugse *et al.* [14] examined the dynamic characteristics of an operational space vehicle in an effort to explore the math model limitations and restricted data provided by ground tests. It was found that “a well designed ground test can predict on-orbit frequencies within the $\pm 10\%$ design frequency sensitivity” for the application used in their research. This result emphasizes the need for on-orbit characterization of satellite parameters especially when their accurate knowledge is critical to the implementation of a detection algorithm.

A smaller number of papers, however, have been written with regard to on-orbit system ID. Adachi *et al.*, in 1999 [1], was frustrated that

...very few papers have appeared that report on-orbit experimental results obtained using actual spacecraft. Exceptions are the vibration test of Hermes [11], the Solar Array Flight Experiment [29], the Middeck Active Control Experiment by the Space Shuttle [12], and the Hubble Space Telescope pointing-control study [5].

Other examples include Manning and Casteel's [20] on-orbit work on the Advanced Controls Technology Experiment (ACTEX), Stetson's on-orbit ID work on NOAA-2 [33], and Wertz and Lee's operational MOI estimation of the Cassini spacecraft.

2.1.2 System Identification Methods. Various on-orbit system ID methods have been investigated. Most, like [3], focus on system ID for the sole purpose of spacecraft attitude control (including flexible shape control). Some of these methods and findings are presented below.

Adachi *et al.* [1] compared two different ID methods on Engineering Test Satellite-VI (ETS-VI). The Prediction Error Method (PEM) is based on the polynomial black-box model while the State-Space Subspace System ID (4SID) is based on state-space models. Frequency and time domains were used for comparison. Both PEM and 4SID were found to create an accurate mathematical model of the satellite, but the 4SID method was shown to be more promising for large space structures like ETS-VI.

Whorton and Calise [40] used data from the closed-loop response to random noise input and a simultaneous, iterative, system ID, and controller design process to get a high fidelity open-loop plant model. By tackling the controller design and system ID together, the authors obtained a model which minimizes the difference between the modeled and actual responses. This method was subsequently validated with ground test data.

Yamaguchi *et al.* [45] also used closed-loop data, but from an impulse response on ETS-VI. The Eigensystem Realization Algorithm (ERA) was used to extract

a closed-loop plant model and algebraic manipulation used to reach an open-loop model with good results.

Haugse *et al.* [14] used on-board excitation to compare the Fast Fourier Transform (FFT), Power Spectral Density (PSD), and ERA methods. It was found that the FFT method was preferable in detecting modes, while the PSD method may be preferable in the determination of damping. ERA was found to do a good job of finding both after a suitable data set was identified by one of the other methods.

Since most system ID experiments are aimed at producing an improved satellite controller design, the properties of mass and MOIs are usually treated as known quantities and parameters such as damping ratio and resonant frequencies are to be found. If the attachment of a “parasitic satellite” is to be found, the reverse is more useful.

Wertz and Lee [39] estimate the inertia tensor of the Cassini spacecraft based on conservation of angular momentum. Telemetry data of the reaction wheel spin rates, spacecraft angular velocities, and ground-based mass properties measurements of the reaction wheel flywheels were used to calculate the moments and products of inertia with good agreement with the values estimated from ground-based tests.

Clemen [7] mentions the estimation of a satellite MOI as a sidebar to estimating other satellite parameters, mainly thruster performance. Various estimators were examined including linear, non-linear, Extended Kalman, and a search scheme based on minimizing the difference between measured and modeled data, the results of which were characterized as “exemplary.” A similar estimation scheme has been employed in this thesis.

2.2 The Satellite Model

The heart of the proposed detection algorithm is the satellite model. Without it, anomalies might be detected, but they can not be resolved. The following satellite model can be used as a building block for more complex systems.

Some parts of the satellite model are loosely based on the original design of SIMSAT [8]. For this thesis, the model has been extensively modified to accommodate new hardware, software, and research intent. It is comprised of a position command input that feeds into the controller subsystem. The controller calculates the wheel commands based on the target orientation and the current orientation. This causes a change in reaction wheel velocities resulting in satellite motion. The motion is sensed in the body frame of reference and changed into an inertial frame, by kinematic equations, completing the loop. Figure 2.1 is a functional representation of the model.

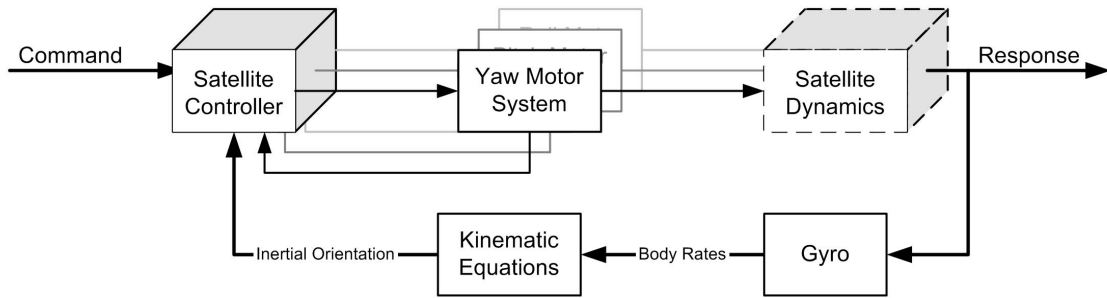


Figure 2.1 Satellite Functional Diagram

2.2.1 Rotational Dynamics. The way in which applied torques/moments affect the satellite's motion is known as the rotation dynamics of the system. Only rigid body motion is considered here since the validation hardware was built as a rigid structure. All reasonable attempts were made to create a mathematical model which accurately matched the physical system.

Figure 2.2 defines the body axes, \mathbf{b}_i 's, where i is the axis number. Orbital motion is assumed to be in the \mathbf{b}_1 direction.

Starting from Newton's Second Law and following Wie [41], Stevens and Lewis [34], and Nelson [24],

$$\mathbf{M} = \left\{ \frac{d\mathbf{H}}{dt} \right\}_I \quad (2.1)$$

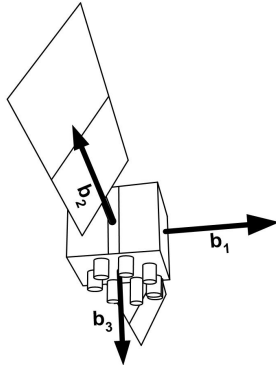


Figure 2.2 Satellite Body Axes

where \mathbf{M} is the moment exerted on the satellite, \mathbf{H} is the angular momentum of the satellite itself and $\{\cdot\}_I$ notates that the derivative is taken with respect to an inertial frame of reference. Use the identity:

$$\left\{ \frac{d\mathbf{A}}{dt} \right\}_I = \left\{ \frac{d\mathbf{A}}{dt} \right\}_B + \boldsymbol{\Omega}^{B/I} \times \mathbf{A} \quad (2.2)$$

where \mathbf{A} is a generic vector, $\{\cdot\}_B$ denotes the body frame of reference, and $\boldsymbol{\Omega}^{B/I}$ is the angular velocity vector between the reference frames. Equation 2.1 then becomes:

$$\mathbf{M} = \left\{ \frac{d\mathbf{H}}{dt} \right\}_B + \boldsymbol{\Omega} \times \mathbf{H} \quad (2.3)$$

where $\boldsymbol{\Omega}$ is the satellite angular velocity vector with respect to the inertial frame of reference.

The satellite's angular momentum is defined as

$$\mathbf{H} = \int_{satellite} \boldsymbol{\rho} \times \dot{\boldsymbol{\rho}} dm \quad (2.4)$$

where $\boldsymbol{\rho}$ is the vector distance from an infinitesimal element of satellite mass to the satellite center of mass and dm is an infinitesimal element of mass. The dot notation

signifies a time derivative. Using the vector identity of Equation 2.2 a second time:

$$\dot{\boldsymbol{\rho}} \equiv \left\{ \frac{d\boldsymbol{\rho}}{dt} \right\}_I = \left\{ \frac{d\boldsymbol{\rho}}{dt} \right\}_B + \boldsymbol{\Omega} \times \boldsymbol{\rho} \quad (2.5)$$

Note that $\{d\boldsymbol{\rho}/dt\}_B = 0$ for a rigid body. Equation 2.4 then becomes:

$$\mathbf{H} = \int \boldsymbol{\rho} \times (\boldsymbol{\Omega} \times \boldsymbol{\rho}) dm \quad (2.6)$$

Resolving $\boldsymbol{\Omega}$ and $\boldsymbol{\rho}$ into the body frame yields:

$$\boldsymbol{\Omega} = \Omega_1 \hat{\mathbf{b}}_1 + \Omega_2 \hat{\mathbf{b}}_2 + \Omega_3 \hat{\mathbf{b}}_3 \quad (2.7)$$

and

$$\boldsymbol{\rho} = \rho_1 \hat{\mathbf{b}}_1 + \rho_2 \hat{\mathbf{b}}_2 + \rho_3 \hat{\mathbf{b}}_3 \quad (2.8)$$

Use the vector triple product formula on Equation 2.6 to give:

$$\mathbf{H} = \int \begin{bmatrix} \Omega_1 \\ \Omega_2 \\ \Omega_3 \end{bmatrix} (\rho_1^2 + \rho_2^2 + \rho_3^2) - \begin{bmatrix} \rho_1 \\ \rho_2 \\ \rho_3 \end{bmatrix} (\Omega_1 \rho_1 + \Omega_2 \rho_2 + \Omega_3 \rho_3) dm \begin{bmatrix} b_1 \\ b_2 \\ b_3 \end{bmatrix} \quad (2.9)$$

Rearranging produces:

$$\mathbf{H} = \begin{bmatrix} \Omega_1 \int (\rho_2^2 + \rho_3^2) dm - \Omega_2 \int \rho_1 \rho_2 dm - \Omega_3 \int \rho_1 \rho_3 dm \\ \Omega_2 \int (\rho_1^2 + \rho_3^2) dm - \Omega_3 \int \rho_2 \rho_3 dm - \Omega_1 \int \rho_2 \rho_1 dm \\ \Omega_3 \int (\rho_1^2 + \rho_2^2) dm - \Omega_1 \int \rho_3 \rho_1 dm - \Omega_2 \int \rho_3 \rho_2 dm \end{bmatrix} \begin{bmatrix} b_1 \\ b_2 \\ b_3 \end{bmatrix} \quad (2.10)$$

If the following integrals are defined,

$$\begin{aligned} I_{11} &= \int (\rho_2^2 + \rho_3^2) dm & I_{12} = I_{21} &= - \int \rho_1 \rho_2 dm \\ I_{22} &= \int (\rho_1^2 + \rho_3^2) dm & I_{13} = I_{31} &= - \int \rho_1 \rho_3 dm \\ I_{33} &= \int (\rho_1^2 + \rho_2^2) dm & I_{23} = I_{32} &= - \int \rho_2 \rho_3 dm \end{aligned} \quad (2.11)$$

Assuming all future vector components resolved in the body axes, equation 2.10 becomes:

$$\mathbf{H} = \begin{bmatrix} I_{11} & I_{12} & I_{13} \\ I_{21} & I_{22} & I_{23} \\ I_{31} & I_{32} & I_{33} \end{bmatrix} \begin{bmatrix} \Omega_1 \\ \Omega_2 \\ \Omega_3 \end{bmatrix} \equiv \mathbf{I}\boldsymbol{\Omega} \quad (2.12)$$

where \mathbf{I} is the satellite inertia matrix. Substituting Equation 2.12 into Equation 2.3 establishes Euler's rigid body rotational equation of motion:

$$\mathbf{M} = \mathbf{I}\dot{\boldsymbol{\Omega}} + \boldsymbol{\Omega} \times (\mathbf{I}\boldsymbol{\Omega}) \quad (2.13)$$

If the body axes are chosen to be the principle axes,

$$\mathbf{I} = \begin{bmatrix} I_{11} & 0 & 0 \\ 0 & I_{22} & 0 \\ 0 & 0 & I_{33} \end{bmatrix} \quad (2.14)$$

and if the applied moment is resolved into the body frame,

$$\mathbf{M} = M_1 \hat{\mathbf{b}}_1 + M_2 \hat{\mathbf{b}}_2 + M_3 \hat{\mathbf{b}}_3 \quad (2.15)$$

then Equation 2.13 becomes the following three scalar equations:

$$M_1 = I_{11}\dot{\Omega}_1 + (I_{33} - I_{22})\Omega_2\Omega_3 \quad (2.16a)$$

$$M_2 = I_{22}\dot{\Omega}_2 + (I_{11} - I_{33})\Omega_3\Omega_1 \quad (2.16b)$$

$$M_3 = I_{33}\dot{\Omega}_3 + (I_{22} - I_{11})\Omega_1\Omega_2 \quad (2.16c)$$

Assume reaction wheels are used for pointing control and are now included in the model. Also assume that the three identically-constructed reaction wheels are aligned with the body axes. Applying Euler's rigid body rotational equation of motion (Equations 2.13) to the reaction wheels produces:

$$M_i \hat{\mathbf{b}}_i = I_{rw}(\dot{\omega}_i - \dot{\Omega}_i)\hat{\mathbf{b}}_i + (\omega_i - \Omega_i)\hat{\mathbf{b}}_i \times I_{rw}(\omega_i - \Omega_i)\hat{\mathbf{b}}_i, \quad i = 1, 2, 3 \quad (2.17)$$

where i is body axis number, M_i is the reaction moment of the wheel on the satellite, I_{rw} is the scalar reaction wheel MOI about its rotational axis, ω_i is the reaction wheel velocity relative to the body axes and $(\omega_i - \Omega_i)$ is the reaction wheel velocity with respect to the inertial frame. Since I_{rw} is a scalar and the cross-product of any quantity with itself is zero, the reaction wheel scalar moments become:

$$M_i = I_{rw}(\dot{\omega}_i - \dot{\Omega}_i), \quad i = 1, 2, 3 \quad (2.18)$$

Solving for the body rates generates the rigid body dynamics of the system:

$$\dot{\Omega}_1 = -\frac{\dot{\omega}_1 I_{rw}}{I_{11} + I_{rw}} + \frac{\Omega_2 \Omega_3 (I_{22} - I_{33})}{I_{11} + I_{rw}} \quad (2.19a)$$

$$\dot{\Omega}_2 = -\frac{\dot{\omega}_2 I_{rw}}{I_{22} + I_{rw}} + \frac{\Omega_3 \Omega_1 (I_{33} - I_{11})}{I_{22} + I_{rw}} \quad (2.19b)$$

$$\dot{\Omega}_3 = -\frac{\dot{\omega}_3 I_{rw}}{I_{33} + I_{rw}} + \frac{\Omega_1 \Omega_2 (I_{11} - I_{22})}{I_{33} + I_{rw}} \quad (2.19c)$$

These equations relate the motion of the satellite in inertial coordinates to the mass properties (MOIs) of the satellite system, the reaction wheel angular accelerations, and the satellite orientation.

2.2.2 Rotational Kinematics. The rotational kinematics of the system connect the rotational motion sensed by the satellite to the motion sensed by a stationary (inertial) observer. In order to find and propagate the absolute orientation of the satellite, the body angular velocities in the dynamics equations must be related to the inertial orientation and orientation rates. One of several different methods are commonly used to arrive at this relationship.

Three consecutive single-axis rotations are used in this thesis to describe the orientation of the satellite relative to an inertial frame. Starting at the inertial frame (a frame) and following Wie [41] and Stevens and Lewis [34]:

1. Rotate about the a_3 -axis an angle ψ
2. Rotate about the new a'_2 -axis an angle θ
3. Rotate about the new a''_1 -axis an angle ϕ

where ψ is the yaw angle, θ is the pitch angle, and ϕ is the roll angle. Figure 2.3 illustrates the three single-axis rotations.

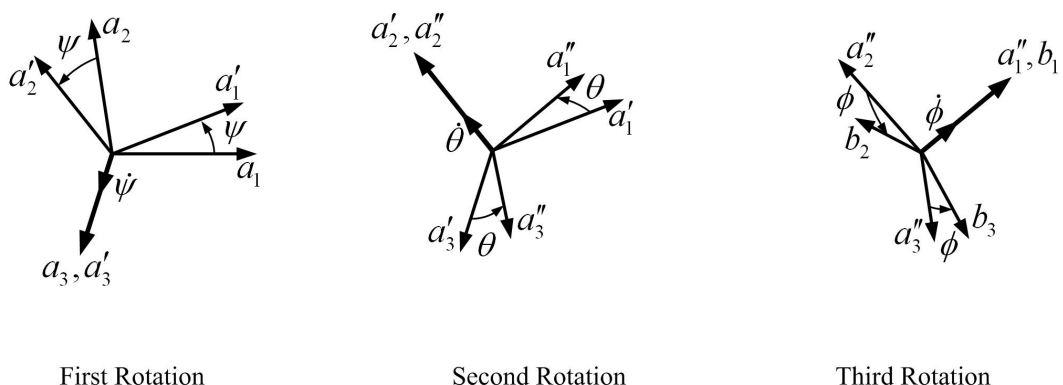


Figure 2.3 Kinematic Single-Axis Rotations

From Figure 2.3 define:

$$\begin{Bmatrix} a'_1 \\ a'_2 \\ a'_3 \end{Bmatrix} = \mathbf{C}_3(\psi) \begin{Bmatrix} a_1 \\ a_2 \\ a_3 \end{Bmatrix} \quad (2.20a)$$

$$\begin{Bmatrix} a''_1 \\ a''_2 \\ a''_3 \end{Bmatrix} = \mathbf{C}_2(\theta) \begin{Bmatrix} a'_1 \\ a'_2 \\ a'_3 \end{Bmatrix} \quad (2.20b)$$

$$\begin{Bmatrix} b_1 \\ b_2 \\ b_3 \end{Bmatrix} = \mathbf{C}_1(\phi) \begin{Bmatrix} a''_1 \\ a''_2 \\ a''_3 \end{Bmatrix} \quad (2.20c)$$

where:

$$\mathbf{C}_3(\psi) = \begin{bmatrix} \cos(\psi) & \sin(\psi) & 0 \\ -\sin(\psi) & \cos(\psi) & 0 \\ 0 & 0 & 1 \end{bmatrix} \quad (2.21a)$$

$$\mathbf{C}_2(\theta) = \begin{bmatrix} \cos(\theta) & 0 & -\sin(\theta) \\ 0 & 1 & 0 \\ \sin(\theta) & 0 & \cos(\theta) \end{bmatrix} \quad (2.21b)$$

$$\mathbf{C}_1(\phi) = \begin{bmatrix} 1 & 0 & 0 \\ 0 & \cos(\phi) & \sin(\phi) \\ 0 & -\sin(\phi) & \cos(\phi) \end{bmatrix} \quad (2.21c)$$

Combine Equations 2.21a–c with Equations 2.20a–c to get:

$$\begin{Bmatrix} b_1 \\ b_2 \\ b_3 \end{Bmatrix} = \mathbf{C}_1(\phi)\mathbf{C}_2(\theta)\mathbf{C}_3(\psi) \begin{Bmatrix} a_1 \\ a_2 \\ a_3 \end{Bmatrix} \quad (2.22)$$

or explicitly,

$$\begin{Bmatrix} b_1 \\ b_2 \\ b_3 \end{Bmatrix} = \begin{bmatrix} c_\theta c_\psi & c_\theta s_\psi & -s_\theta \\ -c_\phi s_\psi + s_\phi s_\theta c_\psi & c_\phi c_\psi + s_\phi s_\theta s_\psi & s_\phi c_\theta \\ s_\phi s_\psi + c_\phi s_\theta c_\psi & -s_\phi c_\psi + c_\phi s_\theta s_\psi & c_\phi c_\theta \end{bmatrix} \begin{Bmatrix} a_1 \\ a_2 \\ a_3 \end{Bmatrix} \quad (2.23)$$

where the abbreviated forms: $c_\alpha = \cos(\alpha)$ and $s_\alpha = \sin(\alpha)$ are used.

The Euler rates are the time derivatives of the Euler angles. From Figure 2.3,

$$\boldsymbol{\Omega} = \dot{\phi} \hat{\mathbf{b}}_1 + \dot{\theta} \hat{\mathbf{a}}_2'' + \dot{\psi} \hat{\mathbf{a}}_3' \quad (2.24)$$

which can be written:

$$\boldsymbol{\Omega} = \begin{Bmatrix} b_1 & b_2 & b_3 \end{Bmatrix} \begin{bmatrix} \dot{\phi} \\ 0 \\ 0 \end{bmatrix} + \begin{Bmatrix} a_1'' & a_2'' & a_3'' \end{Bmatrix} \begin{bmatrix} 0 \\ \dot{\theta} \\ 0 \end{bmatrix} + \begin{Bmatrix} a_1' & a_2' & a_3' \end{Bmatrix} \begin{bmatrix} 0 \\ 0 \\ \dot{\psi} \end{bmatrix} \quad (2.25)$$

Substitute

$$\boldsymbol{\Omega} = \begin{Bmatrix} b_1 & b_2 & b_3 \end{Bmatrix} \begin{bmatrix} \Omega_1 \\ \Omega_2 \\ \Omega_3 \end{bmatrix} \quad (2.26)$$

and

$$\begin{Bmatrix} a_1'' & a_2'' & a_3'' \end{Bmatrix} = \begin{Bmatrix} b_1 & b_2 & b_3 \end{Bmatrix} \mathbf{C}_1(\phi) \quad (2.27)$$

$$\begin{Bmatrix} a_1' & a_2' & a_3' \end{Bmatrix} = \begin{Bmatrix} b_1 & b_2 & b_3 \end{Bmatrix} \mathbf{C}_1(\phi) \mathbf{C}_2(\theta) \quad (2.28)$$

into Equation 2.25 to get:

$$\begin{aligned} \begin{bmatrix} \Omega_1 \\ \Omega_2 \\ \Omega_3 \end{bmatrix} &= \begin{bmatrix} \dot{\phi} \\ 0 \\ 0 \end{bmatrix} + \mathbf{C}_1(\phi) \begin{bmatrix} 0 \\ \dot{\theta} \\ 0 \end{bmatrix} + \mathbf{C}_1(\phi)\mathbf{C}_2(\theta) \begin{bmatrix} 0 \\ 0 \\ \dot{\psi} \end{bmatrix} \\ &= \begin{bmatrix} 1 & 0 & -s_\theta \\ 0 & c_\phi & s_\phi c_\theta \\ 0 & -s_\phi & c_\phi c_\theta \end{bmatrix} \begin{bmatrix} \dot{\phi} \\ \dot{\theta} \\ \dot{\psi} \end{bmatrix} \end{aligned} \quad (2.29)$$

Invert Equation 2.29 to get the Euler rates:

$$\begin{bmatrix} \dot{\phi} \\ \dot{\theta} \\ \dot{\psi} \end{bmatrix} = \frac{1}{c_\theta} \begin{bmatrix} c_\theta & s_\phi s_\theta & c_\phi s_\theta \\ 0 & c_\phi c_\theta & -s_\phi c_\theta \\ 0 & s_\phi & c_\phi \end{bmatrix} \begin{bmatrix} \Omega_1 \\ \Omega_2 \\ \Omega_3 \end{bmatrix} \quad (2.30)$$

The singularity at $\theta = 90^\circ$ is not an issue due to the small size of the maneuvers used in this research for this technique. Also, the experimental equipment is not capable of this attitude.

2.2.3 Satellite Controller. Most satellites spend their entire operational life under feedback control in order to maintain their desired orientation. A detection technique that uses this closed-loop control is desirable from an operational viewpoint, but complicates the analysis. If open-loop tests were feasible, a simple calculation, such as the one in Section 3.4.1, used as the truth model, could be employed. However, a closed-loop detection scheme has the opportunity to collect data from every routine motion of the satellite, thereby being transparent to the user. This type of technique measures the closed-loop response and separates the satellite characteristics from the controller-induced motion.

In this effort, a Proportional Plus Derivative (PD) controller was used for satellite pointing control. This type of controller is similar to controllers found on

some operational satellites. The HST was deployed with a Proportional Plus Integral Plus Derivative (PID) controller [2]. The addition of the integral term allows control of constant applied torques. These are generally second order effects, not present in the hardware simulator and therefore integral control was not included in this effort.

A PD controller responds to the magnitude and rate of change of the error. In general, PD control is mathematically defined in the frequency (Laplace) domain as:

$$U(s) = K_P + K_D s \quad (2.31)$$

where K_P is the proportional gain constant, K_D is the derivative gain constant, and s is the Laplace variable. In the time domain:

$$u(t) = K_P e(t) + K_P T_D \frac{de(t)}{dt} \quad (2.32)$$

where T_D is the derivative time constant, and e is the control error. Figure 2.4 is a functional representation of the PD controller implemented.

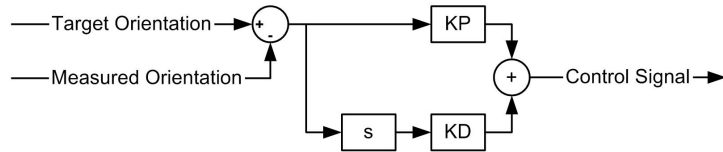


Figure 2.4 Satellite Proportional Plus Derivative Controller

2.2.4 Reaction Wheel System. The reaction wheel motor systems incorporate closed-loop control with a dedicated motor controller. This PID controller with velocity and acceleration feed-forward control action is combined with the motor, amplifier, and encoder in a single unit. Due to the proprietary nature of the motor used (Animatics Corporation), an exact model is unavailable. It is assumed the controller is a standard design as shown in Figure 2.5. Without a definite model of the motor control system, it was decided to model the motor empirically using a look-up

table (See Section 3.4.2). This was necessary for the success of this effort because the response of the motor directly affects the response of the satellite to commands or disturbances such as debris collisions or docking.

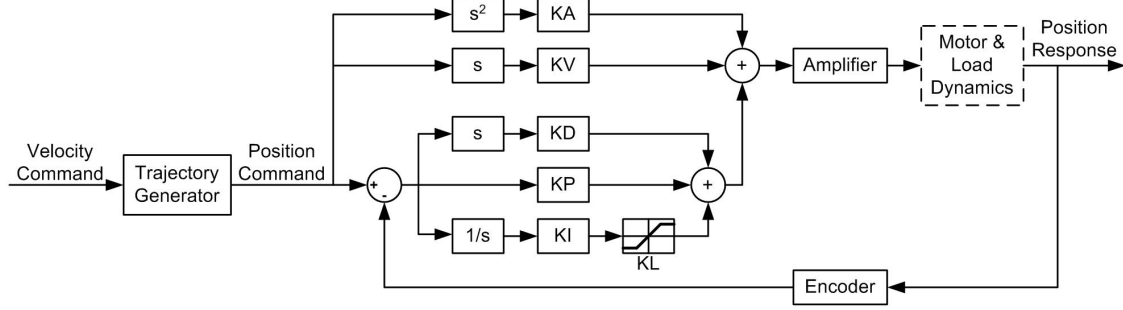


Figure 2.5 Proportional Plus Integral Plus Derivative with Velocity Feed-Forward and Acceleration Feed-Forward Motor Controller

2.3 Docking Event Detection

Detection of a docking event can be difficult given that the detectable result of slowly connecting two spacecraft is very similar to the result of a routine collision with a micrometeoroid or piece of space debris traveling at high velocity. To gain insight into this similarity, consider the following derivation and subsequent simulations.

The space debris impact is modeled as an impulsive angular acceleration. The disturbance acceleration can be calculated from the conservation of angular momentum since the angular momentum immediately before and after the collision event must match:

$$\sum_{i=1}^n \mathbf{H}_i \Big|_{Pre-Collision} = \sum_{i=1}^n \mathbf{H}_i \Big|_{Post-Collision} \quad (2.33)$$

where i is the number of the element under consideration and n is the total number of elements. Specifically,

$$[\mathbf{H}_{s/c} + \mathbf{H}_{debris}]_{Pre-Collision} = [\mathbf{H}_{s/c} + \mathbf{H}_{debris}]_{Post-Collision} \quad (2.34)$$

where $\mathbf{H}_{s/c}$ is the angular momentum of the spacecraft system and \mathbf{H}_{debris} is the angular momentum of the space debris. If the satellite starts at rest ($\mathbf{H}_{s/c} = 0$), and the debris is destroyed/embedded after collision in a perfectly inelastic collision ($\mathbf{H}_{debris} = 0$):

$$\mathbf{r} \times \mathbf{p} = \mathbf{I}\boldsymbol{\Omega} \quad (2.35)$$

where \mathbf{r} is the position vector from the spacecraft center of mass to the point of impact and \mathbf{p} is the linear momentum of the debris. Resolving \mathbf{r} and \mathbf{p} into the body frame produces:

$$\mathbf{r} = \begin{bmatrix} r_1 \\ r_2 \\ r_3 \end{bmatrix} \quad (2.36)$$

and

$$\mathbf{p} = m_{particle} \begin{bmatrix} v_1 \\ v_2 \\ v_3 \end{bmatrix} \quad (2.37)$$

where $m_{particle}$ is the debris mass. Solving for $\boldsymbol{\Omega}$ produces:

$$\Omega_1 = m_{particle} \frac{r_2 v_3 - r_3 v_2}{I_{11}} \quad (2.38a)$$

$$\Omega_2 = m_{particle} \frac{r_3 v_1 - r_1 v_3}{I_{22}} \quad (2.38b)$$

$$\Omega_3 = m_{particle} \frac{r_1 v_2 - r_2 v_1}{I_{33}} \quad (2.38c)$$

To be conservative and present the most detectable case, the maximum single-axis collision is considered (all relative velocity in one body axis). Without loss of generality:

$$\Omega_2 = m_{particle} \frac{r_3 v_1}{I_{22}} \quad (2.39)$$

Integrating discretely yields:

$$\dot{\Omega}_2 = m_{particle} \frac{r_3 v_1}{I_{22} t_{step}} \quad (2.40)$$

where t_{step} is the simulation timestep. Similarly for a docking event:

$$\dot{\Omega}_2 = m_{parasite} \frac{r_3 v_1}{I_{new|22} t_{step}} \quad (2.41)$$

where $m_{parasite}$ is the parasite mass and I_{new} is the new combined satellite and microsatellite MOI.

The fundamental difference between a debris collision and docking event is what happens after the acceleration is imparted to the satellite. In a collision, the satellite MOI remains unchanged (the mass of the particle is negligible) while after the docking event the satellite MOI is increased by some ΔMOI .

Obviously, it is most stealthy for a parasite to be light (minimize $m_{parasite}$) and dock slowly (minimize v), closest to the center of mass of the target (minimize r). Additionally, to minimize post-dock roll, the relative velocity vector must align with the center of mass. For a microsat approaching very slowly from the rear (motion in the b_1 direction), this condition is closely met, leaving relative velocity control and mating location as the important control variables. Figure 2.6 depicts how a satellite might be targeted based on its center of mass.

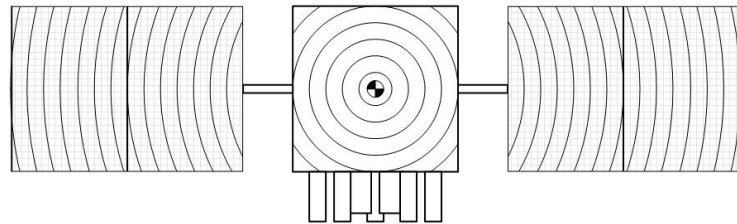


Figure 2.6 Satellite Targeted Based on Center of Mass Location

Microsats generally have very small impulse bits available, allowing for very fine control of closing velocity (as discussed previously in Section 1.1 on micropulsion). With a good relative position measurement, this could lead to very soft attachment. For manned docking maneuvers, Brody [4] utilizes 0.15 m/s as the critical speed between failure and success. Takezawa *et al.* [35] plan to use 0.01 m/s for the low-impact docking of a 5 kg nanosat.

To gain insight into collision versus docking differences, a simulation was performed. The results are shown in Figures 2.7–2.9. Figure 2.7 illustrates a low-fidelity docking by a relatively large parasite compared to a debris collision of the same magnitude. The impact speed is 1 m/s, 2.5 m off-target, and increases the target's MOI by approximately 23%. Figure 2.8 is a moderate-fidelity docking and Figure 2.9 is a higher-fidelity docking with an impact speed of 0.01 m/s, 0.1 m off-target, adding only 3.4% to the target's MOI.

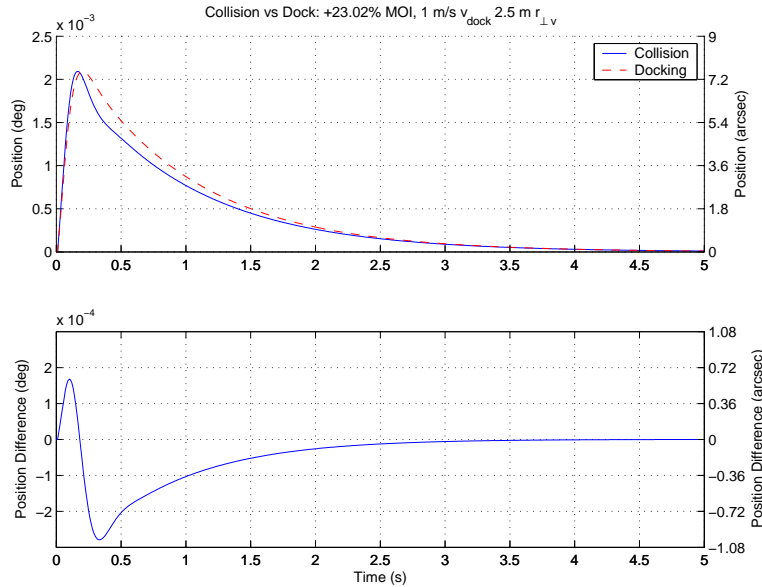


Figure 2.7 Comparison of a Low-Fidelity Docking Versus a Debris Collision of Equal Magnitude

It becomes apparent that even operators of high tech imaging satellites with strict pointing requirements and sensitive gyroscopes will have trouble differentiating

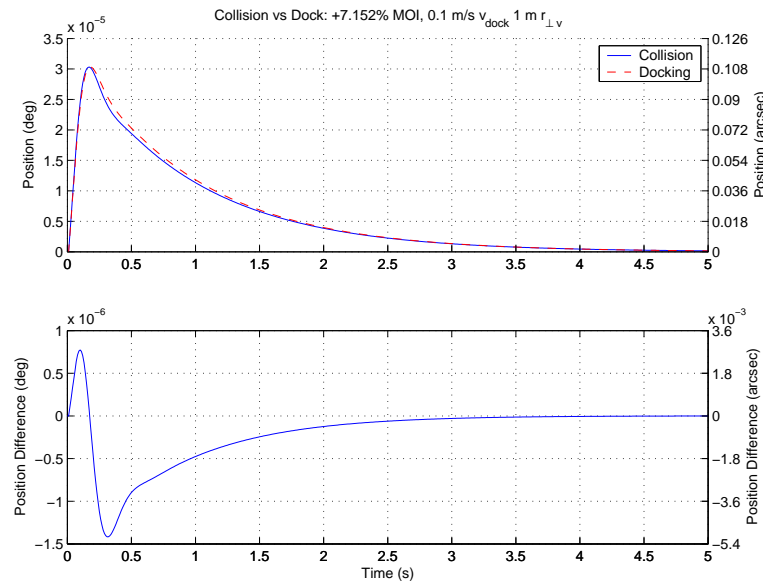


Figure 2.8 Comparison of a Moderate-Fidelity Docking Versus a Debris Collision of Equal Magnitude

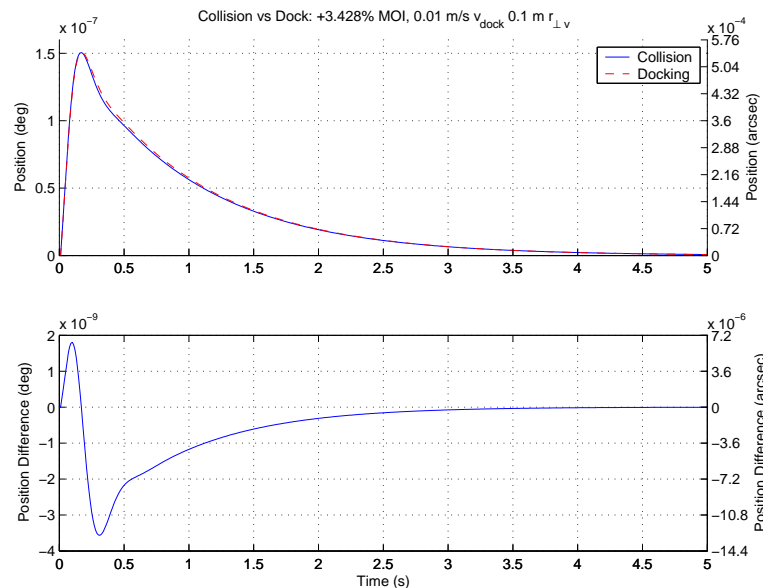


Figure 2.9 Comparison of a High-Fidelity Docking Versus a Debris Collision of Equal Magnitude

differences on the order of $1 \cdot 10^{-5}$ arcsec from noise. The detection is actually even more formidable than these results suggests. If by chance, or by skill, the microsat docks so that its velocity vector nearly intersects the target's center of mass, the resulting response could be orders of magnitude less than presented above. This type of connection would have no other effect than a undetectable rotation and an undetectable in-track change of velocity—one of the most difficult orbit determination parameters to estimate.

Furthermore, if equipped with reaction wheels, solar panels, and a strong attachment mechanism, it is conceivable that additional stealth could be attained through the use of the microsat's own attitude control system. Walker [38] has done research in this area with the intent of righting and continuing to provide attitude control for a distressed satellite. A parasite might be able to routinely generate enough torque to null its own effect on the host satellite.

2.4 Dynamic Detection

As opposed to detecting a single event (docking), dynamic detection senses changes in the response of the satellite to a known input. By creating a model that accurately represents the nominal reactions of the spacecraft, alterations to the spacecraft configuration can be sensed. An angular step command sequence was chosen as the detection maneuver due to its familiarity, repeatability, and cost-effectiveness (no fuel expended). A one degree magnitude step was arbitrarily picked as a starting point. This was determined to be large enough for detection purposes, but small enough to minimize pointing errors, fuel, and time spent in the maneuver.

Since validation hardware was available for testing this technique, a software simulation was unnecessary. The experimental process, however, follows.

Nominally, the detection maneuver is performed multiple times on the physical system, recording the subsequent response. The model is then altered to match this response. Tunable parameters such as look-up tables, delays, structural stiffness,

etc. can be changed to get a best fit. Factors such as mass and MOIs (which are known) are held constant. To find the best fit, a minimization of a least squares-type cost function was employed:

$$J = \sum_{i=1}^n \left\| \frac{\mathbf{y}_{actual}|_i - \mathbf{y}_{model}|_i}{n} \right\| \quad (2.42)$$

where J is the cost function, i is the timestep number, n is number of timesteps, \mathbf{y}_{actual} is the time history of the satellite response, and \mathbf{y}_{model} is the time history of the model response. In this case the cost is simply the mean mismatch between the satellite and modeled responses.

Next, the MOI is changed. The detection maneuver is performed post-dock and the response is fit to the nominal model response, by once again minimizing a least squares-type cost function. Now only the MOIs are given the freedom to change and, thus, be estimated. Functionally:

$$\text{Min } J(\Delta I_{ii}) \quad i = 1, 2, 3 \quad (2.43)$$

where i is the axis number. The revised cost function for detection is

$$J = \sum_{i=1}^n \left\| \frac{\mathbf{y}_{model}|_i - \mathbf{y}_{test}|_i}{n} \right\| \quad (2.44)$$

where \mathbf{y}_{test} is the time history of the satellite response to be tested.

It became necessary to construct a new minimization routine for this purpose because the cost as a function of MOI has multiple local minima which many “canned” routines can not handle reliably. The routine employed here simply runs the model over a wide range of MOIs, finds the minimum cost, and repeats the process on a smaller range. The number of points tested per range of MOIs is held constant. The routine stops when the convergence criteria is reached. For all tests

in this document, the minimization was stopped at a normalized MOI precision of $1 \cdot 10^{-6}$. The minimization code is contained in Appendix C.

2.5 Summary

An overview of the body of research for on-orbit system ID techniques and on-orbit MOI estimation has been presented. The dynamics and kinematics of a reaction wheel-oriented satellite were derived. This baseline model was expanded to include either a collision or a docking event and employed to investigate the differences between the two. It was determined that for a docking with moderate to high fidelity, the two events were indistinguishable based on time history data. A motion-based detection algorithm was developed to sense the change in MOI due to the additional mass of the microsat. This technique was tested using the hardware described in Chapter III.

III. Characterization of Experimental Equipment

SIMSAT was originally developed by AFIT’s 1999 Systems Engineering Team “to simulate satellite behavior with as much fidelity as possible [8].” Design goals included:

- Initial cost under \$100K
- One year to initial operating capability
- Support for spin, “dual” spin, 3-axis rigid, and flexible structure experiments
- Ability to host experimental payloads
- Simple operation

The SIMSAT System is made of three main parts: the air bearing assembly which provides near-frictionless rotational motion, the satellite assembly which provides satellite functionality, and the ground-station computer which provides real-time command/data transmission. The air bearing and satellite assembly are illustrated in Figure 3.1.

An exhaustive description of the original SIMSAT configuration can be found in [8]. The major upgrades included as part of this effort can be summarized as follows:

- Integrated New Digital Reaction Wheel Motors
 - Rewired Motors for Individual Communications and Modularity
 - Wrote Digital Communications Software Package
 - Tuned 8-Parameter Motor Controller
 - Created an Integrated Initialization Package
- Upgraded Onboard Computer

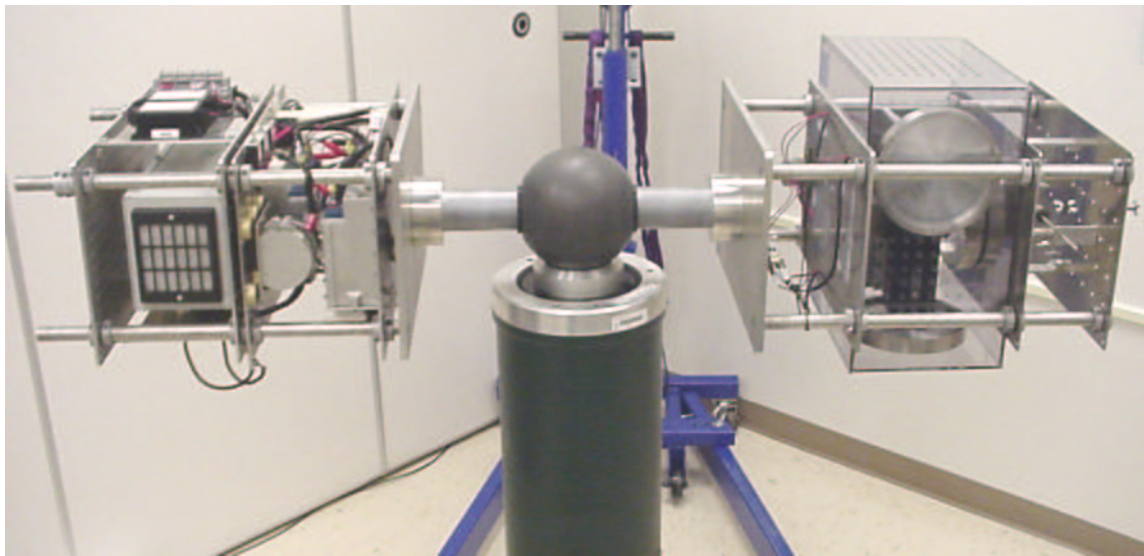


Figure 3.1 Satellite Assembly and Air Bearing

- Integrated New Real-Time Processor Board
- Integrated New Multi-Function Central Processing Unit Board
- Integrated New Digital Input/Output Board
- Upgraded Existing Analog to Digital Board
- Modified Onboard Computer Ventilation for “Zero-Moment” Operation
- Replaced Onboard Batteries
- Upgraded Ground-Station Computer
 - Upgraded dSPACE® Software
 - Upgraded MATLAB®/Simulink® Software
 - Upgraded Wireless Local Area Network Board
- Rerouted Room Ventilation System for “Zero-Moment” Operation

3.1 Air Bearing Assembly

Flotation is achieved through the use of a Space Electronics, Inc. Model SE9791 Tri-axis Spherical Air Bearing. The assembly consists of a spherical rotor, hollow

shaft, mounting flanges, pedestal, and air compressor. Figure 3.2 illustrates the configuration.

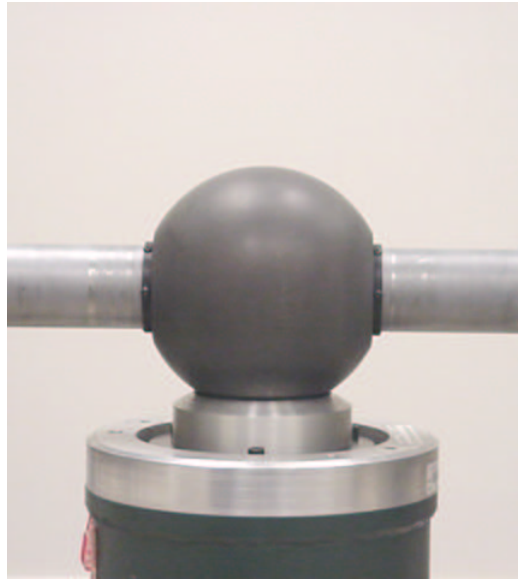


Figure 3.2 Space Electronics, Inc. Model SE9791 Tri-axis Spherical Air Bearing

While in operation, compressed air, at approximately 500 kPa, is supplied through the pedestal into six jets in the air bearing cup. The rotor rides on a cushion of air less than $12.7 \mu\text{m}$ thick. If a coordinate system is defined for maximum range of motion, two body axes are unrestricted and a third restricted to $\pm 25^\circ$ due to contact of the satellite assembly with the pedestal.

3.2 Satellite Assembly

The satellite assembly consists of the structure, attitude determination subsystem, attitude control subsystem, command and data handling subsystem, power subsystem, and other systems.

3.2.1 Structure. The SIMSAT structure consists of a central spherical rotor connected to a hollow mounting shaft. Each end of the mounting shaft is connected to a separate box truss creating a “barbell-shaped” structure. The box

truss is made from aluminum plates and stainless steel mounting rods. The aluminum plates are 53 cm tall by 35 cm wide and vary from a constant 12.7 mm to 2.38 mm in thickness. Each plate has four 24.5 mm diameter holes to allow the mounting rods to pass through. The eight 24.5 mm stainless steel mounting rods are 60 cm in length. Collars connect the aluminum plates to the stainless steel mounting rods.

3.2.2 Attitude Determination. The Humphrey Model CF-75-0201-1 Axis Rate Gyroscope was used for attitude determination. It provided angular velocity and linear acceleration in three axes. Only angular velocity data was used in this experiment. Table 3.1 provides the manufacturer's performance data.

Table 3.1 Humphrey Model CF-75-0201-1 Axis Rate Gyroscope Characteristics

Parameter	Value
Roll Rate Range	± 120 deg/sec
Roll Accuracy (Half Range)	1.2 deg/sec
Roll Accuracy (Full Range)	4.8 deg/sec
Pitch/Yaw Rate Range	± 40 deg/sec
Pitch/Yaw Accuracy (Half Range)	0.6 deg/sec
Pitch/Yaw Accuracy (Full Range)	2.4 deg/sec

McMaster-Carr Natural Rubber Plate Form Mounts insulate the gyroscope from the main SIMSAT structure. Figure 3.3 illustrates the installation.

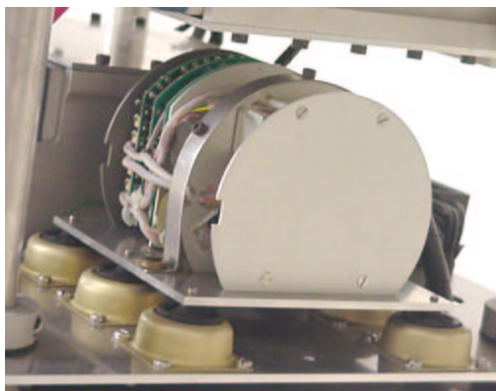


Figure 3.3 Humphrey CF-75-0201-1 Axis Rate Gyroscope and Mounting

This gyroscope was best suited for short term, large magnitude maneuvers. An attempt was made to upgrade this instrument (see Appendix A).

3.2.3 Attitude Control. Three reaction wheels, one per axis, provide attitude control. A perforated Lexan® box encloses the reaction wheel grouping. The configuration is illustrated in Figure 3.4.

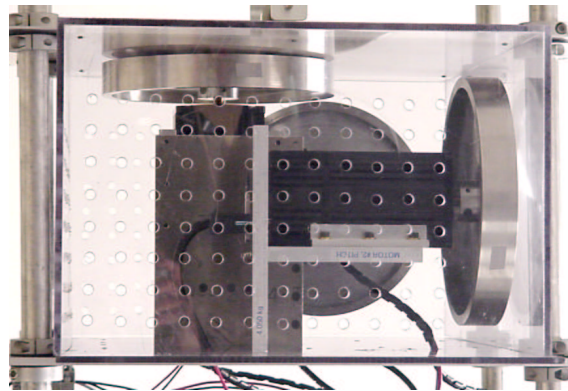


Figure 3.4 Reaction Wheel Cluster

3.2.3.1 Reaction Wheel Motors. The original SIMSAT configuration has been upgraded to use Animatics SmartMotor™ Model SM3450 Motor Systems to drive the flywheels. Each motor system integrates a brushless DC servo motor, motion controller, encoder and amplifier into a single package. Motor characteristics are listed in Table 3.2.

Table 3.2 Animatics SmartMotor™ Model SM3450 Motor System Characteristics

Parameter	Value
Weight	2.90 kg
Length	155 mm
Width	82.6 mm
Voltage	36 V
Encoder Resolution	4,000 counts/rev
Data Interface	RS232

The motors were tuned for a compromise of performance and repeatability. See Appendix B for a more detailed account of the tuning process. Table 3.3 lists the motor controller parameters and settings used during testing.

Table 3.3 Animatics SmartMotorTM Model SM3450 Motor System Integrated Controller Settings

Parameter	Value
Proportional Coefficient	25
Integral Coefficient	0
Integral Limit	0
Derivative Coefficient	3,500
Velocity Feed Forward Coefficient	1,000
Acceleration Feed Forward Coefficient	10,000
Error Limit	32,000
Acceleration	25

3.2.3.2 Reaction Wheel Flywheel. The flywheels were fabricated in-house. Each 8.625 in diameter wheel is made of a steel rim attached to a thin aluminum disk. The MOI of the flywheel was calculated to be 1.955×10^{-2} kg·m².

3.2.4 Command and Data Handling. dSPACE[®] Inc. hardware and software is used for onboard command, control and telemetry in real-time. A dSPACE[®] AutoBox[®] DS400 provides the DC computing power and is configured with the following items:

- DS1005 PPC Processor Board
- DS2003 32-Channel A/D Board
- DS2103 32-Channel D/A Board
- DS4201-S 4-Channel Serial Interface Board

Both the processor board and the serial board have been upgraded from the original SIMSAT configuration. The DS1005 is a PowerPC[®] 750 running at 450 MHz

with 128 MB SDRAM, while the DS4201-S supports RS232 communication at speeds up to 115.2 kBaud.

A RadioLAN DockLINK™ Model 408-008 is utilized for real-time wireless command/data transmission at speeds up to 10 Mbps.

3.2.5 Power. Three Power-Sonic® Model PS-12180 rechargeable batteries power SIMSAT. Each 12 V sealed lead-acid battery has a rated capacity of 12 Amp-Hours when discharged at the one hour rate. The bus wiring makes 12 V, 24 V, and 36 V available for subsystem use. All batteries were replaced prior to testing.

3.2.6 Other Systems. Minor systems are also included in the SIMSAT design.

- A fine tuning weight and balance system consisting of steel masses attached to adjustable threaded rods is incorporated into the endplate adjacent to the reaction wheel assembly.
- A low voltage alarm is included to allow adequate time to safely power down and immobilize the system (if necessary).
- A 32 channel analog input/output connection board is installed below the onboard computer for easy reconfiguration and testing.
- A portable hydraulic crane is used to transport the satellite assembly to and from the air bearing pedestal
- A toggle switch cluster is included on SIMSAT to allow each voltage bus to be individually controlled

None of these items were upgraded as part of this effort.

3.3 Ground-Station Computer

All of the hardware and software in the ground-station computer was upgraded from the original configuration.

3.3.1 Hardware. The ground-station computer has been upgraded from the original configuration to a Dell® Dimension® Model 4500. It is driven by an Intel® Pentium® 4 running at 2.26 GHz with 256 MB DDR SDRAM. The original wireless network card was replaced at the same time and is now a RadioLAN PCI CardLINK™ Model RMG-160 with the same throughput of 10 Mbps.

3.3.2 Software. The operating system on the ground-station computer is Microsoft® Windows® 2000. Release 13 of MATLAB® (Version 6.5) and Simulink® (Version 5) is used for modeling, programming and control system design. The following toolboxes are installed: Control System, Signal Processing, Real-Time Workshop®, and Stateflow®. The top level experimental Simulink® model is displayed in Figure 3.5. ControlDesk® Version 2.2.5 is used as the experiment manager (see Appendix F). It integrates with Simulink® and the onboard dSPACE® hardware to allow real-time control and data acquisition.

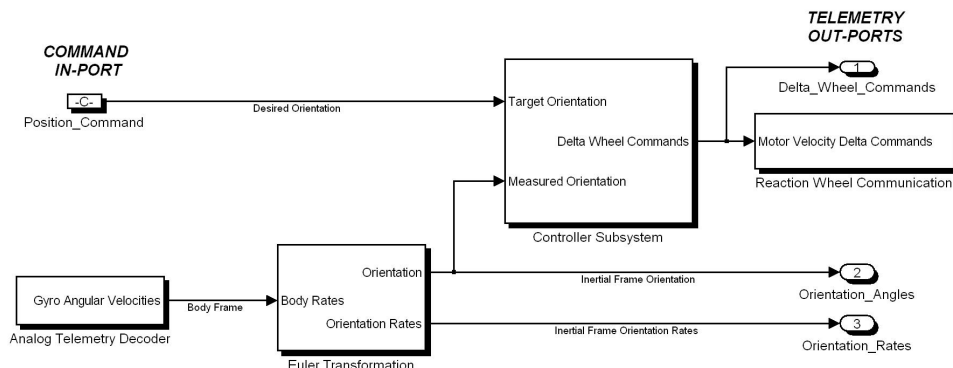


Figure 3.5 Experimental Simulink Satellite Model

3.4 Model Matching

In order to get good agreement between the physical model and the simulation, model parameters must be tuned. Figure 3.6 illustrates the top level Simulink® model used for model tuning. It is functionally identical to Figure 2.1.

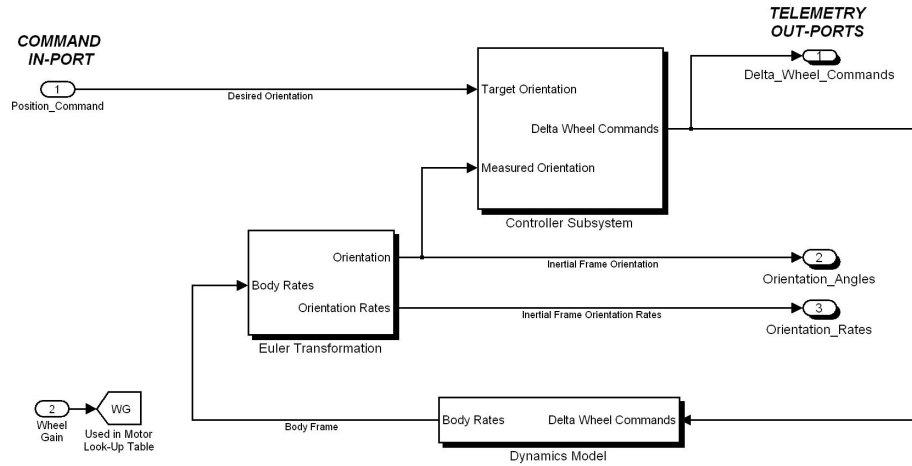


Figure 3.6 Simulation Simulink Satellite Model

The axes of the experimental equipment are configured as in Figure 3.7.

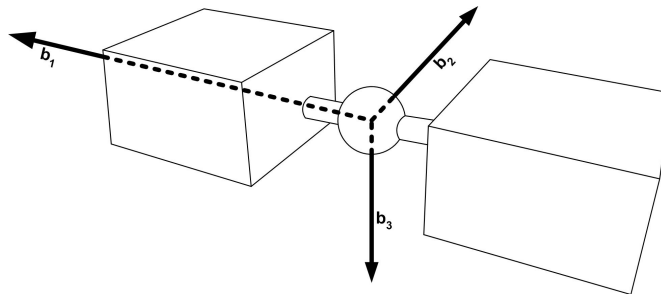


Figure 3.7 SIMSAT Body Axes

3.4.1 Moment of Inertia. The SIMSAT MOI was determined experimentally through conservation of angular momentum:

$$I_{ii} = \frac{I_{rw|i}\Delta\omega_i}{\Delta\Omega_i} \quad (3.1)$$

where i is the body axis number. Each principle axis was determined individually by changing the velocity of the reaction wheel and measuring the resultant satellite motion. Figure 3.8 depicts a single typical test. The slope of the inclined section is SIMSATS angular velocity.

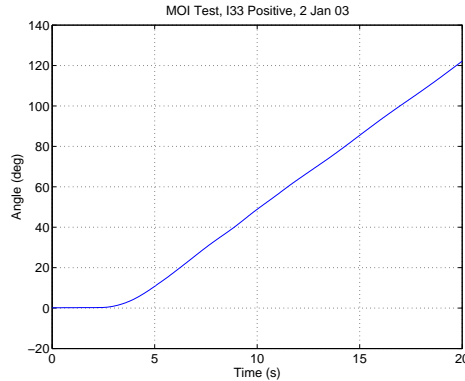


Figure 3.8 Typical SIMSAT MOI Truth Test

Both positive and negative directions were averaged to remove any bias. The result was a baseline MOI matrix:

$$I = \begin{bmatrix} 3.648 & 0 & 0 \\ 0 & 36.78 & 0 \\ 0 & 0 & 35.16 \end{bmatrix} \text{ kg} \cdot \text{m}^2 \quad (3.2)$$

3.4.2 Reaction Wheels. An attempt was made to simulate the reaction wheel motor by using the manufacturer's performance data with unsatisfactory results. A simple look-up table was then designed (Figure 3.9), which when combined with a wheel gain, correlated well with the actual response.

The lookup table was constructed empirically by commanding changes in angular velocity and measuring the resultant angular acceleration. These angular accelerations are the $\dot{\omega}_i$'s of Equations 2.19a–c. The motor is tuned to accelerate at a maximum of 9.92 m/s^2 .

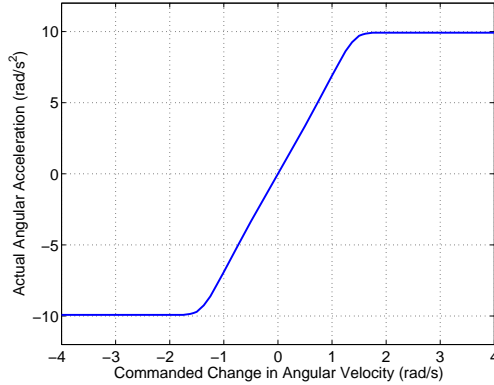


Figure 3.9 Reaction Wheel Look-Up Table Profile

The wheel gain was tuned at the system level to get a best fit for the entire baseline data set. It was the last parameter to be tuned as it was dependent on the magnitude of the detection maneuver.

3.4.3 System Delay. Overall delay was accounted for in the motor model subsystem for convenience. The actual delay takes place in both the motor and on-board computer. Both delay and/or the inclusion of a smoothing (averaging) filter were investigated. While tuning the motors with step commands, some smoothing behavior was observed and considered for incorporation into the model. The output of the smoothing filter was simply the mean of the current input and the last n inputs where n varied from 0–3. A variety of configurations were tested on the system level. Table 3.4 shows that one delay step and no smoothing result in the minimum error.

Table 3.4 Normalized Error Results for Various System Level Delays

Smoothing Steps	Delay Steps			
	0	1	2	3
0	1.284	1.000	1.120	1.656
1	1.103	1.009	1.346	—
2	1.001	1.122	—	—
3	1.007	—	—	—

3.4.4 Detection Maneuver. The detection maneuver consists of four step commands as shown in Figure 3.10. It is symmetric to remove any bias in the response. During the first step, the wheels accelerate in the negative direction, then, maintain a negative speed, until the second step where they return to near zero and vice versa for the second portion of the sequence. Since the motor response is slightly different while speeding up than slowing down (peculiar to SIMSAT's Animatics motors, see Appendix B), the maneuver is designed to include both positive and negative positions. Only the first and third steps are used in the analysis. Figure 3.10 illustrates the 1° detection maneuver. The heavy lines indicate the portion of the command used for matching.

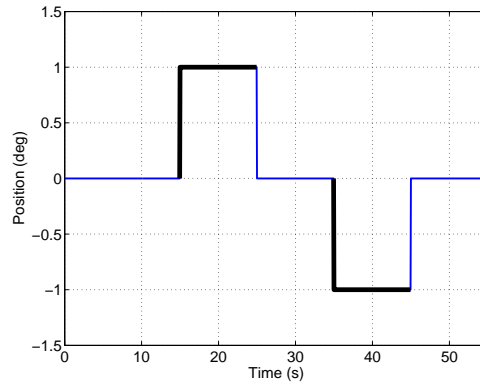


Figure 3.10 One Degree Detection Maneuver

Implementation of the detection maneuver is described in Section 4.1.

3.5 Summary

This chapter provided an overview of the SIMSAT system that was overhauled and used as a test bed to determine the effectiveness of the detection algorithm. Extra steps were taken to characterize system peculiarities necessary for accurate modeling. It was expected that a better model would lead to better results. The test results are presented in the next chapter.

IV. Results and Analysis

This chapter begins with a description of the lab test procedures. Next, baseline data is presented, followed by various methods of detecting the presence and estimating the size of parasite-induced changes in MOI.

4.1 Test Procedure

Experimental single-axis testing of the yaw axis was chosen in order to better isolate the change in behavior, but could easily be expanded to tri-axis testing. The yaw axis was chosen for the following reasons:

1. It best represents on-orbit motion.
2. The gyroscope sensitivity in the pitch axis was larger than the other two axes, which magnified the gyroscope drift and noise, making this a poor choice. See Appendix A.
3. Maneuvers in the roll axis were marred by bending along this axis. Stiffeners were not yet installed at the time of testing.

Even though these irregularities were minor as compared to gross satellite motion, they were deemed undesirable when testing a precision pointing response. Due to the configuration of the lab equipment (See Figure 3.7), a yaw motion in the lab would be most analogous to a pitch or roll motion of a gravity-gradient stabilized satellite on-orbit. The findings and techniques used herein however, are readily adapted to other axes and configurations.

The testing process began with the programming of the ground-station computer to run the detection maneuver. Next, the satellite assembly was floated on the air pedestal, balanced, powered, and positioned. The same starting orientation was achieved by sighting along the satellite assembly to a wall target. High precision

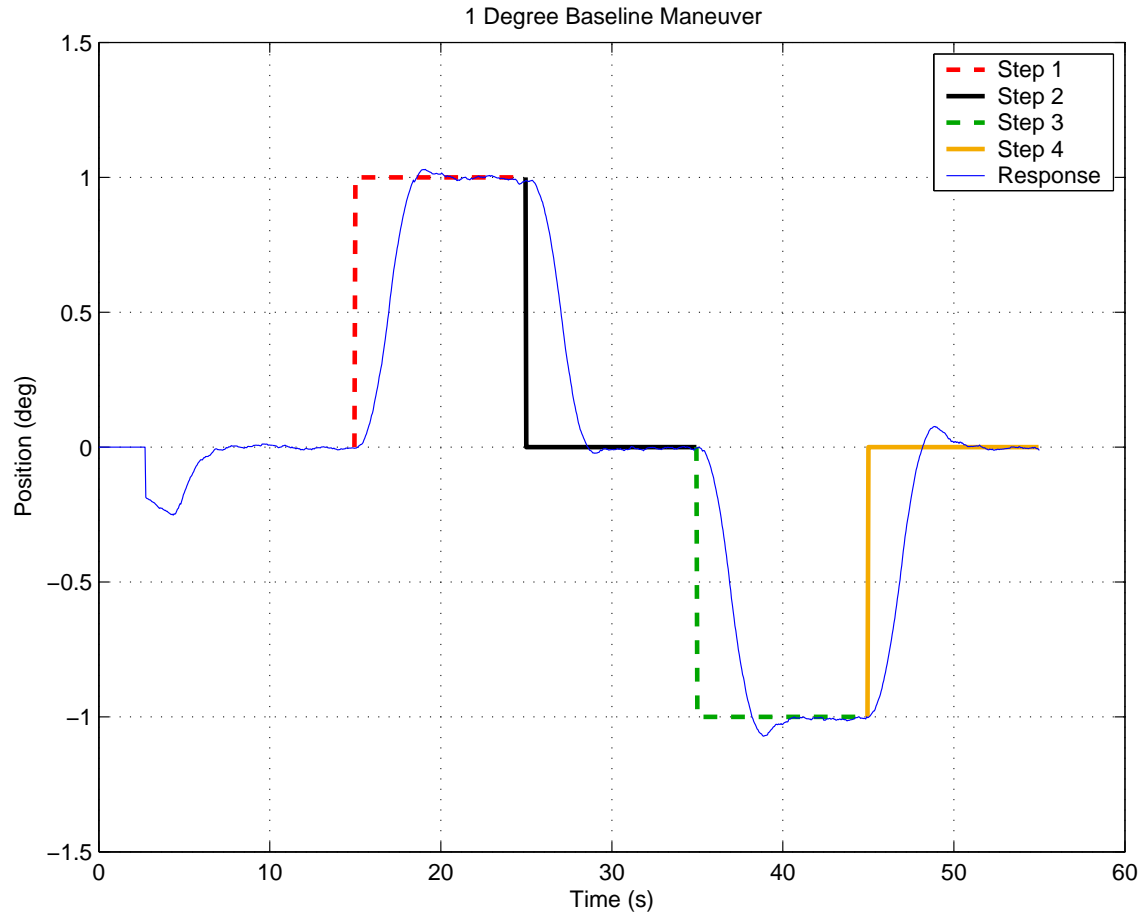


Figure 4.1 Example Data Set

was unnecessary since the satellite was programmed to hold position for the first 15 seconds of the maneuver and gyroscope drift/noise caused some motion before the first step command began (this was unavoidable). The ground computer then started the command sequence and recorded the telemetry. Figure 4.1 is a data set that illustrates most of the peculiarities of the system.

Data collection started after approximately 2.5 seconds. During this time the gyroscope drifted (as well as the satellite to a lesser amount) to approximately -0.2° with a drift rate of approximately -2.5° per minute (in the case shown). This was a typical drift rate for these tests. At approximately 4.25 seconds, the motors had been initialized and began operation. This closed the position error and the satellite

assembly tracked the drift for the remainder of the run. At 15 seconds, the step maneuvers began. Only the first and third step responses were used in the analysis. See Section 3.4.4 for more detail on the maneuver. Notice that the overshoot response on step one was less than that on step three even though these were symmetric commands. This bias due to gyroscope drift was the reason why both steps one and three were used (on-orbit, a simple step command could be utilized). Notice also that the response to steps one and four as well as the response to steps two and three were quite different even though the same relative maneuver was commanded. It was found that the motor response while slowing down was somewhat different than that while speeding up. Refer to Appendix B on motor tuning for further discussion and results. The satellite controller was tuned for a second-order damping ratio of approximately 0.7, yielding an overshoot of approximately 4%. These values yielded a good response that settled quickly.

The gyroscope drift was a minor problem during testing. The drift was random with long period motion on the order one to two minutes. The mean drift was a function of operating temperature—the value changed rapidly after power was applied and slowed to a steady-state mean drift rate after approximately 20–30 minutes. Testing was performed after this steady state was achieved. Constant drift had little effect on the response since the satellite assembly was brought up to the constant drift speed during the first few seconds of a run, well before the first step command was executed.

4.2 Test Scope

The baseline tests included a 1° detection maneuver with a nominally configured satellite assembly. Four other 1° configurations were tested, each with a different MOI. Table 4.1 lists the MOI values tested, as well as, the normalized and Additional Moment of Inertia (+MOI) for each configuration.

Table 4.1 MOI Values Tested

MOI ($\text{kg} \cdot \text{m}^2$)	Normalized	+MOI (%)
35.158	1	–
36.363	1.0342	3.42
37.672	1.0715	7.15
39.215	1.1154	11.54
43.250	1.2302	23.02

Next, the test scope was expanded to investigate the effect of the detection maneuver magnitude on the sensing ability of the algorithm. The satellite controller tuning parameters were not changed between detection maneuver magnitudes. The result was no overshoot for 0.5° steps and approximately 20% overshoot for the 2° steps. In other words, as the maneuver magnitude increased, the damping decreased. The test matrix is catalogued in Table 4.2. In all, 165 tests were used in this effort.

Table 4.2 Number of Test Points at Different Detection Maneuver Magnitudes

+MOI (%)	0.5°	1°	2°
–	10	25	10
3.42	10	10	10
7.15	10	10	10
11.54	10	10	10
23.02	10	10	10

4.3 Test Results

The reaction wheel motors were modeled empirically due to lack of access to the built-in motor controller design (See Sections 3.4.2 and 2.2.4). This resulted in a simple motor model, but also a motor model that needed to be tuned for each detection maneuver amplitude. Each magnitude family (column of Table 4.2) was, therefore, tested nominally (zero +MOI) multiple times in order to tune the model using a least squares type minimization. The minimization routine had to be robust enough to handle multiple local minima.

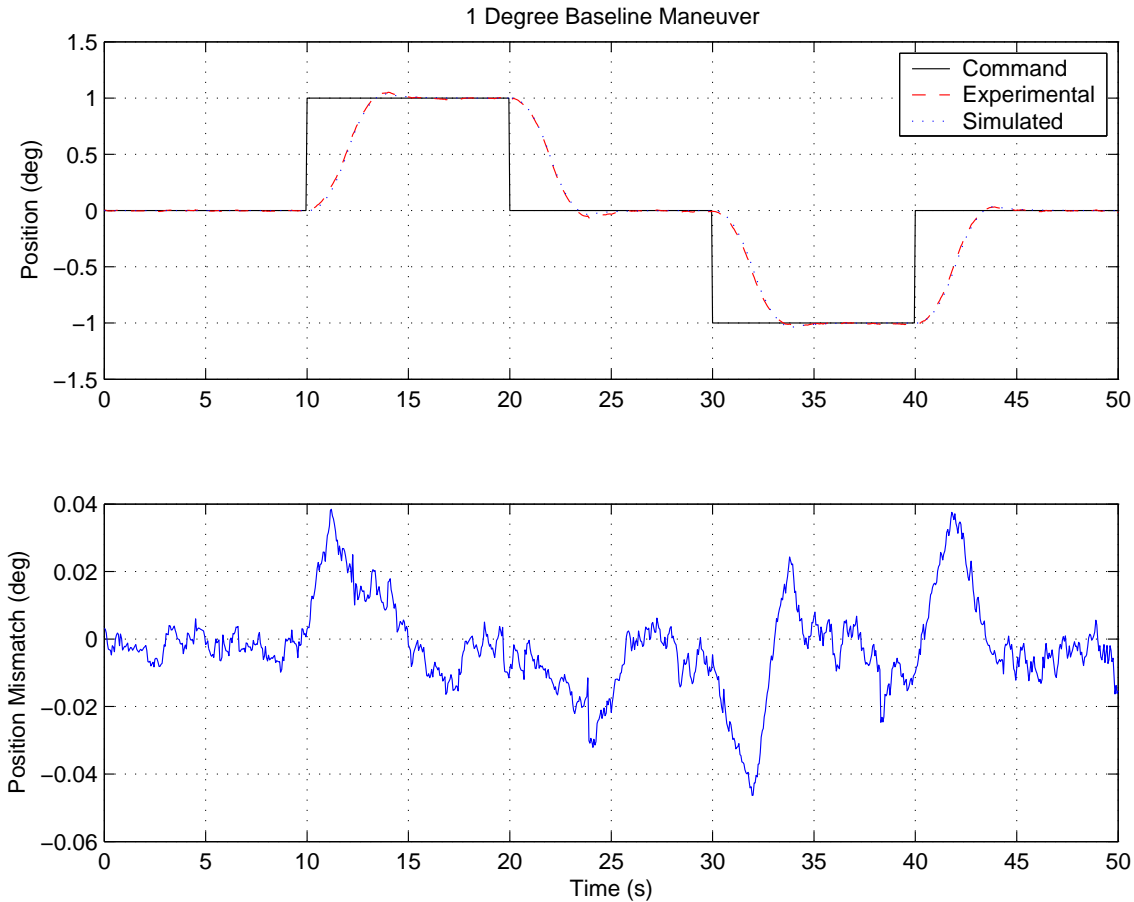


Figure 4.2 Example Data Fit

After the model was tuned, off baseline data was tested. A similar minimization routine was used to estimate the MOI. Figure 4.2 represents a typical data fit. Recall, only steps one and three are used for matching. For this example, this equates to times: $t = 10\text{--}20\text{ s}$ and $t = 30\text{--}40\text{ s}$.

4.3.1 Baseline Results. The baseline MOI values were estimated by first creating the baseline model. This was done by fitting the model to each individual baseline data run. The model parameters were then averaged (arithmetic mean) to arrive at the detection model. Since the model was tuned to this baseline set of data, the normalized distribution has a mean of 1. Due to the nonlinearity of the

model, this process was repeated two more times for the other detection maneuver magnitudes.

Table 4.3 lists the basic statistical analysis of the baseline data for all detection maneuvers. All data that follows was normalized to the nominal satellite characteristics unless otherwise noted (*i.e.* divided by the baseline characteristic). Notice that the range and standard deviation (SD) of the estimated MOI improve with the amplitude of the detection sequence. It is believed that the larger overshoot experienced on the 2° maneuvers allowed for a better data fit and was responsible for the reduction in standard deviation.

Table 4.3 Statistical Analysis of Different Baseline Detection Maneuver Magnitudes

	0.5°	1°	2°
Mean	1.00	1.00	1.00
Range	0.127	0.114	0.0827
SD	0.0416	0.0313	0.0246

The baseline data distributions are illustrated in Figure 4.3. Each bar represents $\pm 0.5\%$ (span of 1%) MOI. Remember that the baseline data for the 1° maneuver contained 25 runs as opposed to 10 runs for the other maneuvers.

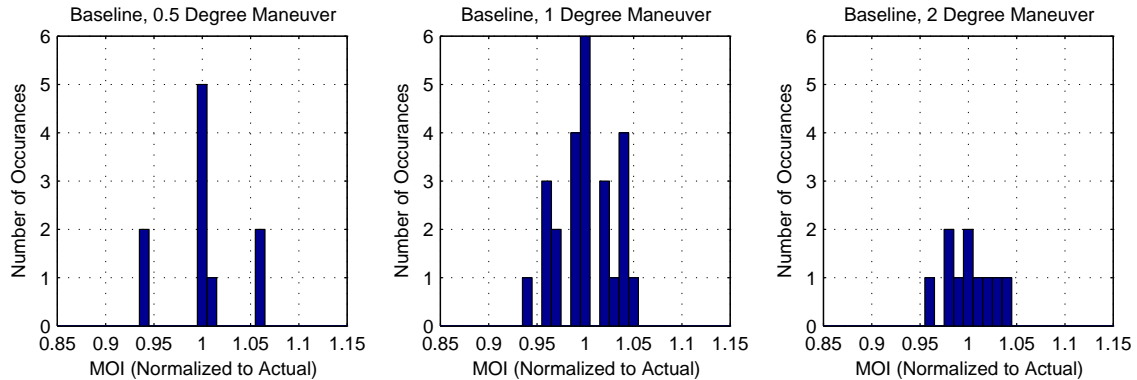


Figure 4.3 Baseline Data Histogram

4.3.2 Estimated MOI Results. The data in this section was estimated by fitting the baseline model to each off-baseline data run by only varying the model MOI. The mean MOI of the 10 trials was estimated to be actual MOI value.

First, a parametric analysis was performed to test the effect of parasite size on the estimated MOI deviation. The estimated MOI for 0.5° , 1° , and 2° tests are compiled into Figures 4.4, 4.5, and 4.6 respectively. Each histogram was normalized to the *actual* MOI value for ease of comparison (*i.e.* a value of 1 is zero error). Again, the same trend of decreased data range for increased maneuver amplitude was observed.

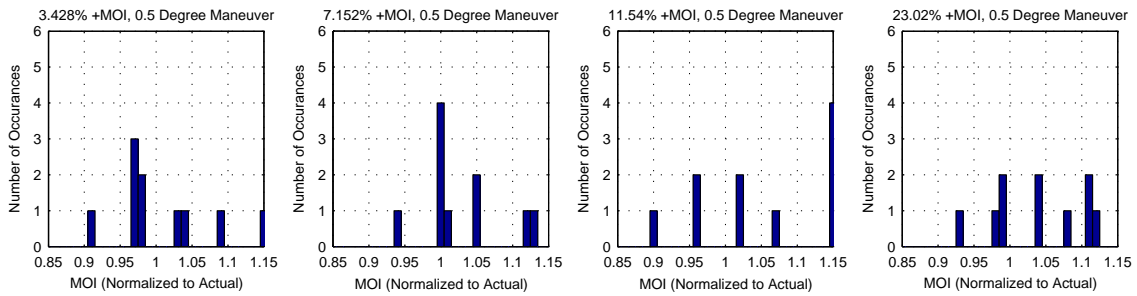


Figure 4.4 Estimated MOI Histogram, 0.5° Maneuver

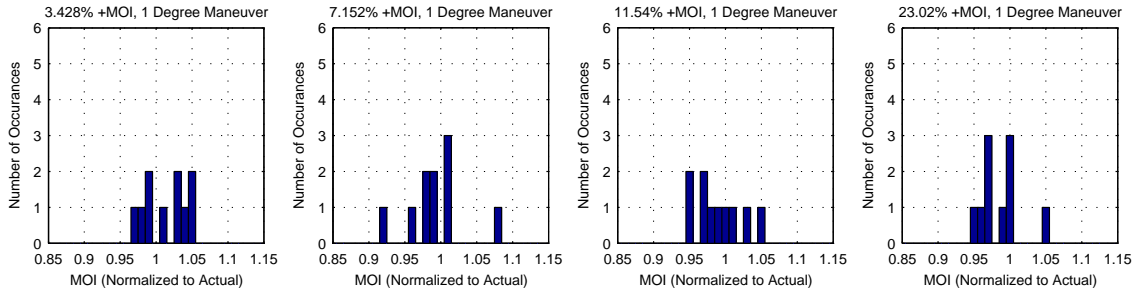


Figure 4.5 Estimated MOI Histogram, 1° Maneuver

Figure 4.7 illustrates some statistical data as a function of MOI. Notice that the seemingly stray data point in Figure 4.6, pane four increases the range and SD of the 2° data at 23% +MOI, but the MOI estimate remains remarkably accurate with a mean MOI estimation accuracy of 0.67% for non-baseline testing. The 1° and 0.5°

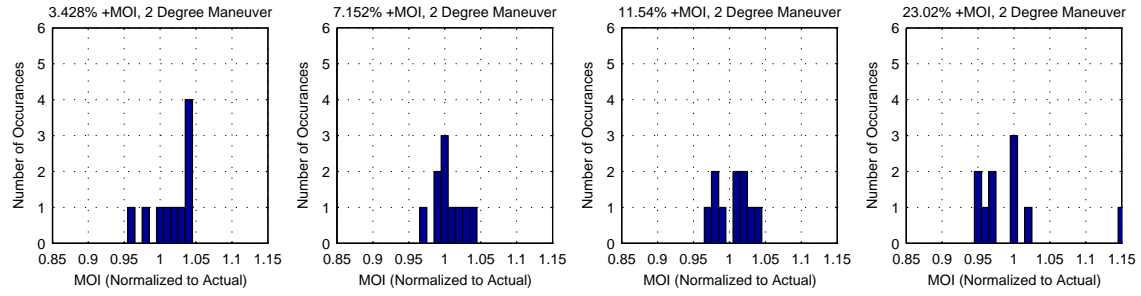


Figure 4.6 Estimated MOI Histogram, 2° Maneuver

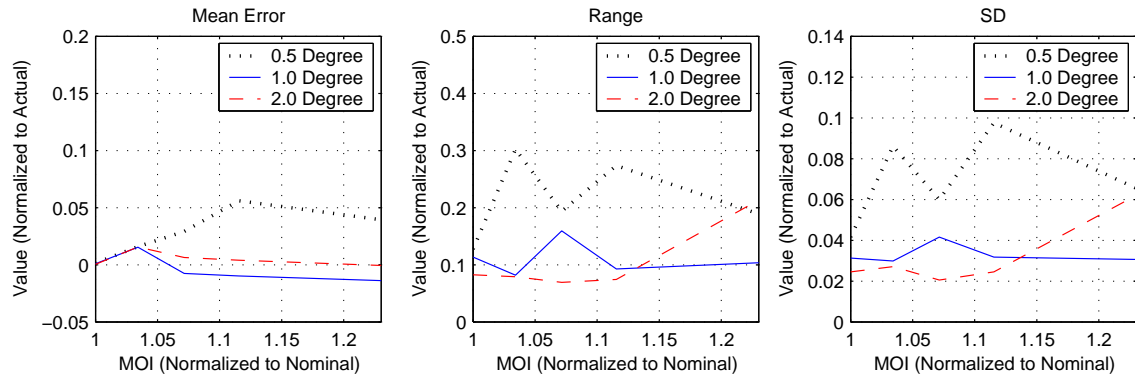


Figure 4.7 Detection Result Statistics

maneuvers only detected to a mean MOI accuracy of 1.2% and 3.5% respectively. With 10 runs, the 1° and 2° groups detected all configurations within $\pm 2\%$. The mean SD of the 1° and 2° maneuvers was nearly identical at 3.4% MOI, while the 0.5° maneuver was nearly double at 7.7% MOI.

Data overlap between sets and MOI estimation accuracy are the critical factors to the operator or detection algorithm. Overlap is related to the SD, while accuracy, in this case, is simply the distance from the mean MOI detected in the data set to the actual value. Figure 4.8 illustrates how a single reading could not determine the actual MOI to more than $\pm 15\%$ in some cases. If the 0.5° maneuver were used and detected a normalized value of 1.05, the actual value could be anywhere from nominal to 11.5% +MOI. Multiple runs had to be performed to “average-out” the noise in the measurements. The question then became: “How could the method

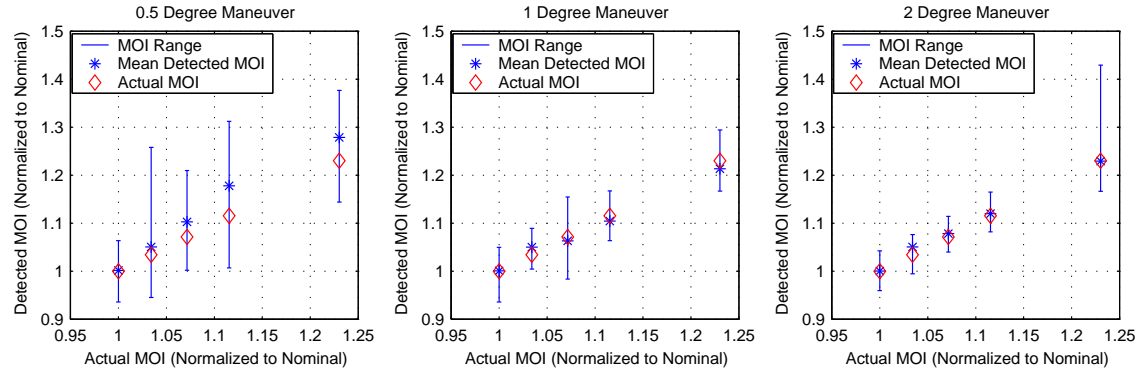


Figure 4.8 Data Overlap and Accuracy

be improved to limit the data overlap and improved the accuracy?" The next two sections look at improving the estimated MOI, from the same data set.

4.3.3 Estimated MOI Results, Method Two. One method of decreasing the data spread was by rejecting data runs (responses to the detection command) on the periphery. It was hypothesized that the data runs least corrupted by noise and other factors, in general, fit the model best. The mean angular mismatch during the match interval was chosen as the metric and defined as the positive difference between the actual response and the modeled response averaged (arithmetic mean) over the matching interval. The model was tuned using only the data runs that were 50 percentile in error. Similarly, the off-baseline data sets were fitted and half of the data runs with the most mismatch were eliminated (*i.e.* "statistical outliers" were ignored). Figure 4.9 shows the statistical trends, while Figure 4.10 shows the relative relationships between the data sets.

The normalized error for method two was larger than method one by an average 41% margin. Both, the mean range and mean SD were generally reduced using method two. The range was on average 30% less than the baseline, while the SD was 11% less. Table 4.4 summarizes the findings.

The decreased range and SD offered by this method is desirable, but the cost in accuracy associated with this method precludes its use. Perhaps a less drastic

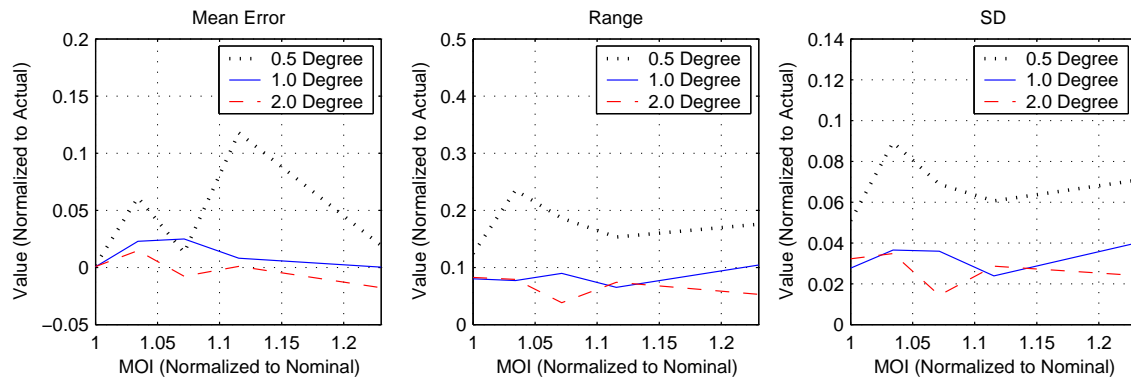


Figure 4.9 Detection Result Statistics, Method Two

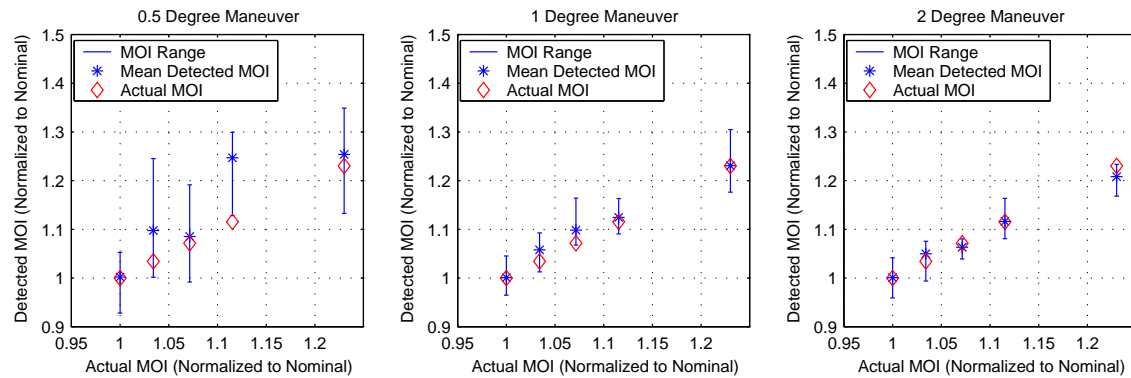


Figure 4.10 Data Overlap and Accuracy, Method Two

Table 4.4 Estimation Method Comparison, Method Two

	Mean Error ($\times 10^3$)		Mean Range ($\times 10^2$)		Mean SD ($\times 10^2$)	
	Method 1	Method 2	Method 1	Method 2	Method 1	Method 2
0.5° Maneuvre	35.18	52.84	23.98	18.78	7.733	7.240
1° Maneuvre	11.60	14.10	10.94	8.424	3.351	3.412
2° Maneuvre	6.703	10.30	10.91	6.127	3.358	2.550

estimation scheme could capture the benefits of this method without the high price paid in accuracy.

4.3.4 Estimated MOI Results, Method Three. A more moderate estimation system was implemented, again using the mean mismatch between actual and modeled responses. This method used a weighted average with weights, W_i 's, defined as:

$$W_i = \frac{1}{E_i} \quad (4.1)$$

where E_i is the angular mismatch normalized to the minimum angular mismatch of the set and i is the number of the run within the data set. The runs with the least mismatch became more important than those with a higher mismatch level. The weighting process was used both to tune the model and to detect the +MOI. Figures 4.11 and 4.12 were the result.

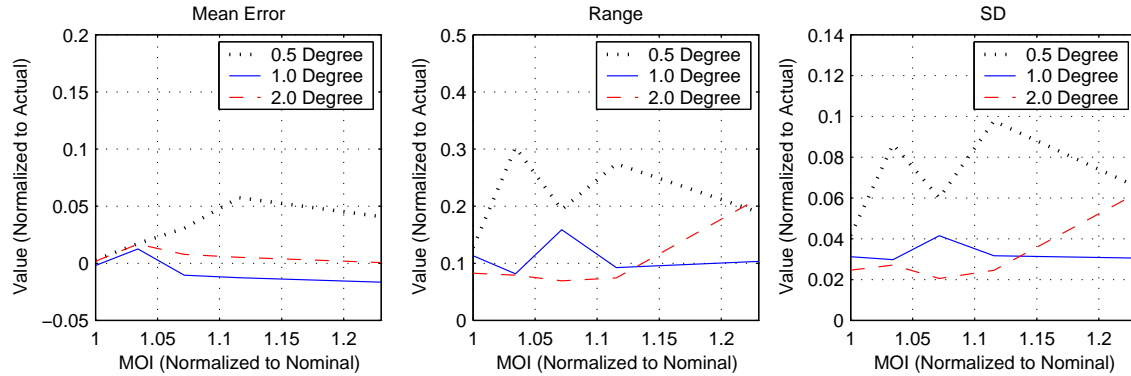


Figure 4.11 Detection Result Statistics, Method Three

Table 4.5 Estimation Method Comparison, Method Three

	Mean Error ($\times 10^3$)		Mean Range ($\times 10$)		Mean SD ($\times 10^2$)	
	Method 1	Method 3	Method 1	Method 3	Method 1	Method 3
0.5° Maneuver	35.18	36.53	2.398	2.401	7.733	7.743
1° Maneuver	11.60	13.12	1.094	1.091	3.351	3.341
2° Maneuver	6.703	7.686	1.091	1.093	3.358	3.362

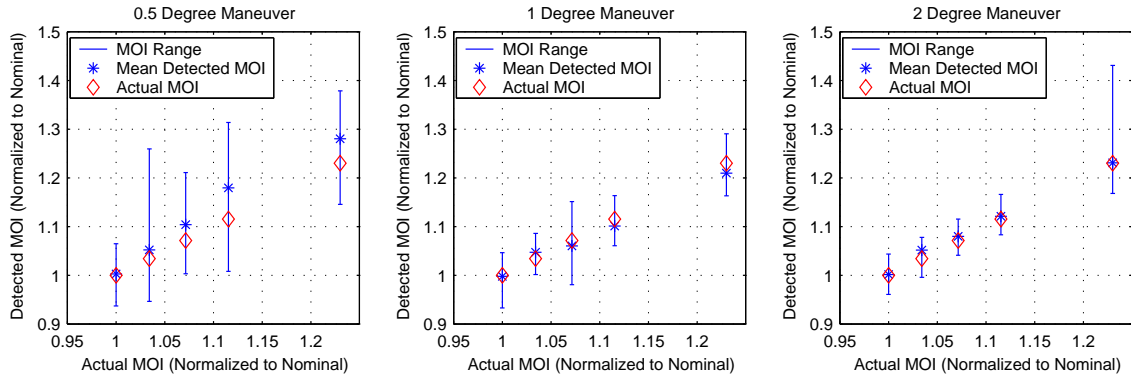


Figure 4.12 Data Overlap and Accuracy, Method Three

Method three increased the normalized error over method one in every case by an average of 10%. The change in range and SD was minimal with average increases less than 0.2%. Table 4.5 summarizes the results.

4.3.5 Repeatability. It was believed that some of the variability from run to run, given the same command input, could be traced back to the reaction wheel motors. A test was performed to test this theory. The motor tuning parameters were changed from a balance between performance and repeatability to a lower performance, higher repeatability state by changing the acceleration parameter from 9.92 m/s^2 (motor controller tuning parameter, $A=25$) to 5.16 m/s^2 ($A=13$). The result confirmed the theory (Table 4.6 and Figure 4.13) that increased repeatability leads to decreased data spread. The range and SD were reduced by 21% and 13% respectively. This result allows us to conclude that higher fidelity reaction wheels (typical space hardware) would result in much less variation in the data yielding more reliable estimates of the MOI. Fewer maneuvers would be required to get the same quality estimate or the same number of maneuvers would result in a better estimate.

Table 4.6 Results of Repeatability Investigation

	Mean Range ($\times 10^2$)	Mean SD ($\times 10^2$)
Baseline Performance	8.266	2.462
Low Performance	6.546	2.147

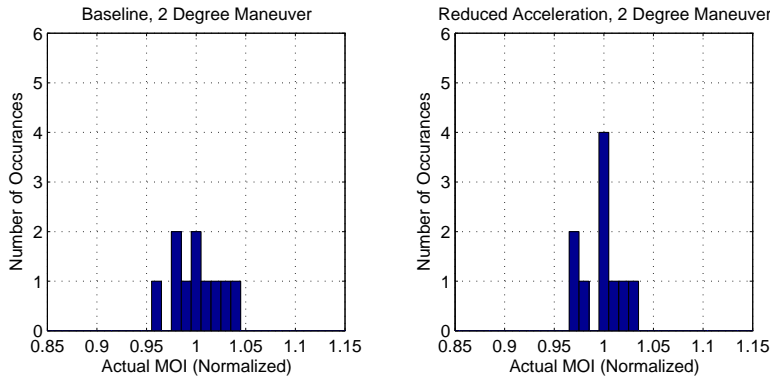


Figure 4.13 Repeatability Comparison, 2° Maneuver

4.4 Application of Results

Having successfully demonstrated the detection algorithm in the lab, the findings of this thesis, as presented above, were applied to operational systems. The GPS-IIR satellite and HST were considered.

4.4.1 Method. The analysis begins by defining the change in MOI:

$$\Delta \mathbf{I} = \mathbf{I}_{new} - \mathbf{I} \quad (4.2)$$

where $\Delta \mathbf{I}$ is the change in MOI due to the docked microsat (+MOI). Assume the system center of mass remains unchanged (the mass of the parasite is small relative to the satellite). For simplicity, adapt Equation 2.11 to a discrete distribution of mass in a single axis:

$$\Delta I_{ii} = \Delta m(\rho_{i+1}^2 + \rho_{i+2}^2) \quad (4.3)$$

where i is the axis number evaluated modulo three and Δm is the change in system mass—the change in MOI was caused by a change in mass, m , at a position, ρ . Solving for Δm or the mass of the parasite:

$$m_{parasite} = \frac{\Delta I_{ii}}{\rho_{i+1}^2 + \rho_{i+2}^2} \quad (4.4)$$

where i is again the axis number evaluated modulo three.

4.4.2 Applied Results. The approximate mass properties of the GPS satellite [23] (aligned with the body axes defined in Figure 2.2) are:

$$\mathbf{I} = \begin{bmatrix} 1725 & 0 & 0 \\ 0 & 782 & 0 \\ 0 & 0 & 2020 \end{bmatrix} \text{ kg} \cdot \text{m}^2 \quad (4.5)$$

Using the best detection algorithm as derived in this paper (Method I, 2° maneuver, 0.67% mean accuracy), the detectable MOI limits become:

$$\Delta \mathbf{I} = \mathbf{I} \cdot 0.0067 = \begin{bmatrix} 11.56 & 0 & 0 \\ 0 & 5.239 & 0 \\ 0 & 0 & 13.53 \end{bmatrix} \text{ kg} \cdot \text{m}^2 \quad (4.6)$$

The GPS bus is a 1.6 m cube with its center of mass centrally located. Assume the parasite is docked on the satellite exterior centered on the b_1 axis. To be conservative, define the parasite center of mass to also be located on the satellite exterior (not offset some distance). The position of the additional mass relative to the system center of mass is then:

$$\rho = \begin{bmatrix} .8 \\ 0 \\ 0 \end{bmatrix} \quad (4.7)$$

Applying Equation 4.4 to find the minimum mass detectable at this location, results in a minimum detectability of 8.2 kg. This is the worst case scenario for this satellite configuration. A similar investigation into the HST [25] provides a detectable limit of 52 kg. Figure 4.14 is a depiction of the HST. As expected, the least detectable locations are the circle of points on the cylindrical satellite bus passing through the solar panel attachment points.

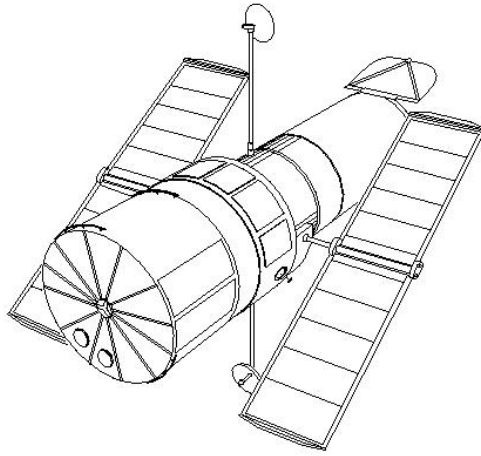


Figure 4.14 Hubble Space Telescope

Attack on a GPS satellite would appear to be detectable assuming a parasite mass on the order of 40 kg. On-orbit results would have to be better than observed on the ground-based simulator in order to detect HST parasites. This improvement is expected, but the size of any improvement is unclear. An estimate of the utility of this method on specific satellites is possible by examining characteristics at the system level.

4.5 System-Level Characteristics

If second order response characteristics are applied to the satellite at various MOI configurations, insight into the top-level requirements for this type of detection algorithm can be determined.

Figure 4.15 tracks overshoot, rise time, and settling time as a function of MOI for the 2° maneuver. Note that the time characteristics (rise time and settling time) are quantized to the timestep used in the simulation, 0.05 seconds, yet the trend is clear. It is shown that overshoot is the most sensitive to these types of changes, whereas rise time is rather insensitive. Using this chart, one can determine the repeatability required in order to detect a parasite of a given size. For example, if it is known that for a series of identical maneuvers the overshoot of particular satellite varied $\pm 5\%$, one can expect this method to be able to detect 4.1% changes in MOI.

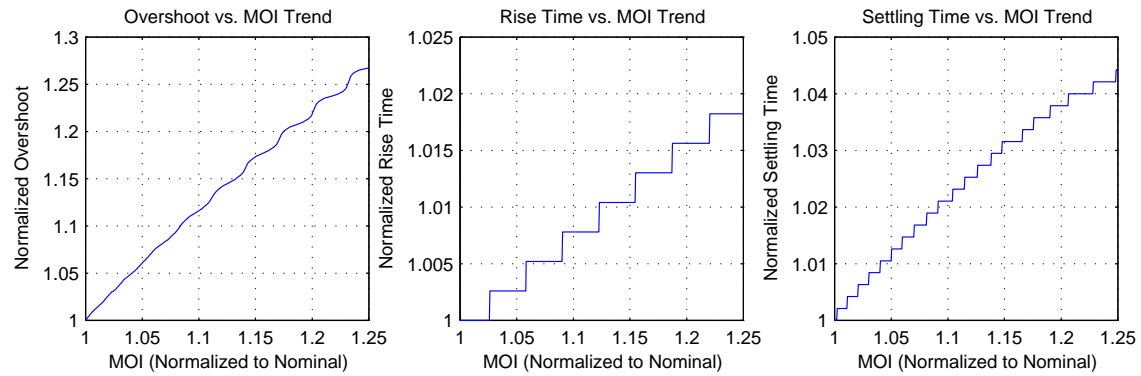


Figure 4.15 Second Order Characteristics as a Function of MOI

4.6 Summary

The test procedure and scope were described followed by the baseline test results. It was discovered that the larger amplitude maneuvers with greater overshoot led to more repeatable measurements in the baseline data. This in turn led to more repeatable and accurate results for most test cases. The equally weighted mean of all the individual measurements was found to best estimate the parasite-induced \pm MOI. It was found that repeatable reaction wheel motion is an important factor in the quality of the estimate achieved. The most accurate method was applied to operational systems to better understand the utility of the system. The results were promising. Finally, system-level properties were investigated so that one might be able to predict how well this system may operate on a specific platform with a given

repeatability of motion. Chapter V presents the conclusions drawn from this work and recommendations for the future.

V. Conclusions and Recommendations

The US is currently blind to attack by microsats. If this is to change, action must be taken to increase the situational awareness of satellites. Detection methods, like the technique outlined in this thesis, can be used immediately to drastically increase the degree of US readiness. Further research would be beneficial to refine the method and adapt the system for operational deployment.

5.1 Conclusions

The detectability of “parasitic” satellite attack was investigated. Cited research deemed ground-based methods inadequate using current equipment. It has been suggested that the impact of a soft-dock would be detectable by operators. Docking and collision models were constructed to test response differences. Detecting the docking event itself proved to be indistinguishable from routine space debris collisions. Angular differences from zero to the order of 10^{-5} arcsec were calculated for a relatively high fidelity docking maneuver compared to a debris collision of the same magnitude.

A dynamic detection technique was then devised and validated on a ground-based satellite simulator. The baseline methodology required the creation of a satellite model and detection maneuver. Next, the satellite’s response to the detection command was recorded. Model parameters were changed to fit the model response to the satellite response. By fitting the model to future satellite responses, changes in MOI could be sensed. This was based on the assumption that the only model parameter changed to get a best fit during these operational runs was the satellite MOI.

Parasite-induced MOI changes of 3–23% MOI were investigated. Detection maneuver amplitudes of 0.5° , 1° , and 2° were tested on a system optimized for 1° motion. The mean of multiple trials were required for positive ID of a parasite and

estimation of its size. The 2° maneuver yielded the best results with a mean SD of 3.4% MOI and mean error of 0.67% MOI with 10 trials per configuration. Estimated MOI values were normalized to the actual satellite properties. All detection command sets did successfully sense the additional parasite mass.

Other estimation schemes were explored utilizing the average angular mismatch between the actual response and the modeled response as a weighting factor between runs in a set. Culling data based on this metric, generally reduced the range and SD of data, but did not improve the accuracy overall. Using a weighted average to come to a final MOI estimate based on this metric was also tested. The weight was chosen to be the reciprocal of the mean angular mismatch. The results were similar to the baseline case, but were generally unimproved by any measure.

The results suggest that even smaller changes in MOI can be detected. Detection of MOI changes on the order of 1% would not be unreasonable on the current test apparatus. The detectability limitations depend on the number of trials performed and the repeatability of the satellite response. Better results are expected on-orbit, as the lab results were limited by the fidelity of SIMSAT system. Military satellites generally employ the use of high-quality space-qualified hardware.

5.2 Recommendations

The work presented in this thesis can be immediately incorporated into a detection package. Follow-on work in this field would ease the transition to operational detection and expand the applicability of the findings.

5.2.1 Future Work. Additional research in this field will allow an even higher-quality detection scheme to be easily incorporated into current satellite operations. Possible areas of further exploration include the following.

- A more robust estimation scheme could be incorporated to decrease computation time and automate detection. A layered approach might be incorpo-

rated using a batch filter for estimating MOI from individual maneuvers and a sequential filter for maneuver-to-maneuver MOI estimation. This task is nontrivial due to the nonlinearities (saturations, delays, look-up tables) in the model.

- Combined axis testing could be implemented to reduce the number of motions required to sense change.
- The same command sequence given multiple times to SIMSAT resulted in a range of responses. This variation in time histories led to the “spread” of detected MOI values. Investigation into the non-repeatable nature of the experiments performed in this thesis could help predict how closely the results presented here might correspond to on-orbit operation.
- Further investigation and testing of the motors could lead to an improved model of the motor controller creating a more robust model of SIMSAT.
- The results presented here only considered a rigid body. Many satellites have appendages (antennas, solar arrays, etc.). Flexible structures could be incorporated on SIMSAT to simulate these effects. It is unclear if the modal testing of such satellites will increase or decrease the detection sensitivity.
- The detection maneuver could be tailored to specific satellite operations and stationkeeping maneuvers for a transparent deployment of the system.

5.2.2 Current Results. The research provide herein verifies that parasite satellites can be detected today. Only simple models and readily available data are required to drastically increase our SSA. Old telemetry data can be used for model creation and tuning. Current routine maintenance maneuvers may be able to be used for detection purposes.

The most likely method of installation of this detection algorithm is as part of a “smart” system where artificial intelligence is used to monitor satellite health and environment. The “brain” of this kind of system requires tools and rules to

operate. This detection scheme is readily integrated into a complete SSA system such as RAIDRS. The deployment of such a system could be designed to have no impact on current operations, but provide fundamental knowledge of the systems readiness for war.

Appendix A. LN-200 Fiber Optic Gyroscope Upgrade

A high-quality gyroscope would greatly increase the usability of the SIMSAT system. The current gyroscope needs constant attention to achieve good performance. The measurements are highly temperature sensitive and noisy. It must be run for approximately 30 minutes prior to testing to achieve steady-state performance. Even at this point, short and long period noise are present. The noise in the roll and yaw axes has an amplitude on the order of 0.1° while in pitch this noise is amplified approximately five-fold. For experiments lasting on the order of minutes, this long period noise presents problems. Without regular software recalibration, the drift in the pitch can soon reach extreme levels. It is not uncommon to start the SIMSAT system at 0° in pitch and find that after five minutes of closed-loop operation holding this “position”, the system is in contact with the pedestal (*i.e.* $>25^\circ$ drift). A better system is desired.

A Litton® (now Northrop Grumman® Navigation Systems) model LN-200 Fiber Optic Gyroscope (FOG) was purchased for this purpose. Figure A.1 illustrates the LN-200 FOG. It is a space-qualified FOG with up to $1^\circ/\text{hr}$ accuracy. This is expected to be a two order of magnitude improvement. It is approximately the same size as the current gyroscope for simple physical integration. Table A.1 presents the relevant instrument characteristics.

The data communications integration proved to be difficult. The author spent considerable time (months) attempting to integrate this hardware into the SIMSAT system. The fundamental problem is the conversion of the SDLC data stream to an asynchronous data structure for capture by a standard asynchronous RS-485 port. The synchronous SDLC data stream uses a flag/framing structure and therefore has no “start” or “stop” bits allowing the data to remain relatively unaltered within the frame as opposed to an asynchronous structure where the data is usually chopped



Figure A.1 LN-200 Fiber Optic Gyroscope

into 8-bit “chunks”. Attempting to receive this synchronous framed data on an asynchronous platform results in data loss where the “start” and “stop” are stripped.

Additionally, this conversion is required to be accomplished onboard the satellite assembly and must use only direct current (DC). The onboard computer is a proprietary design and standard computer cards will not interface with it correctly although company representatives mentioned it may be able to provide DC power to a non-compatible board. The author unsuccessfully searched for a COTS solution

Table A.1 Northrop Grumman[®] LN-200 Characteristics

Parameter	Value
Weight	700 g
Diameter	8.9 cm
Height	8.5 cm
Power Consumption	10 W
Bias Repeatability	1–10°/hr
Random Walk	0.04–0.1° hr ^{1/2} power spectral density
Data Latency	<1 msec
Data Protocol	RS-485
Data Structure	Synchronous Data Link Control (SDLC)

and/or COTS hardware that could be integrated into a workable solution. A custom piece of hardware is expected to be implemented as funds allow.

Appendix B. Reaction Wheel Motor Tuning

The motors used in the reaction wheel assembly are not designed for this purpose. They are manufacturing motors most often used for assembly line operation/automation. Some of the difficulties encountered as a result of this mismatch follow.

- The motors are optimized for the use of position commands, not velocity commands. Some of the controller parameters do not translate well into velocity operations, for example the mandatory position error limit.
- The motors are capable of accepting velocity mode commands, but have no tachometer to measure velocity. A finite difference routine is needed to calculate velocity.
- The large flywheels and lack of friction cause the motors to be regularly operated outside of the envelope for which they were designed.
- The proprietary nature of the controller restricts access to its design. This makes designing a program to optimize the tuning parameters very difficult. The unorthodox use of the motors makes the manufacturer's tuning documentation/experience of little use.

The author spent two weeks tuning the motors for maximum performance over a broad range of commands for general SIMSAT usage. Large commands require large amperage. Even smaller commands have a large transient peak power requirement that altered the response between the bench power supply and the onboard batteries. The largest power supply available to the author, trips its breaker at approximately 20 Amps, requiring most tests to be done from battery power. Unfortunately, the batteries were deteriorated and only lasted for approximately 10 maximum performance tests before requiring to be recharged for six to eight hours. New batteries were ordered, received, and installed to continue testing. In all, over 200

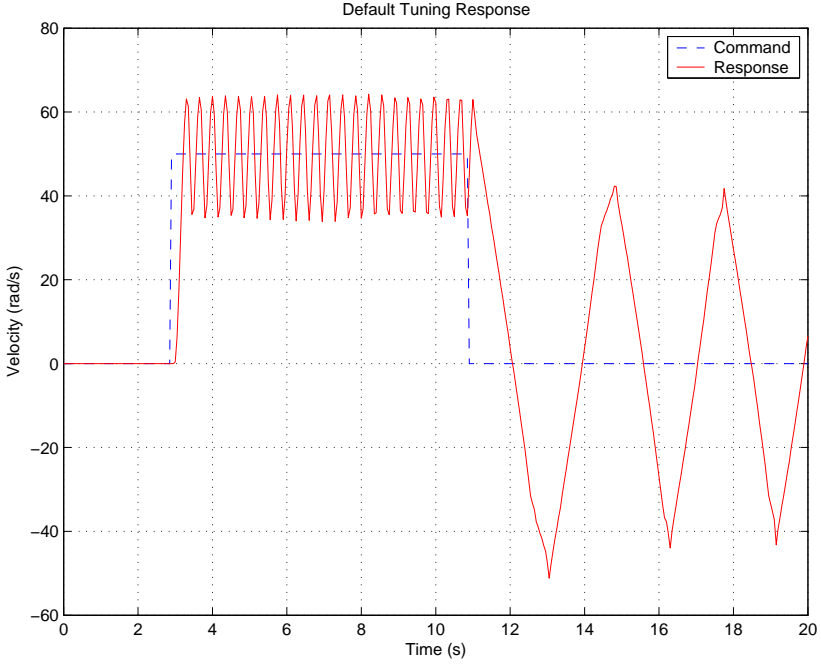


Figure B.1 Default Tuning Response

tests were performed to find a suitable set of tuning parameters. Figure B.1 shows the response of the factory-set default tuning values to a 50 rad/s square pulse at an acceleration of approximately 200 rad/s² (acceleration parameter of 500). This value is approximately ten times larger than the maximum found in the test protocol, but 10 times less than the maximum range. Notice the high frequency oscillation due to poor tuning and the lower frequency limit cycle due to exceeding the maximum position error value which turns the motor off momentarily only to restart and repeat the cycle.

Figure B.2 is an intermediate stage of tuning (all values as in the final configuration with the exception of KP=15, KD=2500, and A=500), so larger commands are possible. Notice the excellent acceleration performance to -50 rad/s followed by a “kink” in the response as the next step begins and again as it crosses from deceleration to acceleration. During the final change in command, the motor once

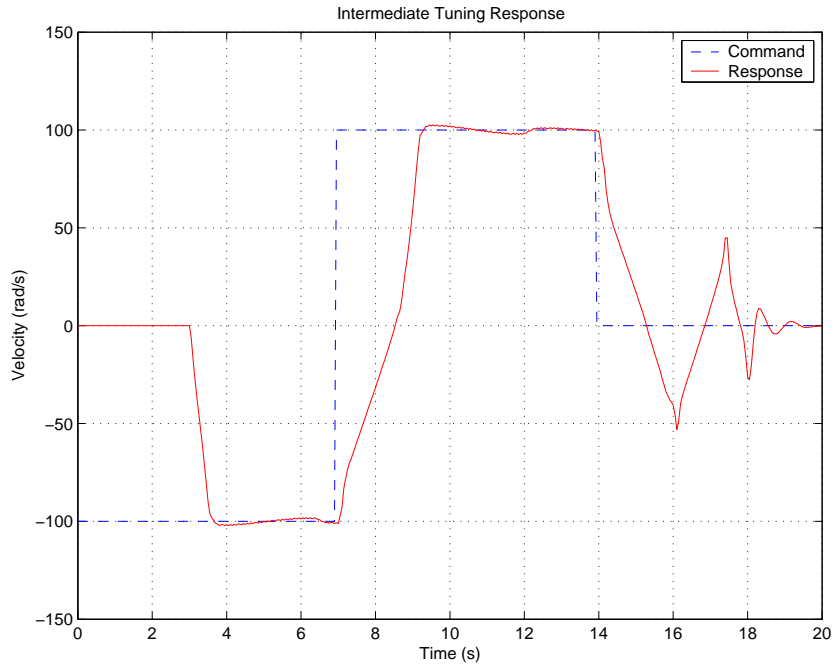


Figure B.2 Intermediate Tuning Response

again enters an error limit-driven limit cycle. This one is less severe and therefore recoverable.

The final testing configuration was used to make the response in Figure B.3. Notice the smaller slope (lower performance) accepted in return for a clean repeatable acceleration. Notice also the drastic difference between acceleration and deceleration. Fortunately, this distinction is less apparent for the smaller changes in velocity used by the test protocol, but provided here to clearly illustrate the phenomenon.

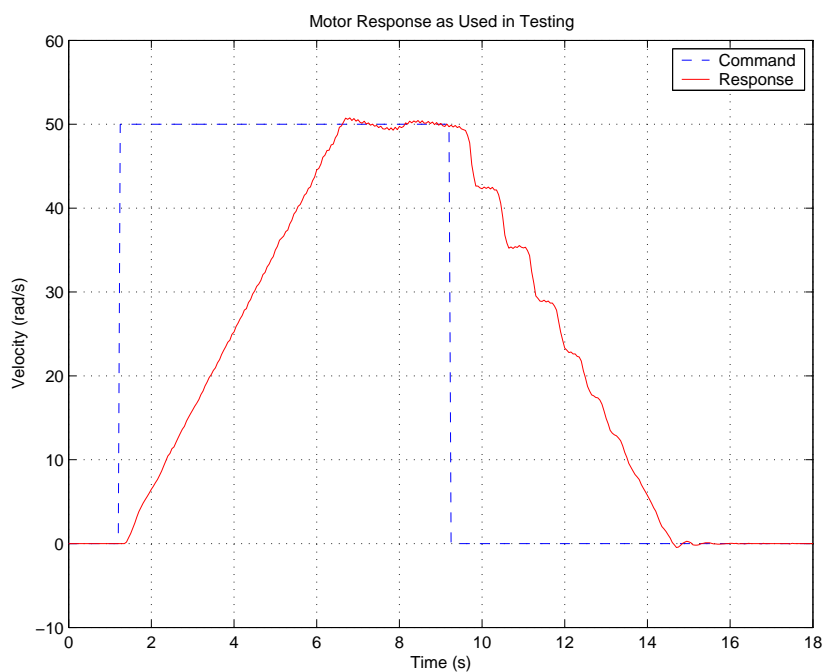


Figure B.3 Final Tuning Response

Appendix C. Minimization Program Code

The following MATLAB® script file was used to find the best fit between the actual and modeled data. The program sequence is as follows:

1. Load the data set to be considered (one file at a time)
2. Load the simulation options
3. For each data run
 - (a) Test 20 MOI points between 50%–200% Baseline MOI
 - (b) Choose the point with the minimum cost
 - (c) Cut the MOI range in half centered on the minimum cost
 - (d) Repeat from (a) until the MOI step is $< 1 \cdot 10^{-6}$
4. Plot the resulting data fit

```
%%%%%%%%
% Program find_I33_best
% Minimizes the mismatch between a Simulink
% Model and actual SIMSAT data
%
% Capt Vincent Dabrowski, 2003
%%%%%%%
global I11 I22 I33 Iw ex ey
format long; clear;clc

%CHOOSE FILESET
disp('set#1: BL')
files=['a32 a34 a35 a36 a37 a38 a39 a40 a41 a43 a44 a45 a46 a48...
        a49 a50 a51 a52 a54 a55 a56 a57 a58 a59 a61'];
%disp('set#2: BL half')
%files=['a63 a64 a65 a66 a68 a69 a70 a71 a72 a73'];
```

```

%disp('set#3: BL two')
%files=['a74 a76 a77 a78 a79 a80 a81 a82 a83 a84'];
%disp('set#4: 10kg, 1 deg')
%files=['a86 a87 a88 a89 a90 a91 a93 a95 a96 a97'];
%disp('set#5: 10kg, .5 deg')
%files=['a98 a99 a100 a103 a104 a105 a106 a107 a108 a109'];
%disp('set#6: 10kg, 2 deg')
%files=['a110 a111 a112 a114 a115 a116 a117 a118 a119 a120'];
%disp('set#7: 4kg, 1 deg')
%files=['a122 a124 a125 a126 a127 a128 a129 a130 a132 a133'];
%disp('set#8: 4kg, .5 deg')
%files=['a134 a135 a136 a137 a138 a139 a142 a143 a144 a145'];
%disp('set#9: 4kg, 2 deg')
%files=['a146 a147 a148 a149 a150 a151 a153 a154 a155 a157'];
%disp('set#10: 2kg, 1 deg')
%files=['a158 a159 a161 a162 a163 a164 a166 a167 a168 a169'];
%disp('set#11: 2kg, .5 deg')
%files=['a170 a171 a172 a174 a175 a176 a177 a179 a180 a181'];
%disp('set#12: 2kg, 2 deg')
%files=['a182 a183 a184 a185 a186 a188 a189 a191 a192 a193'];
%disp('set#13: 1kg, 1 deg')
%files=['a194 a195 a196 a197 a198 a200 a202 a203 a204 a205'];
%disp('set#14: 1kg, .5 deg')
%files=['a207 a208 a209 a210 a211 a212 a213 a214 a215 a216'];
%disp('set#15: 1kg, 2 deg')
%files=['a218 a219 a220 a221 a222 a225 a226 a227 a228 a229'];
%disp('set#16: 0kg, 2 deg, A=13')
%files=['a231 a233 a234 a235 a236 a237 a238 a239 a240 a241'];

model='simsat_sim'

%CHOOSE SIM OPTIONS
command=1 %1 deg
simlength=55

```

```

start_t1=15/.05+1;
stop_t1=25/.05+1;
start_t2=35/.05+1;
stop_t2=45/.05+1;

% command=2 %0.5 deg
% simlength=55
% start_t1=15/.05+1;
% stop_t1=25/.05+1;
% start_t2=35/.05+1;
% stop_t2=45/.05+1;

%command=3 %2 deg
%simlength=75
%start_t1=15/.05+1;
%stop_t1=30/.05+1;
%start_t2=45/.05+1;
%stop_t2=60/.05+1;

%command=4 %2 deg A=13;
%simlength=95
%start_t1=15/.05+1;
%stop_t1=35/.05+1;
%start_t2=55/.05+1;
%stop_t2=75/.05+1;

steps=simlength/.05+1;
num_data_pts=stop_t1-start_t1+stop_t2-start_t2;

% SIMSAT MOIs
%BL set
I11=3.647546812465531e+000;
I22=3.677811796985044e+001;
%I33=3.515802468071735e+001;

```

```

%~10kg
I33=4.324981053845178e+001
%~4kg
%I33=3.921527184484653e+001
%~2kg
%I33=3.767249505661412e+001
%~1kg
%I33=3.636324072038076e+001

% Wheel MOI
Iw=1.955099417802845e-002;

%WHEEL GAIN
WG=0.89569311523437; %Set 1
%WG=1.00108245849609; %Set 2
%WG=0.92266143798828; %Set 3

%Determine # of Files
delimiters=find(files==' ');
num_files=length(delimiters)+1;

for ii=1:num_files
    [token,rem] = strtok(files);
    filename=[token,'.mat']
    load(filename)
    files=rem;

    start= .50*I33;
    finish=2.00*I33;
    step=(finish-start)/20;
    J_min=1e10;
    change=1e10;

    while step>1e-6

```

```

for I33=[start:step:finish]
    [tout,x,y] = sim('simsat_sim',simlength,[],...
    [[0:.05:simlength]',command*ones(steps,1),WG*ones(steps,1)]);
    J=sum(abs(data(start_t1:stop_t1,3)-sy(start_t1:stop_t1,1)))+...
        sum(abs(data(start_t2:stop_t2,3)-sy(start_t2:stop_t2,1)));
%
    figure(1)
%
    plot(I33,J)
%
    hold on
%
    if J<J_min
        J_min=J;
        I33_best=I33;
    end
%
    start=I33_best-2.5*step;
    finish=I33_best+2.5*step;
    step=(finish-start)/20;
end
error_mean=J_min/num_data_pts
load I33_best
% Save best fit & Mean Error
save_error_mean_1(ii)=error_mean;
save_I33_best_1(ii)=I33_best;
save('I33_best.mat','save*')
[tout,x,y] = sim('simsat_sim',simlength,[],...
[[0:.05:simlength]',command*ones(steps,1),WG*ones(steps,1)]);

figure(2)
clf
plot(data(:,1),data(:,2),data(:,1),data(:,3),tout,sc(:,1),tout,sy(:,1))
legend('ec','ey','sc','sy')
xlabel('Time (s)')
ylabel(['Velocity (rad/s), Mean Error: ',num2str(error_mean,'%6E'),' rad/s'])
grid
end

```

Appendix D. Simulation Model Library

The following figures illustrate the mathematical model of the satellite. Its response was used as part of the minimization program (Appendix C) to estimate the MOI of the actual hardware. The programming language is Simulink®.

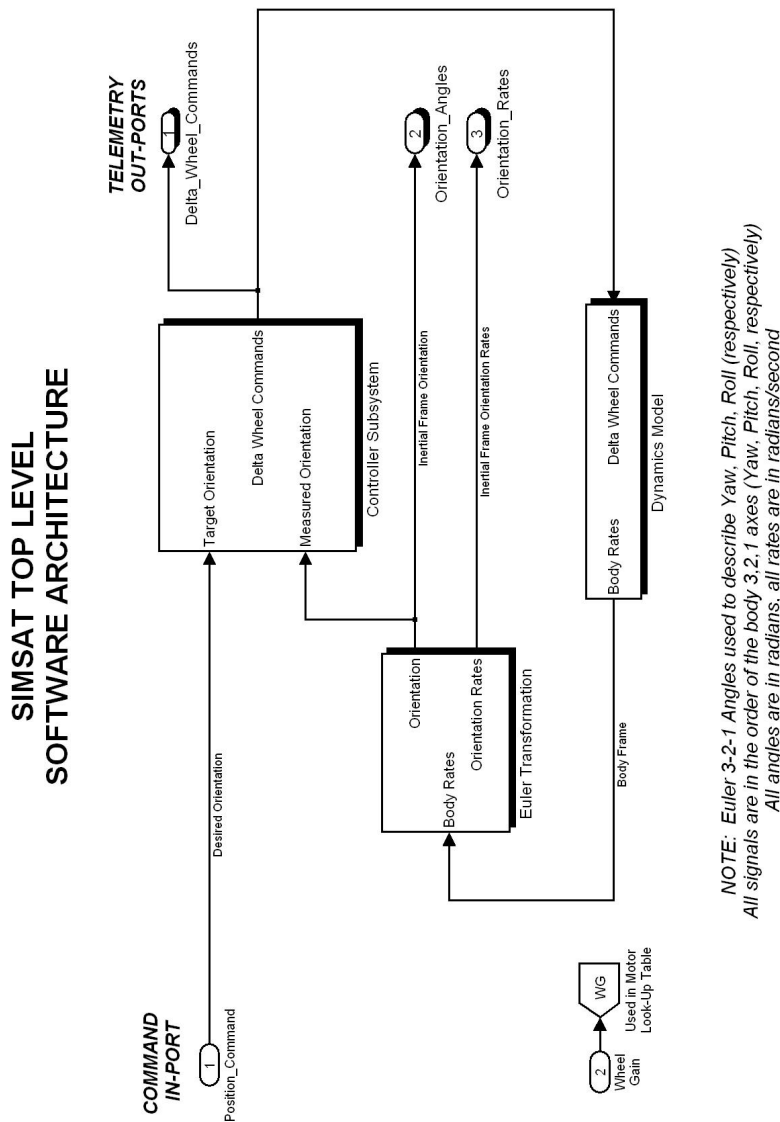


Figure D.1 Top Level Simulation Model

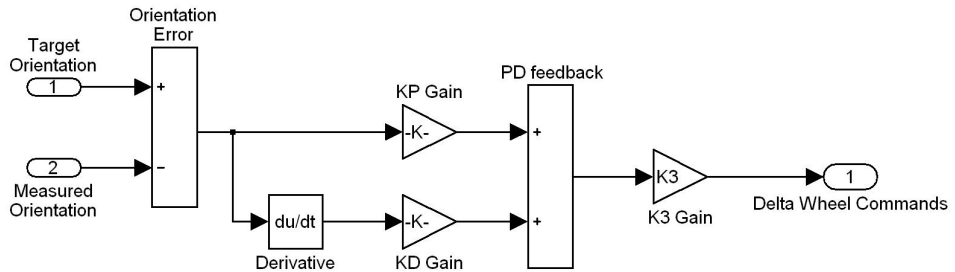


Figure D.2 Proportional Plus Derivative Controller, Level 2 Submodel

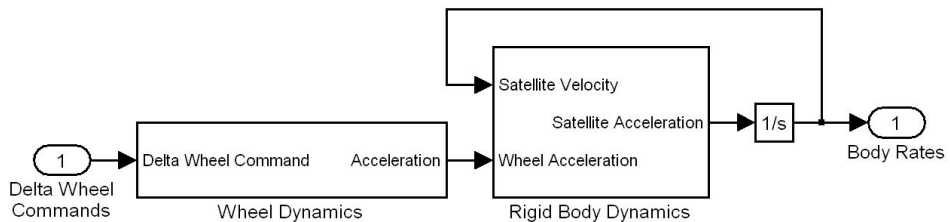


Figure D.3 Dynamics Model, Level 2 Submodel

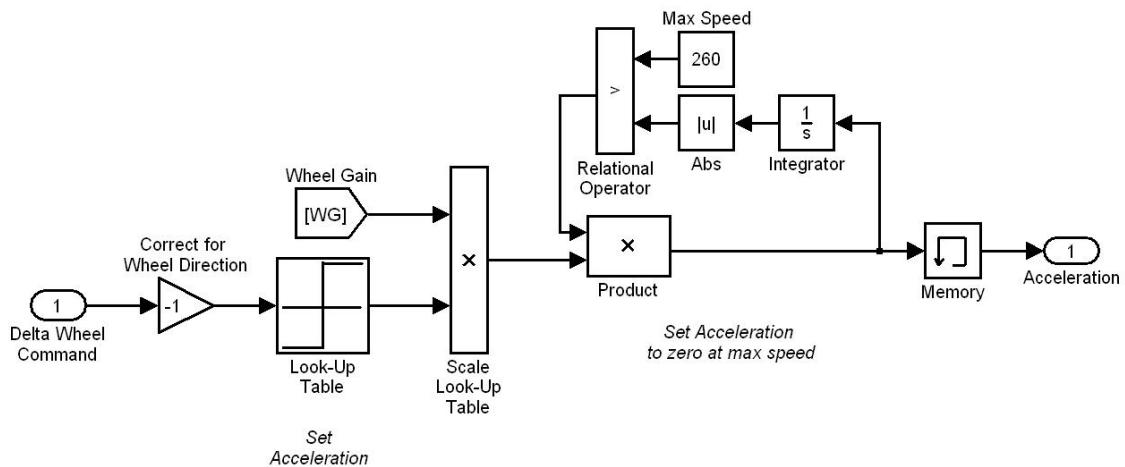


Figure D.4 Wheel Dynamics, Level 3 Submodel

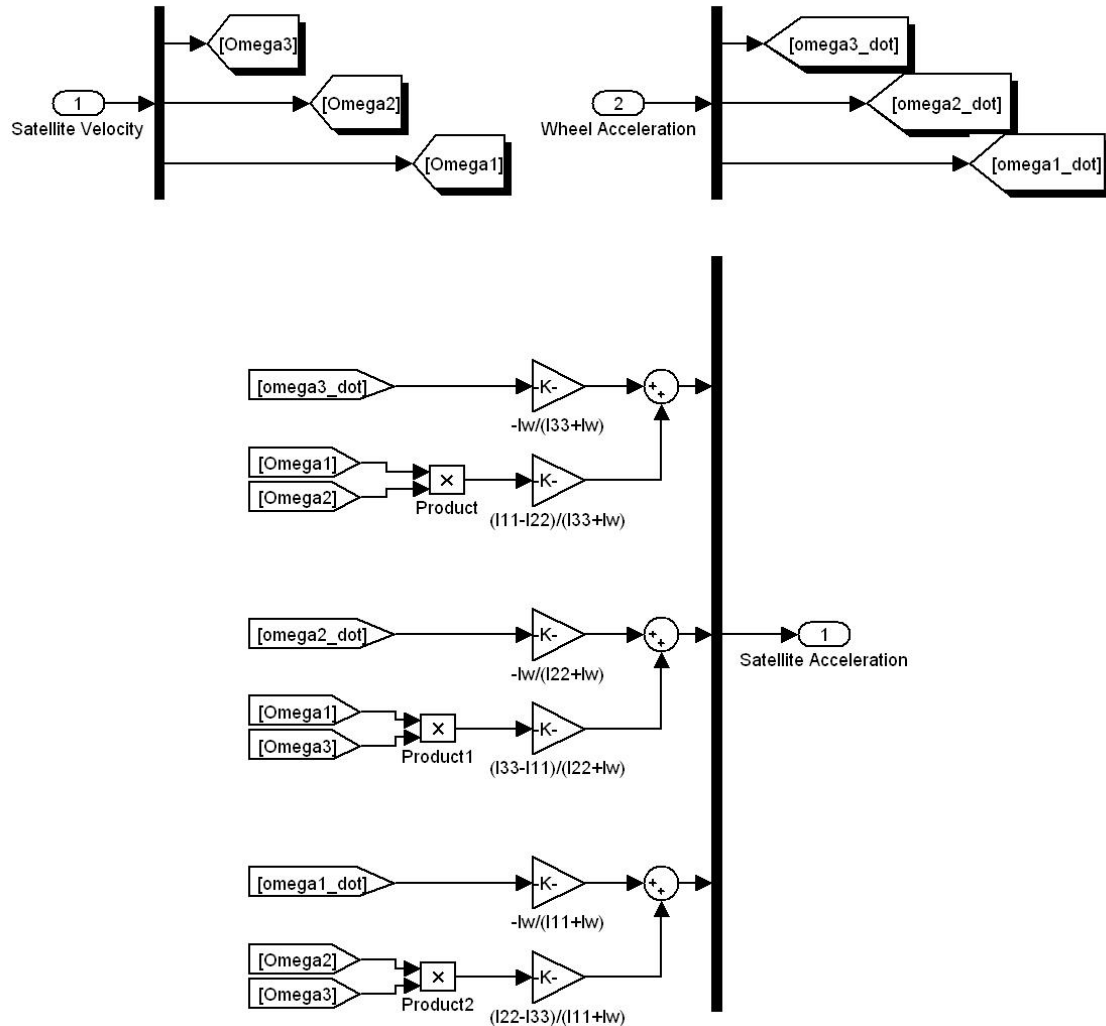


Figure D.5 Rigid Body Dynamics, Level 3 Submodel

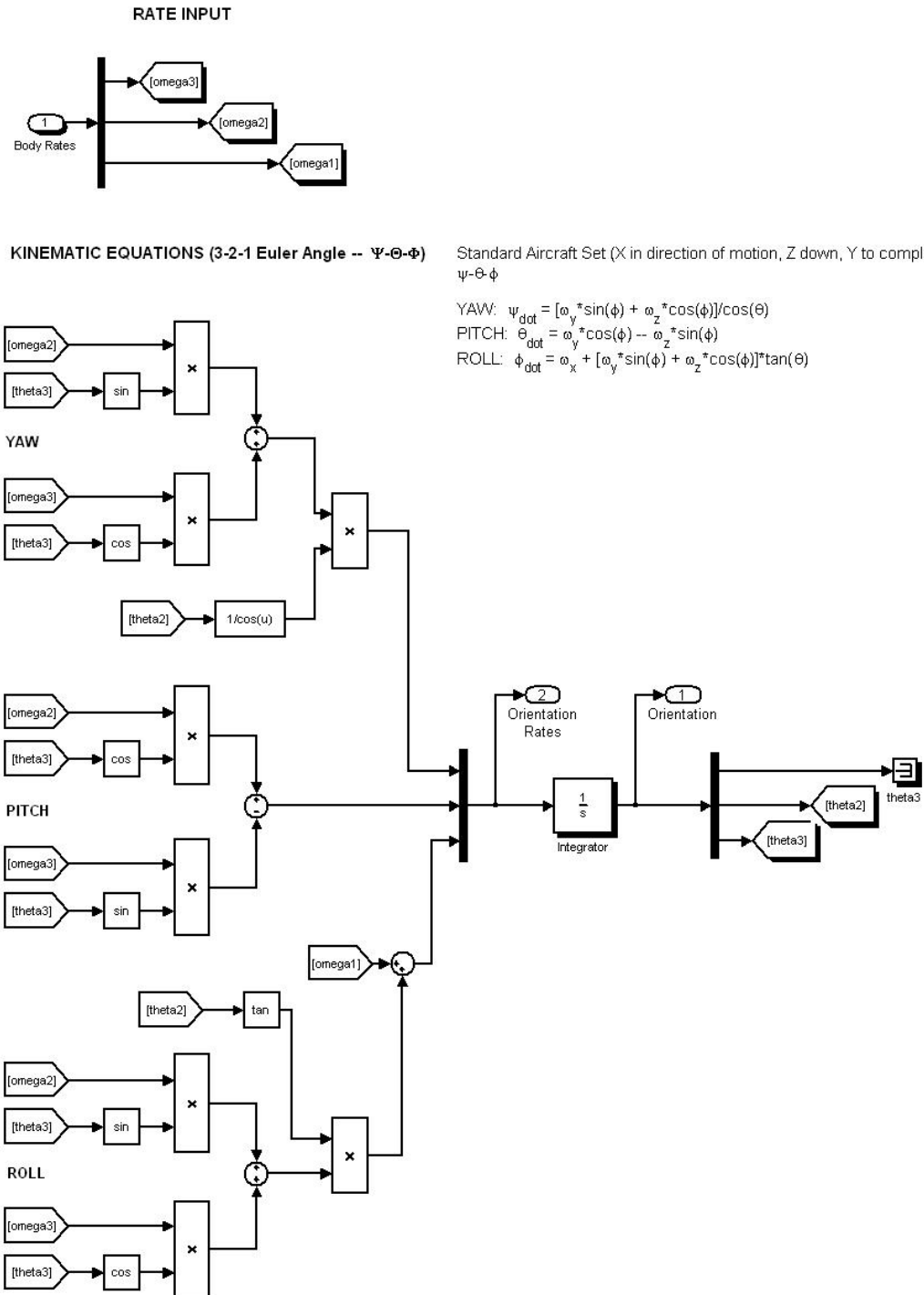


Figure D.6 Euler 3-2-1 Kinematics, Level 2 Submodel

Appendix E. Experimental Model Library

The following figures illustrate the control logic of the satellite simulator. It was used to define the command/telemetry structure of the experiment. The programming language is Simulink®.

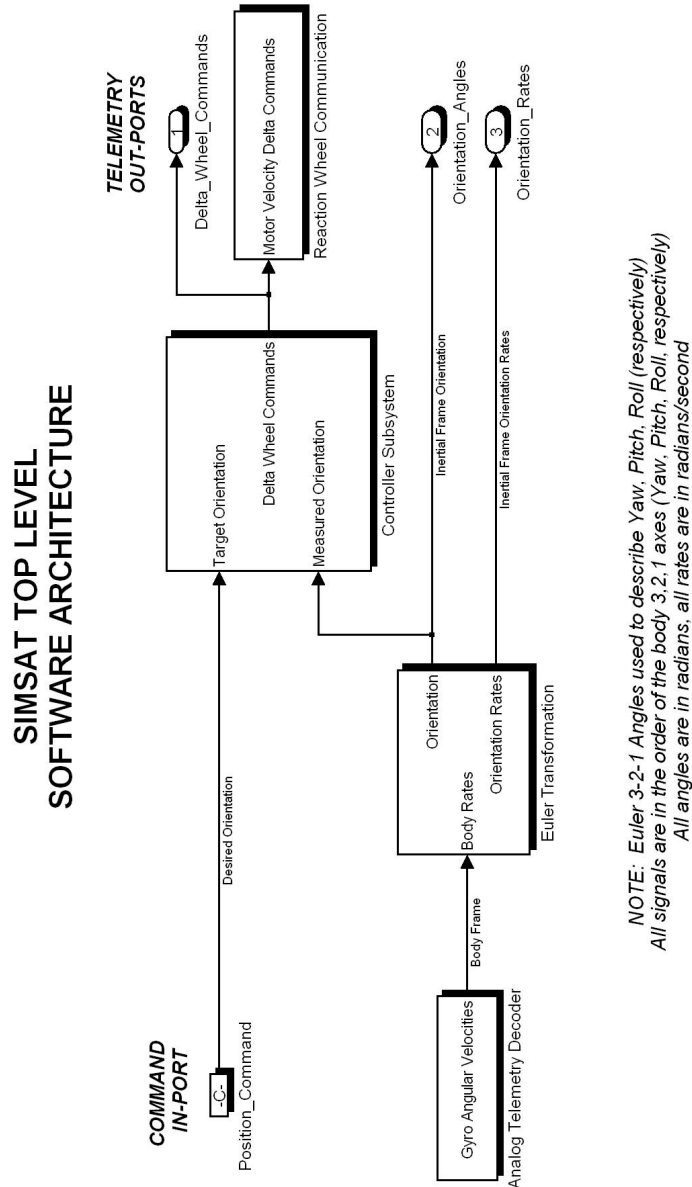


Figure E.1 Top Level Experimental Model

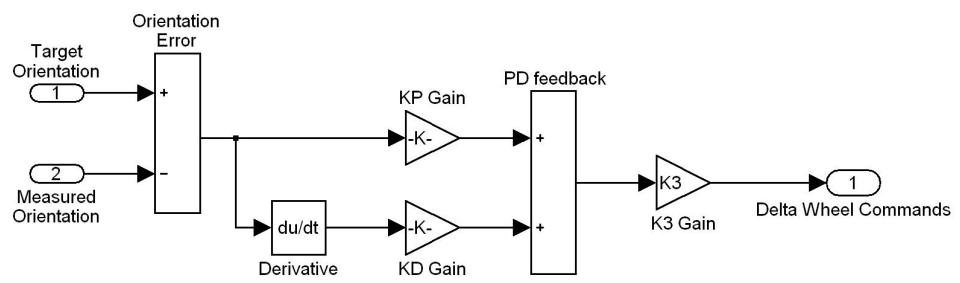


Figure E.2 Proportional Plus Derivative Controller, Level 2 Submodel

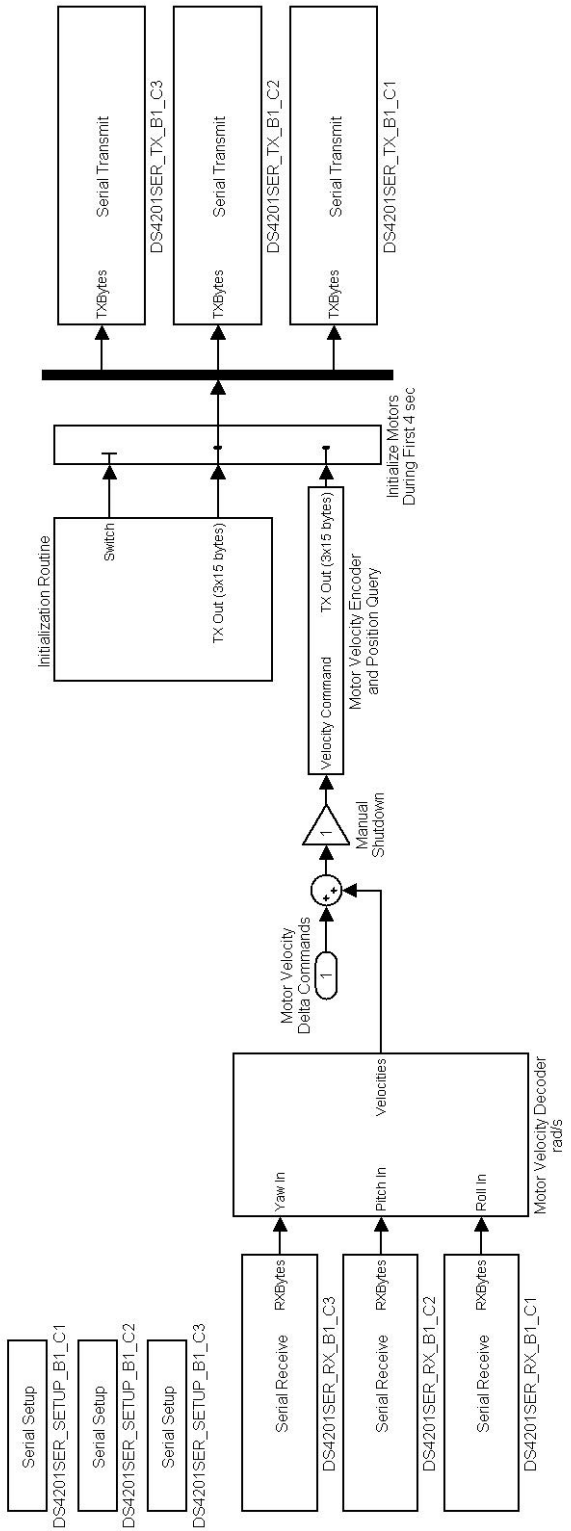


Figure E.3 Motor Communications, Level 2 Submodel

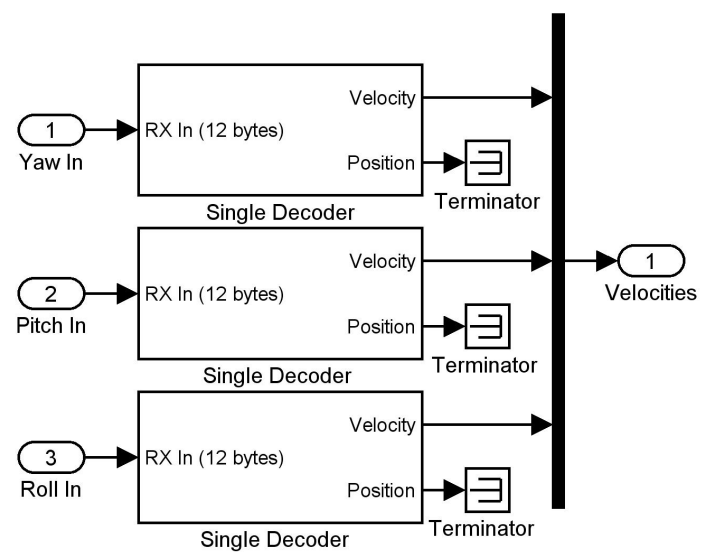


Figure E.4 Velocity Decoder Cluster, Level 3 Submodel

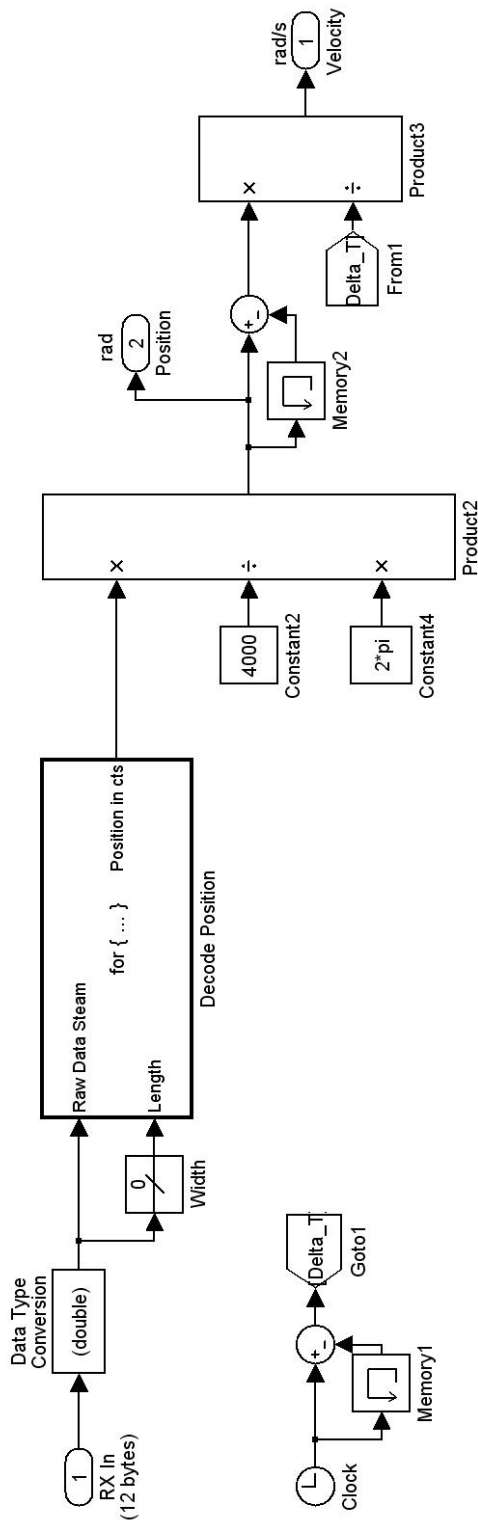


Figure E.5 Single Velocity and Position Decoder, Level 4 Submodel

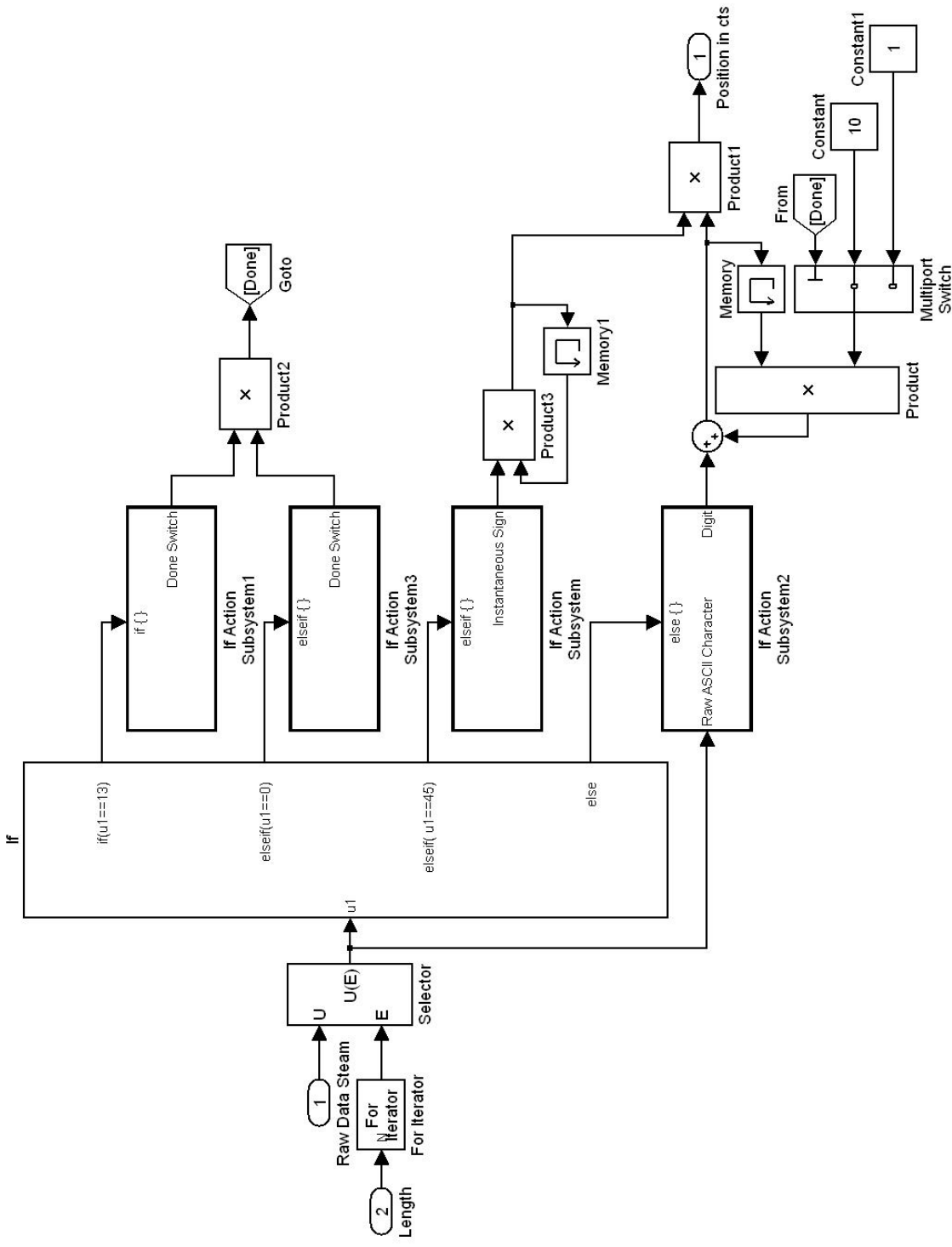


Figure E.6 Position Decoder, Level 5 Submodel

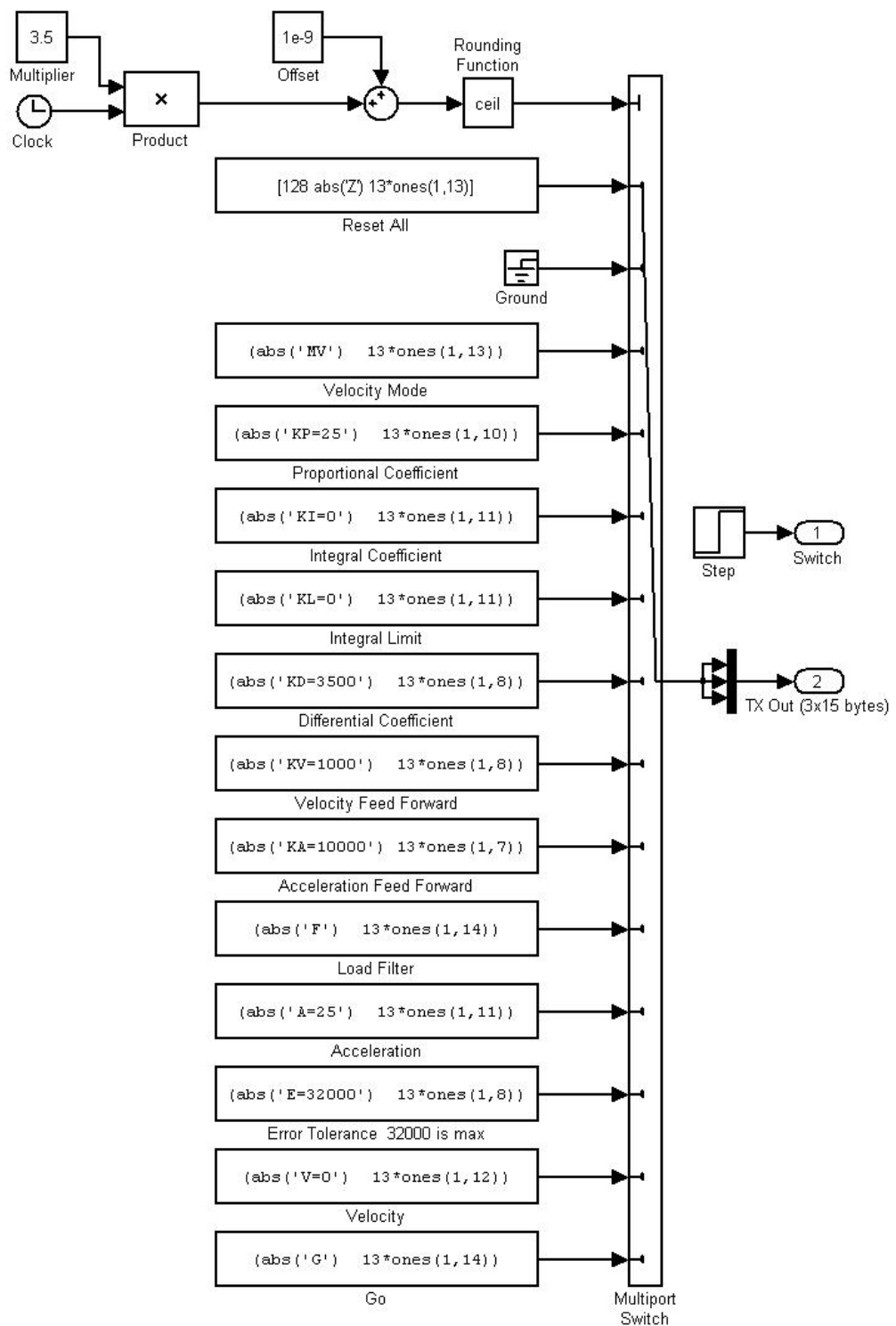


Figure E.7 Motor Initialization, Level 3 Submodel

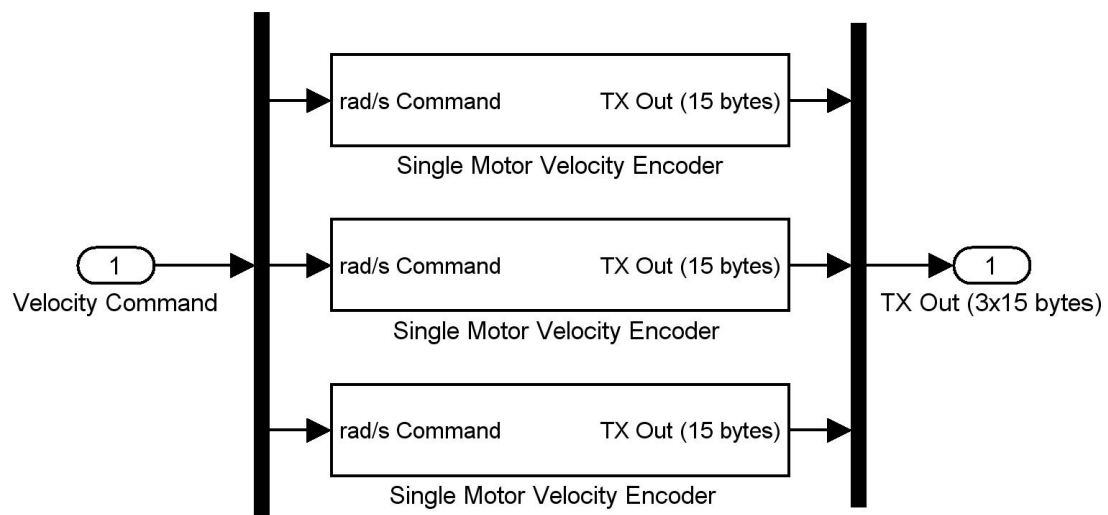


Figure E.8 Velocity Encoder Cluster, Level 3 Submodel

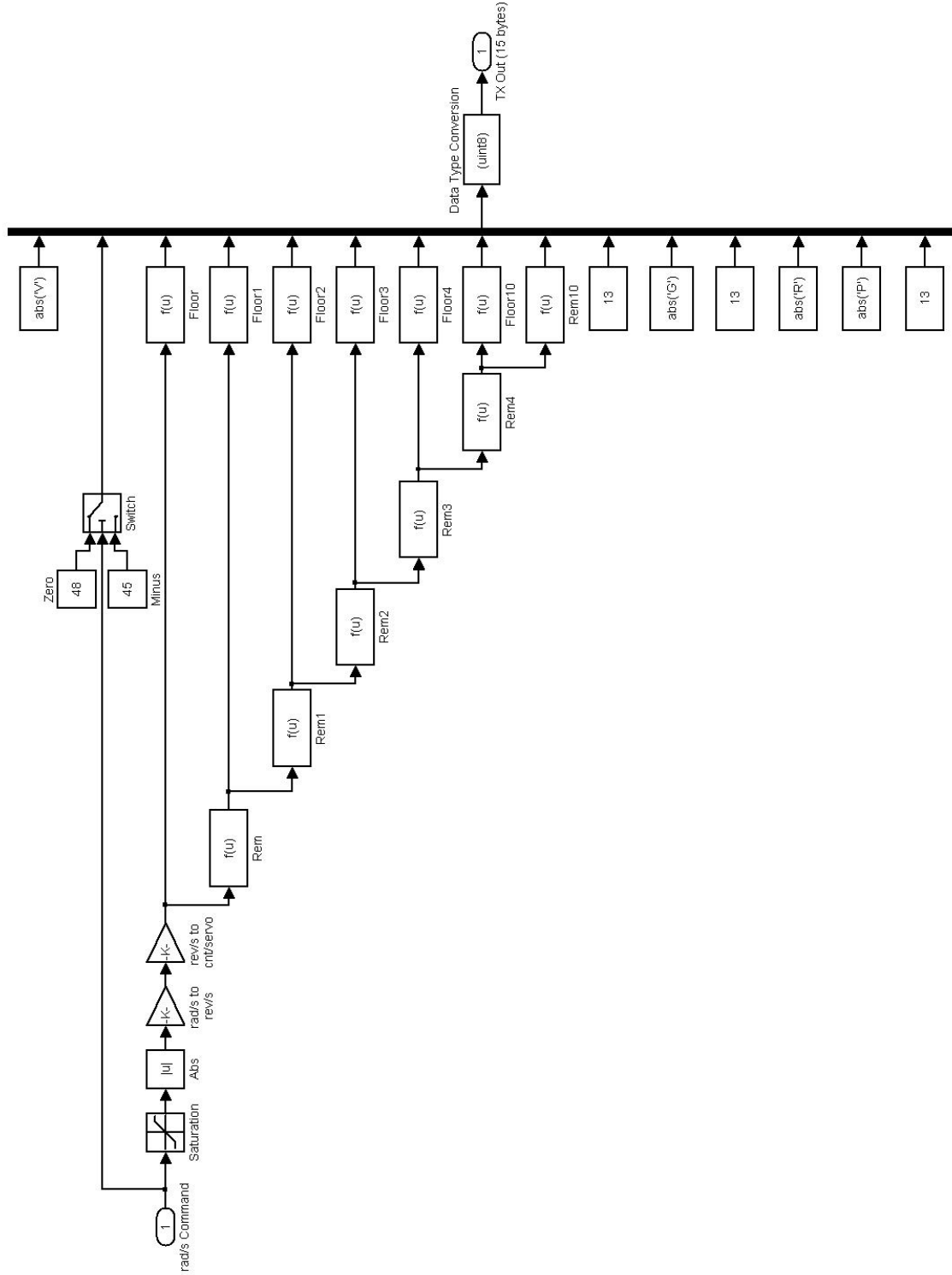


Figure E.9 Single Velocity Encoder, Level 4 Submodel

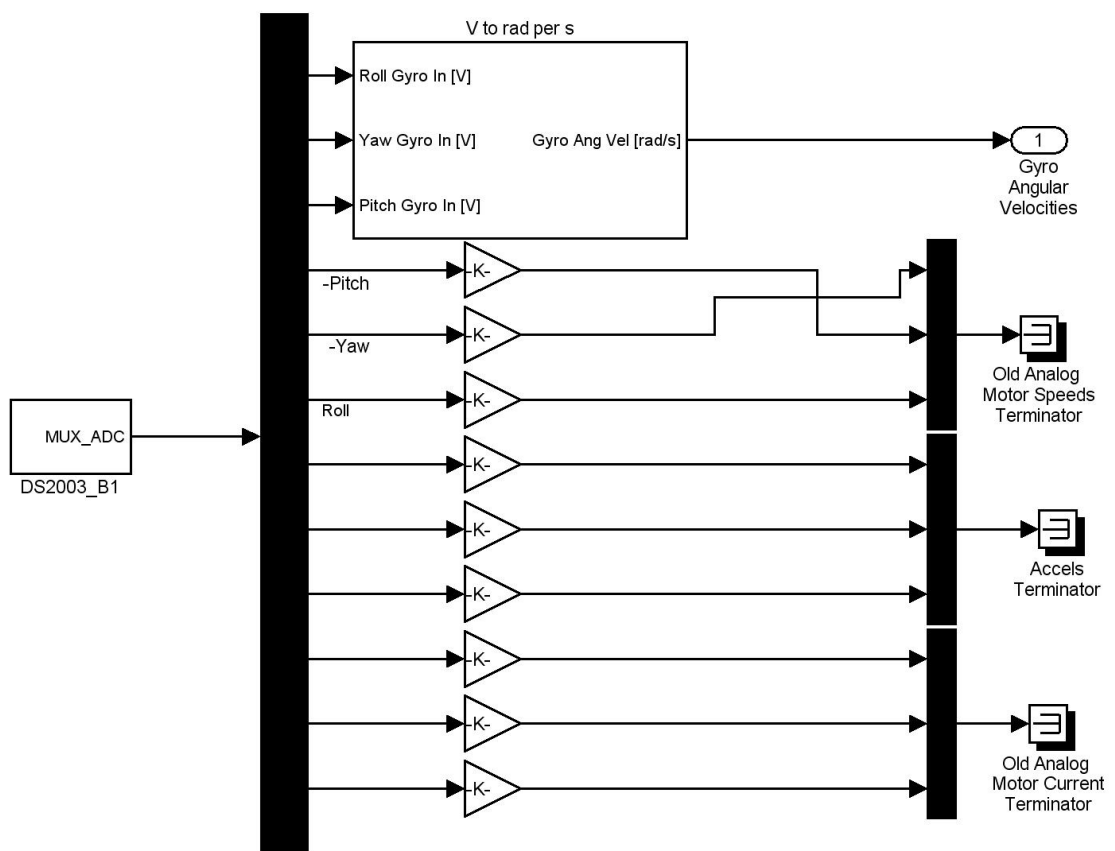


Figure E.10 Analog Telemetry Decoder, Level 2 Submodel

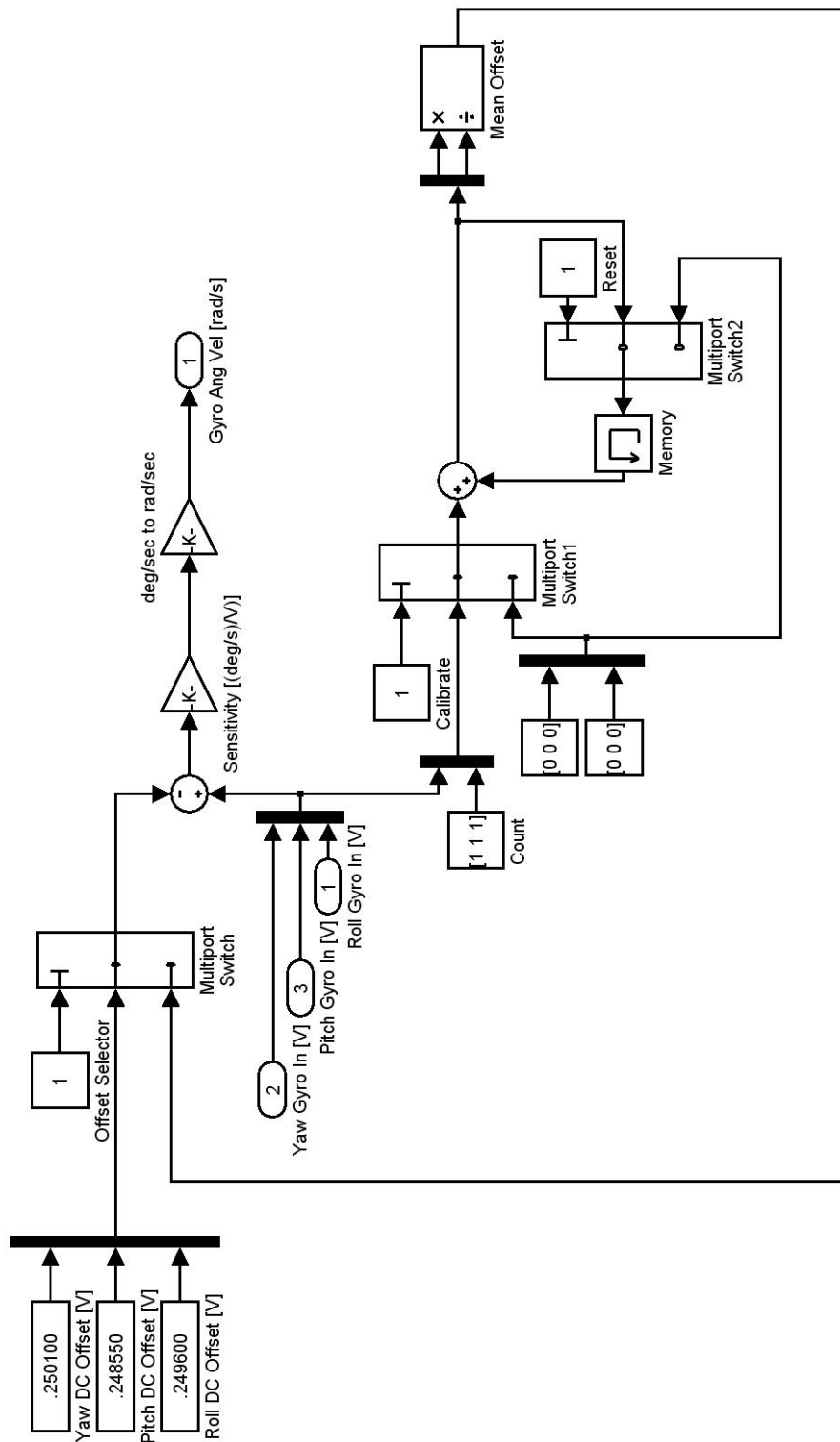


Figure E.11 Gyroscope Decoder and Calibration, Level 3 Submodel

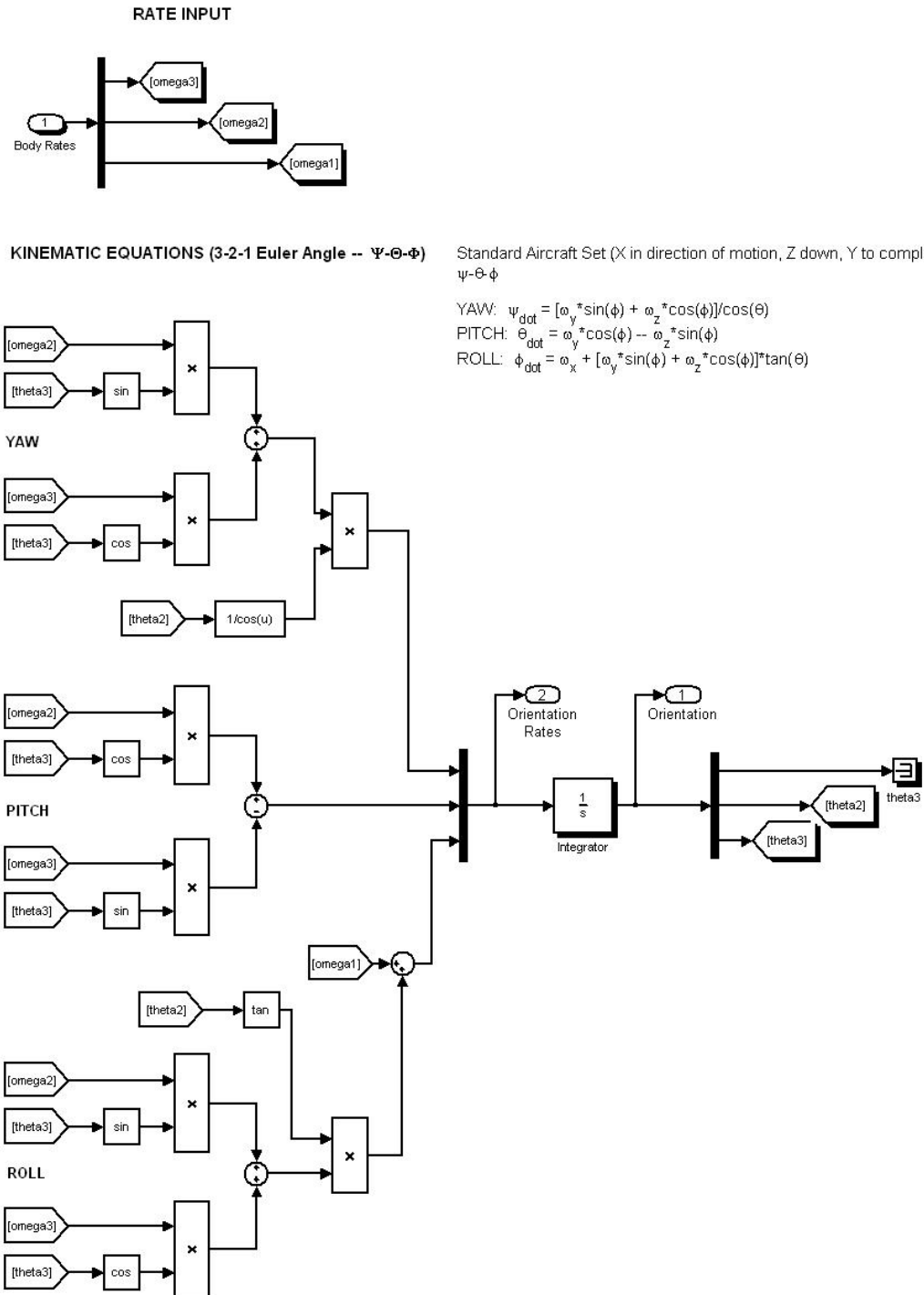


Figure E.12 Euler 3-2-1 Kinematics, Level 2 Submodel

Appendix F. Experiment Software User Interface

ControlDesk® software by dSPACE, Inc. was used as the real-time link between the experimental hardware (SIMSAT), control software (Simulink®), and the user. An interface (Figure F.1) was created to more easily recalibrate the gyroscopes. The user can immobilize the SIMSAT and “zero out” the gyroscope before the start of operations. An averaging mechanism is designed into the Simulink® model to assist in the calibration process.

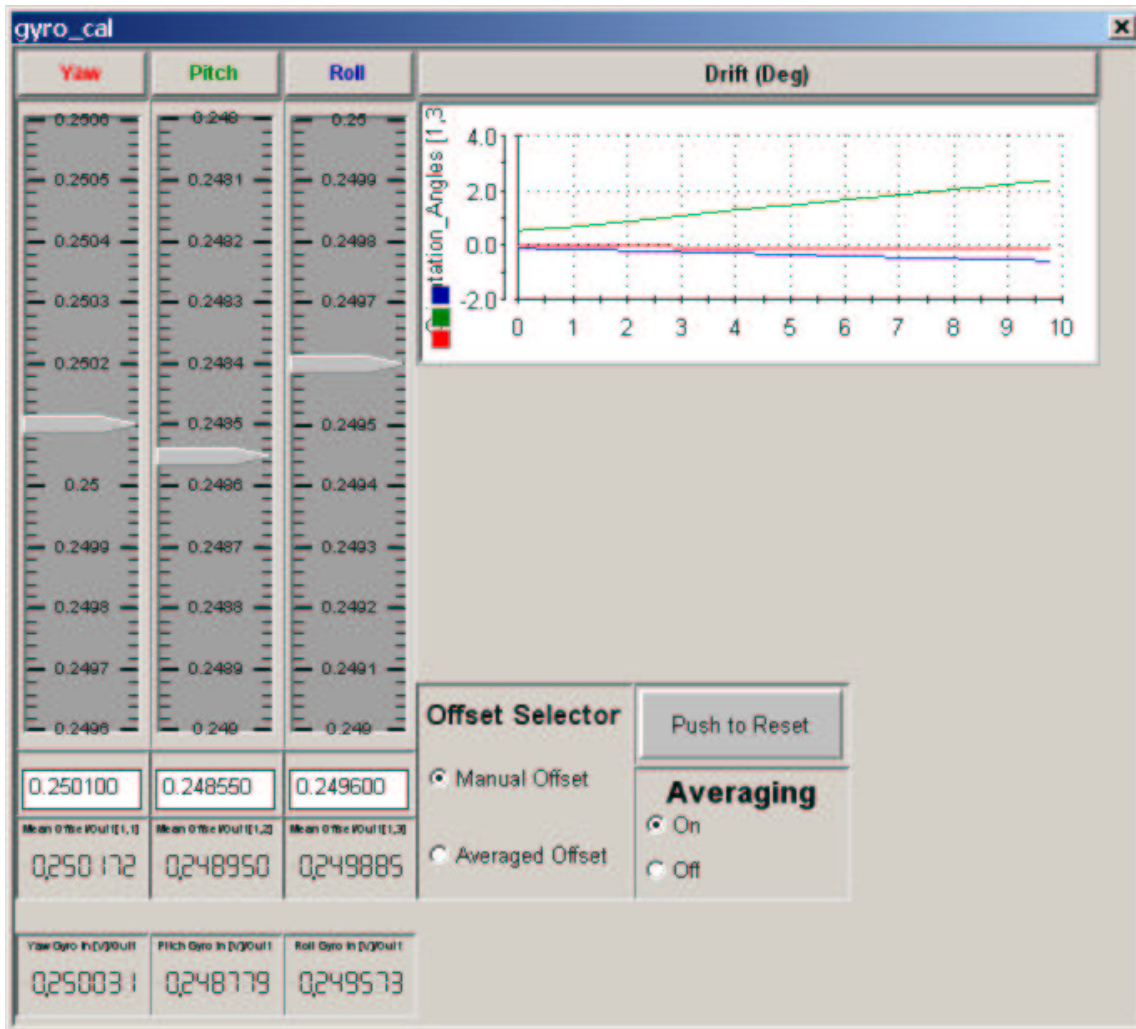


Figure F.1 Gyroscope Calibration Interface

The ground station interface was developed for general SIMSAT usage and is illustrated in Figure F.2. This interface was reproduced from the original SIMSAT design effort as a demonstration and diagnostics tool. It includes three different ways to input position commands and three large buttons to allow the operator to quickly return the system to the origin. The satellite angular velocity and reaction wheel speeds are displayed both on dials and numerically. The PD controller settings were added to the layout and can be adjusted during operations as necessary.

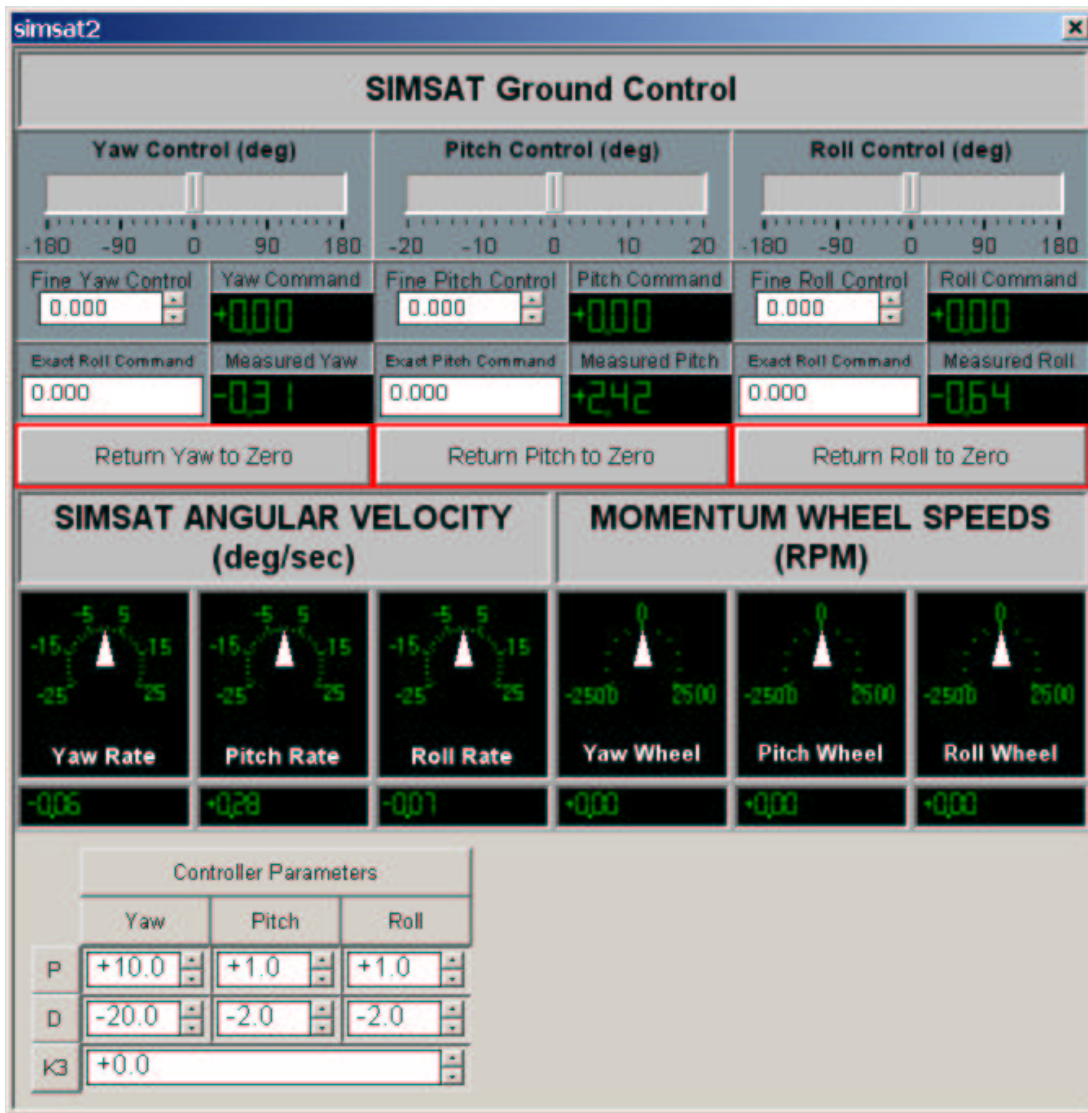


Figure F.2 General Operation Interface

Bibliography

1. Adachi, Shuichi, et al. “On-Orbit System Identification Experiments on Engineering Test Satellite-VI,” *Control Engineering Practice*, 7(7):831–41 (July 1999).
2. Andersen, G.C., et al. “An Overview of the Hubble Space Telescope Pointing Control System Design and Operation.” *Proceedings of the 1992 AIAA Guidance Navigation and Control Conference*. Reston, VA: American Institute of Aeronautics and Astronautics, 1992.
3. Bayard, D.S., et al. “Automated On-Orbit Frequency Domain Identification for Large Space Structures,” *Automatica*, 27(6):931–46 (November 1991).
4. Brody, Adam R. “Evaluation of the ’0.1 Percent Rule’ for Docking Maneuvers,” *Journal of Spacecraft and Rockets*, 27 (January-February 1990).
5. Buckley, A.P. “Hubble Space Telescope Pointing Control System Design Improvement Study Results,” *Journal of Guidance, Control and Dynamics*, 18(2):194–9 (1995).
6. “China is Developing Anti-Satellite Weapon as a Counter Measure.” *Hong Kong Ming Pao*, Internet Version Translated by Foreign Broadcast Information Service, 30 January 2001.
7. Clemen, Carsten. “New Method for On-Orbit-Determination of Parameters for Guidance, Navigation and Control,” *Acta Astronautica*, 51(1-9):457–65 (July 2002).
8. Colebank, James E., et al. *SIMSAT: A Satellite System Simulator and Experimental Test Bed for Air Force Research*. MS thesis, AFIT/GSE/GSO/ENY/99M-1, Air Force Institute of Technolgy, Wright-Patterson AFB OH, March 1999.
9. The Commission to Assess United States National Security Space Management and Organization. *Report of the Commission to Assess United States National Security Space Management and Organization*. Technical Report. Washington: Government Printing Office, January 2001.
10. Desrocher, David, et al. “Data Exploitation Techniques for Enhanced Satellite Operations.” *SatMax 2002: Satellite Performance Workshop*. Reston, VA: American Institute of Aeronautics and Astronautics, April 2002.
11. Garg, S.C. and P.C. Hughes. “Flight Results on Structural Dynamics from Hermes,” *Journal of Spacecraft*, 16(2):81–7 (1979).

12. Grocott, S., et al. "Robust Control Design and Implementation on the Mid-deck Active Control Experiment," *Journal of Guidance, Control, and Dynamics*, 17(6):1163–70 (1994).
13. Gulczinski, Frank S., et al. "Micropropulsion Research at AFRL." *36th AIAA/ASME/SAE/ASEE Joint Propulsion Conference & Exhibit*. July 2000.
14. Haugse, E. D., et al. "On-Orbit System Identification." *37th AIAA/ASME/ASCE/AHS/ASC Structures, Structural Dynamics and Materials Conference and Exhibit*. 2398–407. Reston, VA: American Institute of Aeronautics and Astronautics, April 1996.
15. Huang, Jen-Kuang, et al. "State-Space System Identification from Closed-Loop Frequency Response Data," *Journal of Guidance, Control, and Dynamics*, 19(6):1378–80 (November/December 1996).
16. Ledebuhr, A.G., et al. "Micro-Satellite Ground Test Vehicle for Proximity and Docking Operations Development." *Proceedings of the 2001 IEEE Aerospace Conference*. 2493–504. Piscataway, NJ: IEEE, 2001.
17. Ledebuhr, A.G., et al. "Autonomous, Agile, Micro-Satellites and Supporting Technologies for Use in Low-Earth Orbit Missions." *Proceedings of the 12th AIAA/USU Conference on Small Satellites*. Logan, UT: Utah State University, 1998.
18. Liu, K. and R. Skelton. "Closed-Loop Identification and Iterative Controller Design." *Proceedings of the 29th IEEE Conference on Decision and Control*. 482–7. New York, NY: IEEE, 1990.
19. "Lockheed Martin Missles & Space Photo Page." Lockheed Martin Missles & Space Homepage, <http://lmms.external.lmco.com>, Accessed: 8 February 2003.
20. Manning, R.A. and S.C. Casteel. "On-Orbit Performance of the Advanced Controls Technology Experiment." *Proceedings of the 1997 American Control Conference*. 3990–4. Evanston, IL: American Autom. Control Council, 1997.
21. Moser, Ruth L., et al. "Low Cost Microsatellites: Innovative Approaches to Breaking the Cost Paradigm." *AIAA Space 2000 Conference & Exposition*. September 2000.
22. "NASA Quest Hubble Space Telescope Photo Page." NASA Quest Homepage, <http://quest.arc.nasa.gov>, Accessed: 20 February 2003.
23. "Navstar Global Positioning System (GPS) Replenishment Satellites (Block IIR) Phase II Mass Properties Report - Subnumber 1.0." Martin Marietta Corporation, Astro Space Division, 9 March 1995.
24. Nelson, Robert C. *Flight Stability and Automatic Control*. New York: McGraw-Hill, 1998.

25. Nurre, G.S., et al. "Preservicing Mission, On-Orbit Modifications to Hubble Space Telescope Pointing Control System," *Journal of Guidance, Control, and Dynamics*, 18(2):222–9 (1995).
26. Office of the Secretary of Defense. *Department of Defense Space Technology Guide, FY 2000-01*. Technical Report. Washington: Government Printing Office, FY 2000-01.
27. Ravazzotti, Maria T. and Maurizio Betto. "A Rendezvous Simulator for a Maneuvering Inspection Vehicle." *Proceedings of the 47th International Astronautical Congress*. 1996.
28. Saunders, Phillip, et al. *China's Space Capabilities and the Strategic Logic of Anti-Satellite Weapons*. Research Story of the Week, <http://cns.miis.edu/pubs/week/index.htm>, Monterey, CA: Center for Nonproliferation Studies, Monterey Institute of International Studies, 22 July 2002.
29. Schlock, R.W. "Solar Array Flight Dynamics Experiment." *Proceedings of the Workshop on Structural Dynamics and Control Interaction of Flexible Structures*. 487–504. 1986.
30. Scott, William B. "Cincspace Wants Attack Detectors on Satellites," *Aviation Week & Space Technology*, 149(6):22–4 (August 1998).
31. "Small Satellites Home Page." Surrey Space Centre Website, <http://www.smallsatellites.org>, Accessed: 1 February 2003.
32. *Space Object Identification*. Contract N00014-97-D-2014/001, Albuquerque, NM: Schafer Corporation, February 1999.
33. Stetson, John B., Jr. "On-Orbit Identification of NOAA-2," *Advances in the Astronautical Sciences*, 87(1):3–16 (1994).
34. Stevens, Brian L. and Frank L. Lewis. *Aircraft Control and Simulation*. New York, NY: John Wiley & Sons, Inc. 1992.
35. Takezawa, Satoshi, et al. "Experimental Study of Rendezvous Docking Mechanism for Microsatellite Under the Microgravity." *Proceedings of the 22nd International Symposium on Space Technology and Science*. 1238–42. Tokyo, Japan: Japan Society for Aeronautical and Space Sciences and 22nd ISTS Organizing Committee, 2000.
36. Tschan, Chris. "Defensive Counterspace (DCS) Test Bed (DTB) for Rapid Spacecraft Attack/Anomaly Detection, Characterization, and Reporting." Briefing at the 2001 Ground System Architectures Workshop, El Segundo, California, February 21-23 2001.
37. Vidal, E., et al. "Open and Closed Loop Parametric System Identification in Compact Disk Players." *Proceedings of the American Control Conference*. 3294–3298. 2001.

38. Walker, Michael W. and Dong-Min Kim. “Satellite Stabilization Using Space Leeches.” *Proceedings of the 1990 American Control Conference*. 1314–9. 1990.
39. Wertz, Julie A. and Allan Y. Lee. “Inflight Estimation of the Cassini Spacecraft’s Inertia Tensor.” *Proceedings of the 2001 AAS Spaceflight Mechanics Meeting*. 1087–102. 2001.
40. Whorton, Mark S. and Anthony J. Calise. “On-Orbit Model Refinement for Controller Redesign.” *Proceedings of the 1998 IEEE Aerospace Conference*. 105–16. New York, NY: IEEE, 1998.
41. Wie, Bong. *Space Vehicle Dynamics and Control*. Reston, VA: American Institute of Aeronautics and Astronautics, Inc. 1998.
42. Wilson, Sam B., III, “Orbital Express, A Comprehensive Architecture for the 21st Century.” Presentation from DARPATech2000. DARPA Website, <http://www.darpa.mil/darpatech2000/presentations>, 6–8 September 2000.
43. Wilson, Tom. *Threats to United States Space Capabilities*. Staff Background Paper to the Commission to Assess United States National Security Space Management and Organization. Washington: Government Printing Office, 2000.
44. Worden, Simon P. “New Directions for National Security Space Programs.” *Space Access and Utilization Beyond 2000; Proceedings of the Symposium*. 133–43. San Diego, CA: Univelt, Inc. 2001.
45. Yamaguchi, Isao, et al. “Open-Loop System Identification of Large Space Structures from Closed-Loop Impulse Response by On-Orbit Excitation.” *Proceedings of the 21st International Symposium on Space Technology and Science*. 718–23. Tokyo, Japan: 21st ISTS Publications Committee, 1998.
46. Yi, Tung, “China Completes Ground Tests of Anti-Satellite Weapon.” *Hong Kong Sing Tao Jih Pao*, Internet Version Translated by Foreign Broadcast Information Service, 5 January 2001.

Vita

Captain Vincent J. Dabrowski was raised in Northwest New Jersey and graduated from Wallkill Valley Regional High School in 1993. He entered undergraduate studies at Embry-Riddle Aeronautical University in Daytona Beach, Florida where he graduated with a Bachelor of Science degree in Engineering Physics in December 1997. He was subsequently commissioned through the Detachment 157 AFROTC.

His first assignment was at Wright-Patterson AFB as an Acquisition Program Manager Intern at the Aeronautical System Center. As part of his training, he spent one year as a F-16 Training Systems Contract Manager in the Training System Product Group followed by one year as a C-17 Integration and Test Engineer in the C-17 System Program Office. Subsequently, he was assigned to the F-22 System Program Office as the F-22 Lot II Production Program Manager. There, he lead the acquisition of 13 aircraft, support, and training equipment worth \$2.6B.

In August 2001, he entered the Graduate School of Engineering and Management, Air Force Institute of Technology. He was married in March 2002. Upon graduation, he will be assigned to the Air Force Research Lab's Munitions Directorate at Eglin AFB, Florida.

REPORT DOCUMENTATION PAGE

*Form Approved
OMB No. 0704-0188*

The public reporting burden for this collection of information is estimated to average 1 hour per response, including the time for reviewing instructions, searching existing data sources, gathering and maintaining the data needed, and completing and reviewing the collection of information. Send comments regarding this burden estimate or any other aspect of this collection of information, including suggestions for reducing this burden to Department of Defense, Washington Headquarters Services, Directorate for Information Operations and Reports (0704-0188), 1215 Jefferson Davis Highway, Suite 1204, Arlington, VA 22202-4302. Respondents should be aware that notwithstanding any other provision of law, no person shall be subject to any penalty for failing to comply with a collection of information if it does not display a currently valid OMB control number. PLEASE DO NOT RETURN YOUR FORM TO THE ABOVE ADDRESS.

1. REPORT DATE (DD-MM-YYYY) 25-03-2003	2. REPORT TYPE Master's Thesis	3. DATES COVERED (From — To) Sep 2001 – Mar 2003		
4. TITLE AND SUBTITLE EXPERIMENTAL DEMONSTRATION OF AN ALGORITHM TO DETECT THE PRESENCE OF A PARASITIC SATELLITE		5a. CONTRACT NUMBER 5b. GRANT NUMBER 5c. PROGRAM ELEMENT NUMBER		
6. AUTHOR(S) Dabrowski, Vincent J., Captain, USAF		5d. PROJECT NUMBER 5e. TASK NUMBER 5f. WORK UNIT NUMBER		
7. PERFORMING ORGANIZATION NAME(S) AND ADDRESS(ES) Air Force Institute of Technology Graduate School of Engineering and Management 2950 P Street, Building 640 WPAFB OH 45433-7765		8. PERFORMING ORGANIZATION REPORT NUMBER AFIT/GAE/ENY/03-2		
9. SPONSORING / MONITORING AGENCY NAME(S) AND ADDRESS(ES)		10. SPONSOR/MONITOR'S ACRONYM(S) 11. SPONSOR/MONITOR'S REPORT NUMBER(S)		
12. DISTRIBUTION / AVAILABILITY STATEMENT APPROVAL FOR PUBLIC RELEASE; DISTRIBUTION IS UNLIMITED.				
13. SUPPLEMENTARY NOTES				
14. ABSTRACT Published reports of microsatellite weapons testing have led to a concern that some of these “parasitic” satellites could be deployed against US satellites to rendezvous, dock and then disrupt, degrade, disable, or destroy the system. An effective detection method is essential. Various sensing solutions were investigated including visual, impact, and dynamic techniques. Dynamic detection, the most effective solution, was further explored. A detection algorithm was constructed and validated on the Air Force Institute of Technology’s ground-based satellite simulator, SIMSAT. Results indicate that microsatellites rigidly connected to a satellite can be detected with a series of small identical maneuvers utilizing data available today. All algorithm variations readily detected parasite-induced moment of inertia changes of 3–23%. The most accurate detection scheme estimated the moment of inertia to 0.67%. The results look promising for sensing potential microsatellite threats to US systems. The detection scheme presented could easily be integrated into a complete space situational awareness system.				
15. SUBJECT TERMS Parasitic Satellite; Anti-Satellite Weapon; Detection Algorithm; Moment of Inertia Estimation; Inertia Tensor Estimation; System Identification; Satellite Simulator; Hardware Simulation				
16. SECURITY CLASSIFICATION OF: a. REPORT U b. ABSTRACT U c. THIS PAGE U		17. LIMITATION OF ABSTRACT UU	18. NUMBER OF PAGES 117	19a. NAME OF RESPONSIBLE PERSON Richard G. Cobb, Maj, USAF (ENY) 19b. TELEPHONE NUMBER (include area code) (937) 255-3636, ext 4559